

**BIOLOGICALLY INSPIRED SURFACE DESIGN USING CHEMICAL
VAPOR DEPOSITION POLYMERIZATION**

by

Xiaopei Deng

A dissertation submitted in partial fulfillment
of the requirements for the degree of
Doctor of Philosophy
(Macromolecular Science and Engineering)
in the University of Michigan
2013

Doctoral Committee:

Professor Joerg Lahann, Chair
Professor Zhan Chen
Assistant Professor Anastasios John Hart
Professor Paul H. Krebsbach

ACKNOWLEDGMENTS

First and foremost, I would like to express my most sincere gratitude and appreciation to my PhD advisor Joerg Lahann for his guidance, support and help in every aspect of my study including experimental design, academic paper writing, presentation skills and future career development. He keeps me inspired by his positive perspectives, great passion for academic researches and hard-working attitude. I am also grateful to my dissertation committee members Prof. Zhan Chen, Prof. Paul H. Krebsbach and Prof. Anastasios John Hart not only for their constant encouragement and insightful suggestions but also for the fruitful collaborations.

I am deeply thankful for all my collaborators especially Dr. Christian Friedmann, Thomas Eyster, Dr. Hsien-Yeh Chen, Dr. Yaseen Elkasabi, Dr. Takashi D. Y. Kozai, Dr. Sameh Tawfick, Dr. Ying Zhang, Dr. Aftin Ross and Prof. Henry Hess from Columbia University. I have learned a lot from each of them. I would like to express my special thanks to Thomas Eyster for proofreading this dissertation.

I also owe a warm thank you to the undergraduate students whom I had the pleasure of mentoring, and who were a great help for me, Shirin Chaphalkar and Douglas Reed.

Many thanks to the EMAL, MIL and UM Chemistry TechServices staff members Kai Sun, Haiping Sun, Ying Qi, Chris Edwards, Bruce Donahoe, Shelley

Almburg, Linda Barthel and James Windak for the instruments training and invaluable help.

All the past and current Lahann group members are pleasant to work with. I cherish all the fun and friendship with you.

It is my fortune to join the family-like Macromolecular Science and Engineering Program, especially to have the program assistant Nonna Hamilton taking care of us like a dearest mother.

For any achievement, I am indebted to my dear husband Bingyuan, who cares for me and cooks for me almost every day even though he also has a Material Science and Engineering PhD study to finish. I'd also like to thank my parents and in-laws for their unconditional love and support.

TABLE OF CONTENTS

ACKNOWLEDGEMENTS.....	ii
LIST OF FIGURES.....	ix
LIST OF TABLES.....	xvi
ABSTRACT.....	xvii
CHAPTER 1. Introduction.....	1
1.1 Motivation.....	1
1.2 Overview of the Dissertation.....	6
References.....	8
CHAPTER 2. Orthogonal Co-Immobilization Strategies for Biomolecules Based on Multifunctional Chemical Vapor Deposition Polymer Coatings.....	10
2.1 Bio-Orthogonal "Double-Click" Chemistry Based on Multifunctional Coatings....	15
2.1.1 Introduction.....	15
2.1.2 Experimental Section.....	16
Synthesis of [2.2]Paracyclophane-4-methyl propiolate.....	16
CVD Polymerization.....	18
Surface Characterization.....	18
Surface Immobilization.....	19

2.1.3 Results and Discussion.....	20
2.1.4 Conclusion.....	27
2.2 Bio-orthogonal Polymer Coatings for Co-Presentation of Biomolecules.....	31
2.2.1 Introduction.....	31
2.2.2 Experimental Section.....	34
CVD Co-Polymerization.....	34
Surface Characterization.....	34
Immobilization of EGF.....	35
Immobilization of the cRGD Peptide.....	35
Adhesion and Spreading of Endothelial Cells.....	36
Phosphorylated EGFR Immunofluorescence.....	36
EGF EC ₅₀ Measurement.....	37
Image and Statistical Analysis.....	38
2.2.3 Results and Discussion.....	39
2.2.4 Conclusion.....	47
2.3 A Generic Strategy for Co-Presentation of Heparin-Binding Growth Factors	
Based on CVD Polymerization.....	48
2.3.1 Introduction.....	48
2.3.2 Experimental Section.....	51
CVD Co-Polymerization.....	51
Surface Characterization.....	52
Immobilization of Biomolecules.....	52
2.3.3 Results and Discussion.....	54

2.3.4 Conclusion.....	61
References.....	63
CHAPTER 3. Towards Biosensors Development: Metal Enhanced Fluorescence on CVD Polymer Coated Gold Films.....	70
3.1 Introduction.....	70
3.2 Experimental Section.....	72
3.2.1 Electron Beam Evaporation Metal Coating	72
3.2.2 CVD Precursor Synthesis.....	73
3.2.3 CVD Polymerization.....	75
3.2.4 Polymer Coating Characterization.....	76
3.2.5 Fluorescent Molecules Immobilization and Imaging.....	76
3.3 Results and Discussion.....	79
3.4 Summary and Outlook.....	92
References.....	96
CHAPTER 4. Biodegradable CVD Polymer Films.....	99
4.1 Introduction.....	99
4.2 Experimental Section.....	101
4.2.1 Synthesis of Cyclic Ketene Acetals	101
4.2.2 CVD Copolymerization of [2.2]Paracyclophanes and Cyclic Ketene Acetals.....	105
4.2.3 Surface Characterization and Degradation Progress Tracking	106
4.2.4 Degradation Condition.....	106
4.3 Results and Discussion.....	106

4.4 Conclusion and Future work.....	110
References.....	111
CHAPTER 5. Applications of CVD Polymer Coatings on Complex Structures and Integrated Devices.....	113
5.1 Nanocomposite Microstructures with Tunable Mechanical and Chemical Properties.....	114
5.1.1 Introduction.....	115
5.1.2 Experimental Section.....	117
CNT Growth.....	117
CVD Polymer Coating.....	118
Surface Characterization.....	118
Surface Functionalization.....	119
Mechanical Testing.....	119
5.1.3 Results and Discussion.....	120
5.1.4 Conclusion.....	130
5.2 Materials and Surface Design of Ultrasmall Implantable Composite Microelectrodes for Chronic Neural Interfaces.....	132
5.2.1 Introduction.....	133
5.2.2 Experimental Section.....	136
Functional CVD Coatings on Carbon-fibre Microthread Electrodes (MTEs).....	136
Atom Transfer Radical Polymerization.....	136
Probe Tip Treatment with PEDOT.....	137

Electrical Characterization	137
Protein Adsorption.....	138
SEM Imaging.....	138
Microscopic Raman Spectroscopy.....	138
5.2.3 Results and Discussion.....	142
5.2.4 Conclusion.....	148
References.....	151
CHAPTER 6. Conclusion and Future Directions.....	158
6.1 Conclusion.....	158
6.2 Future Directions.....	161
6.2.1 Combining the Functional Coating Platform with Multifunctional Linkers.....	161
6.2.2 Understanding the Biomolecule-Surface Interactions.....	162
6.2.3 Improving the CVD Polymerization System Design.....	163
6.2.4 Developing More Integrated and Sophisticated Devices.....	163
References.....	165

LIST OF FIGURES

Figure 1.1 CVD polymerization scheme for the substituted [2.2]paracyclophanes and the established functional groups library.....	3
Figure 1.2 Overview of the four different aspects of biomedical surface design based on CVD polymerization platform in this dissertation.....	6
Figure 2.1 Combinations of chemical functional groups for orthogonal immobilizations of multiple biomolecules.....	13
Figure 2.2 Two types of spatial arrangements for the orthogonal functional groups.....	14
Figure 2.3 CVD polymerization process of polymers with inactivated (1) and activated alkyne groups (2).....	20
Figure 2.4 a) FTIR spectrum for poly[(<i>p</i> -xylylene-4-methyl-propiolate)- <i>co</i> -(<i>p</i> -xylylene)] (2); b) chemical composition of polymer 2 determined by XPS. Experimental values are compared with calculated values. Spectra are shown in Figure 2.8.....	21
Figure 2.5 Chemical reactivity comparison of polymer 1 and 2 at copper-free condition using μ CP for 3 h at room temperature. CVD polymer coatings on the samples: (a) poly- <i>p</i> -xylylene (no reactive functional group, R=H in Figure 2.3); (b) polymer 1 (with inactivated alkyne); (c) polymer 2 (with activated alkyne). After CVD coating, the same treatment was done to samples in all the 3 images: μ CP of biotin-PEG-azide followed by TRITC streptavidin solution incubation. Scale bars represent 500 μ m.....	22
Figure 2.6 Chemical reactivity comparison of polymer 1 and 2 under copper-free conditions in solution reactions at room temperature. Samples coated by a 2-step CVD process using the VAMPIR technique resulted in surfaces with different polymer coatings inside and outside the squares. a1), a2), b) polymer 2 inside the squares and polymer 1 outside as shown in Figure 2.7, c) the reverse pattern, where polymer 1 is inside the squares. a1) bright field image of sample incubated in deionized water and then TRITC-streptavidin, a2) same sample as in (a1) but under red channel. b) and c) samples incubated in biotin-PEG-azide water solution and then TRITC-streptavidin solution. Scale bars represent 200 μ m.....	24

Figure 2.7 Scheme of two-step click reactions on surface coated with different polymers in different selected areas. The goal is to achieve sequential immobilization of molecules on defined areas of the same surface by utilizing the different reactivity of activated and nonactivated alkynyl groups towards azide groups. a), b), c) Fluorescence images of samples prepared exactly as shown in the schematic representation. b) overlay image of green and red channels shown in (a) and (c). Scale bar represents 200 μm	26
Figure 2.8 XPS survey spectrum and high-resolution peak fittings corresponding to the reported in the table of Figure 1.....	28
Figure 2.9 Thickness measurement on the micro-engineered surface by Imaging Ellipsometry. The thickness map was generated from delta map at 658nm by modeling. For more accurate measurement, multiwavelength 4-zone nulling was used to measure the average thickness of the region of interest (ROI) 0 and 1 in the image. For this particular sample, thickness for ROI 0 and ROI 1 is 51.2 nm and 48.1 nm respectively.....	29
Figure 2.10 Fluorescence image for 10 seconds printing on polymer 2	30
Figure 2.11 CVD copolymerization of [2.2]paracyclophanes with pentafluorophenyl ester and alkyne groups; $m = n$ for the copolymer 3 discussed in this chapter section.....	34
Figure 2.12 a): FTIR spectra for polymer 1 , 2 and 3 and b): chemical composition in atom-% shown as experimental value (calculated value in the bracket) determined by XPS; Experimental values of O and F atom ratios [%] were from survey results and other experimental values are from high resolution C 1s spectra peak fitting calculated based on a equimolar distribution of starting materials.....	39
Figure 2.13 a): Scheme for CVD copolymerization, biomolecules immobilization and potential cell responses. b) Fluorescence micrograph of epidermal growth factor (EGF) immobilized in patterned area after μCP and immunostaining. c1) Imaging ellipsometry thickness map of cRGD peptide pattern. c2) Thickness profile representing thickness difference along the red line shown in (c1).....	41
Figure 2.14 Fluorescence micrographs of HUVEC line seeded onto modified surfaces of polymer 3 after 4 h incubation. The surfaces were tethered with: (a) AEE (b) cRGD-only (c) EGF-only (d) cRGD + EGF (e) Quantification of spreading by ImageJ (three trials combined).....	43
Figure 2.15 Immunofluorescence of phosphorylated EGFR in A431 cells cultured on CVD-coated surfaces with tethered (a) AEE (b) cRGD (c) EGF and (d) cRGD+EGF. (e) Quantification of pEGFR immunofluorescence (three trials combined).....	45

Figure 2.16 a) EC ₅₀ plot for EGF (individual trial); b) Quantification of pEGFR immunofluorescence of phosphorylated EGFR in A431 cells in bar graph form (individual trial). The cells were cultured on CVD-coated surfaces passivated with AEE and in media with soluble EGF from 0-1000 ng/ml, in comparison with surface with tethered EGF in soluble EGF-free media.....	46
Figure 2.17 a) CVD copolymerization of [2.2]paracyclophanes with aldehyde and alkyne groups. $m = n$ for the copolymer 3 discussed in this chapter section. Polymer 1 and 2 are used as controls. b) Co-immobilization scheme for heparin-binding growth factor and adhesion peptide on the copolymer 3	51
Figure 2.18 FTIR spectra for polymers 1 , 2 and 3	54
Figure 2.19 a) TOF-SIMS images of carbonylhydrazide patterned on polymer 3 . The m/z values and their corresponding chemical structures are denoted by squares of different colors. b) Imaging ellipsometry thickness map of carbonylhydrazide pattern by μ CP, the thickness difference between the marked area 1 and 2 is 0.3 nm. c) Imaging XPS N1s elemental map of the carbonylhydrazide pattern at 400.0 eV. All scale bars represent 50 μ m.....	56
Figure 2.20 Scheme and fluorescence microscope images (a & b) after immunostaining the heparin and bFGF immobilized surface, respectively. In the scheme for this Figure, we use pink to represent heparin and green to represent bFGF, the same colors used in Scheme 1b. a) Fluorescence micrograph after immunostaining the immobilized heparin on the patterned carbonylhydrazide. b) Fluorescence micrograph after immunostaining the immobilized bFGF on the heparin. Scale bars are 500 μ m.....	59
Figure 2.21 Imaging ellipsometry thickness map (on the right side) of a cRGD azide pattern created by μ CP. The thickness difference between the marked area 1 and 2 is 0.5 nm. Scale bar represents 100 μ m.....	60
Figure 3.1 Chemical vapor deposition polymerization scheme for the two types of polymers used in this study.....	79
Figure 3.2 FTIR and XPS spectra of polymer 1	79
Figure 3.3 a) Fluorescence intensity of Alexa Fluor® 488 conjugated fibrinogen adsorbed on different substrates (35 nm gold – squares, 100 nm gold – diamonds, silicon – circles, triangle – glass) coated with polymer 1 films of different thicknesses. Black solid line: Eq. (1) with $I_0=105$ counts, $a=488$ nm, $b=700$ nm, $c=20$ nm; Black dashed line: same as black solid line but with $\sin^{10}(x)$ instead of $\sin^4(x)$ dependence; Red line: Eq. (2) with $I_0=45$ counts, $a=488$ nm, $b=700$ nm.....	81
Figure 3.4 a) Fluorescence intensity of Alexa Fluor® 555 hydrazide covalently immobilized on different substrates (35 nm gold – squares, 100 nm gold –	

diamonds, silicon – circles, triangle – glass) coated with polymer **1** of different thicknesses. Black solid line: Eq. (1) with $I_0=73$ counts, $a=560$ nm, $b=700$ nm, $c=20$ nm; Black dashed line: same as black solid line but with $\sin^{10}(x)$ instead of $\sin^4(x)$ dependence; Red line: Eq. (2) with $I_0=24$ counts, $a=560$ nm, $b=700$ nm.....84

Figure 3.5 a) Scheme for surface treatment to the samples shown in this figure. b) and c): Bright-field images for polished silicon wafer patterned with 35nm gold film inside the squares and circles features; d), e), f), g): the gold patterned silicon substrates similar as shown in b) and c) were coated with polymer **1** of different thicknesses (10nm, 20nm, 40nm, 85nm, respectively) and then incubated in Alexa Fluor 488 conjugated fibrinogen solution (100 µg/ml in PBS) for 5 hours followed by thorough rinsing and drying before fluorescence microscope imaging; m) and n): the gold patterned silicon substrates were coated with polymer **1** of different thicknesses (55nm and 110nm, respectively) and then incubated in Alexa Fluor 555 hydrazide solution (10 µg/ml, pH=5) for 12 hours followed by thorough washing and drying before fluorescence microscope imaging. All scale bars represent 100 µm.....86

Figure 3.6 All substrates here are polished silicon wafers coated with 100 nm homogenous gold film (no metal pattern). The feature contrast shown in all the images is from different polymer film thickness inside and outside the squares after Multiple-step VAMPIR CVD coating. a) Scheme for surface treatment to the samples shown in this figure. The numbers in b), d), e), f), g) show the thicknesses of different areas. b): The gold substrate coated with polymer **1** (44nm inside the squares and 35nm outside the squares) was incubated in Alexa Fluor® 488 conjugated fibrinogen solution (100 µg/ml in PBS) for 5 hours followed by thorough wash and drying. Fluorescence microscope image was taken in the FITC channel; c): Imaging ellipsometry thickness map and line profile for the same sample shown in b) before in contact with the fibrinogen. d), e), f), g): The gold substrate were coated with polymer **1** of different thicknesses in different areas (thicknesses noted in the images), and then incubated in Alexa Fluor® 555 hydrazide solution (10 µg/ml, pH=5) for 12 hours followed by thorough rinsing and drying. Fluorescence microscope images were then acquired in the Cy3 channel. g) shows the same sample as f) with different magnification. All scale bars represent 100 µm.....88

Figure 3.7 Lambda DNA stained with SYBR gold adsorbed and condensed on polymer **2** (with amine group) coated on different substrates with different thicknesses. All the samples were incubated in the DNA solution (50ng/ml) for 30 min followed by thorough rinsing. All scale bars represent 10 µm.....91

Figure 3.8 Linear relationship of precursor feeding amount and the resulted CVD polymer film thickness for the two different types of polymers used in this study.....94

Figure 3.9 Concentration dependence study. Fluorescence intensity of Alexa Fluor 488 conjugated fibrinogen (different concentration from 0.1 to 100 $\mu\text{g}/\text{ml}$ in PBS, 5h) adsorbed on 100 nm polymer 1 coated glass or 45nm polymer 1 coated gold.....	95
Figure 3.10 Concentration dependence study. Fluorescence Intensity of Alexa Fluor 555 hydrazide (different concentration from 0.01 to 10 $\mu\text{g}/\text{ml}$, pH=5, 12h) covalently immobilized on 100 nm polymer 1 coated glass or 60nm polymer 1 coated gold.....	95
Figure 4.1 Scheme of the biodegradable CVD film synthesis by copolymerizing [2.2]paracyclophanes with cyclic ketene acetals.....	101
Figure 4.2 Synthesis scheme of 5,6-benzo-2-methylene-1,3-dioxepane.....	101
Figure 4.3 Synthesis scheme of 2-methylene-1,3-dioxepane.....	103
Figure 4.4 Synthesis scheme of 2-methylene-1,3,6-trioxocane.....	104
Figure 4.5 Copolymerization of [2.2]paracyclophane and 5,6-benzo-2-methylene-1,3-dioepane. The degrading copolymer shown in Figure 4.6 and Figure 4.7 had an initial feeding ratio of [2.2]paracyclophane : 5,6-benzo-2-methylene-1,3-dioepane = 1 : 2.....	107
Figure 4.6 FTIR spectra for the degradation process of the [2.2]paracyclophane and 5,6-benzo-2-methylene-1,3-dioepane copolymer in 5mM KOH isopropanol solution.....	107
Figure 4.7 Thickness change measured by ellipsometry during the degradation process of the [2.2]paracyclophane and 5,6-benzo-2-methylene-1,3-dioepane copolymer in 5mM KOH isopropanol solution.....	108
Figure 5.1 Two-stage CVD process for synthesis of functionalized polymer-coated CNT microstructure arrays.....	117
Figure 5.2 SEM images of polymer-coated CNT microstructures, demonstrating diversity of shapes and heterogeneous in-plane scales obtained through parallel processing of CNTs.....	121
Figure 5.3 SEM images of the sidewalls of the CNT microstructures; (a) after CNT growth, without polymer; (b) after 10 min CVD polymerization (10 nm thickness); (c) after 20 min CVD polymerization (19 nm thickness); (d) after 30 min CVD polymerization (27 nm thickness). The images show that poly[4-trifluoroacetyl- <i>p</i> -xylylene- <i>co-p</i> -xylylene] conformally coats the CNTs and increases their effective diameter, with thicker polymers at longer deposition times. The magnified images	

were taken from the side walls of identical microstructures shown in Figure 5.3.....122

Figure 5.4 Chemical analysis of reactive coating deposited on CNTs; (a) FTIR spectrum of poly[4-trifluoroacetyl-*p*-xylylene-*co-p*-xylylene]; (b) chemical composition of the polymer-coated CNTs determined by XPS.....123

Figure 5.5 Tuning of the mechanical properties of the polymer-CNT microstructures: (a) schematic of test configuration; (b) SEM image of representative microstructure array used for mechanical testing; (c) load-displacement curves, corresponding to data in Table 5.1; (d) schematic of effective length approximation for modelling of mechanical properties.....124

Figure 5.6 Demonstration of selective chemical functionalization of CNT microstructures enabled by the polymer coating: (a, c) CNT structures without polymer coating, with coating and subsequent reaction with a fluorescence probe; (b, d) CNT structures with poly[4-trifluoroacetyl-*p*-xylylene-*co-p*-xylylene] coating and subsequent immobilization of dye coating, exhibiting significant fluorescence enhancement. Structures were densified by infiltration and evaporation of acetone before dye coating to prevent distortion due to capillary forces from the dye solution. The normalized fluorescence intensity (NFI), plotted in (e), is defined as the mean gray value of the CNT structures divided by the mean gray value of flat surface background. Scale bars represent 100 μm129

Figure 5.7 Microthread electrodes (MTE). a-d, Preparation of a MTE: carbon fibres are coated with 800nm poly(*p*-xylylene) (a); the fibre is further coated with a 50-nm-thick layer of poly(*p*-xylylene-4-methyl-2-bromoisobutyrate)-*co*-(*p*-xylylene) (b); poly(ethylene glycol) is covalently grafted onto the doubly coated fibre by ATRP (c); a carbon recording site is exposed at the tip by cutting away the insulation, and the recording site is coated with PEDOT by electrochemical deposition (d). SEM images of a fully assembled, functional MTE (e). The Confocal Raman Spectroscopy analysis of the MTE components is shown in Figure 5.8. EDX analysis is shown in Figure 5.9.....139

Figure 5.8 Raman Spectroscopy Analysis of MTE components. Raman Spectroscopy of bare carbon fibers (black), PEDOT recording tip (red), and poly(*p*-xylylene) coating (blue). Characteristic bands are labeled with their respective wavelengths. This demonstrates that the parylene insulation was present along the sides of the carbon fiber surface. Also, PEDOT was detected at the tip of the device, but not along the insulated sides of the microthread electrode.....140

Figure 5.9 Stepwise EDX Analysis of Microthread Electrodes throughout fabrication. EDX data of MTE component. **a**, Carbon fiber, **b**, Poly(*p*-xylylene), **c**, Poly[*p*-xylylene-4-methyl-2-bromoisobutyrate]-*co*-(*p*-xylylene)]. **d**, PEGMA. **e**, PEDOT. The poly[*p*-xylylene-4-methyl-2-bromoisobutyrate]-*co*-(*p*-xylylene)] and PEGMA coatings were not detectable using Raman Spectroscopy, perhaps due to low

activity of their Raman scattering frequencies. Therefore, EDX was also used to characterize the surface material after each fabrication step. Carbon fiber and parylene-N were not discernable using EDX. The bromine element could be detected after the 50 nm coating with poly[(*p*-xylylene-4-methyl-2-bromoisobutyrate)-*co*-(*p*-xylylene)]. An increase in oxygen was detected as expected after the PEGMA coating. Sulfur was detected in PEDOT at the tip of the assembled Microthread Electrode. This suggests that each component of the fabrication is assembled into the MTE.....141

Figure 5.10 In vitro electrical characterization of MTEs. **a,b**, Electrical characterization of a poly(*p*-xylylene)-coated carbon fibre, a poly(*p*-xylylene)-coated fibre with an exposed carbon tip and a poly(*p*-xylylene)-coated fibre with a recording site of PEDOT:PSS electrodeposited with applied charges of 5, 25, 50, 100, 200 and 400 nC. **a**, Bode magnitude impedance plot showing decreasing impedance with increasing PEDOT deposition across all frequencies. **b**, Bode phase plot showing phase shift towards smaller phases indicative of a change from a capacitive carbon interface to a faradaic PEDOT interface with increasing deposition. The poly(*p*-xylylene)-insulated fibre without an exposed recording site was not plotted because a reliable signal could not be detected. **c**, Cyclic voltammogram showing increasing charge storage capacity with increasing PEDOT deposition in response to voltage cycling of the electrode site.....143

Figure 5.11 Demonstration of bending strength of Microthread Electrode. MTE can withstand substantial bending into, for instance, a loop-knot without any fracturing. Scale bare indicates 100 microns.....144

Figure 5.12 Physical characteristics of the MTEs. **a**, AMTE laid on top of a 10mm silicon electrode. Scale bar, 50 μ m. **b**, FITC–albumin adsorbed onto a 10mm silicon electrode whereas an ATRP-PEGMA surface-coated MTE showed no adsorption. **c**, Bright-field images of FITC–albumin adsorbed onto a poly(*p*-xylylene)-coated device (left) and an ATRP-PEGMA coated device (right). Scale bar, 20 μ m. **d**, The same image as in c under fluorescent microscopy showing less protein adsorption onto the PEGMA surface (right) compared with the poly(*p*-xylylene) surface (left). **e**, Comparison of the intensity of adsorbed FITC–albumin between PEGMA-coated MTEs and silicon probes (left), and PEGMA coated MTEs and poly(*p*-xylylene)-coated MTEs. Error bars show s.d.....146

Figure 6.1 Multidisciplinary collaborative efforts for designing and producing integrated biomedical devices.....164

LIST OF TABLES

Table 2.1 Chemical Composition of polymers 1, 2 and 3 in atom-% shown as experimental values determined by XPS. Theoretically calculated compositions are included for comparison.....	55
Table 5.1 Summary of measurements of polymer-coated CNT microstructures, along with parameter estimates calculated by effective elasticity model.....	125
Table 6.1 Applications summary of the functionalized [2.2]paracyclophane CVD polymerization.....	159

ABSTRACT

Chemical vapor deposition (CVD) of reactive polymer coatings is an ideal technique for surface functionalization, modification and encapsulation. In this dissertation, surface designs for four different biomedical application areas based on the CVD polymerization platform are presented.

Precision immobilization strategies for surface tethering multiple biomolecules are discussed in Chapter 2. Orthogonal immobilization strategies are developed based on orthogonally functionalized multipotent polymer coatings. Three specific studies are included in this chapter. Highly efficient and orthogonal bioconjugation reactions are employed, including the alkyne-azide “click” reaction, the hydrazide-aldehyde reaction and the active ester-amine reaction.

For potential biosensor development, metal enhanced fluorescence on reactive CVD polymer coated gold films is studied and presented in Chapter 3. Functional CVD polymer coatings with nanoscale thicknesses are used as spacer layers and the surface enhanced fluorescence effect is demonstrated. The fluorescence intensity oscillates with the polymer spacer layer thickness, ranging from highly enhanced (up to 18 fold compared to the polymer coated glass) to completely turn-off.

Chapter 4 reports for the first time a method for synthesizing biodegradable CVD polymer films. Degradability is an essential requirement for tissue engineering

and other biomedical applications. Degradable CVD polymer films with ester groups in the polymer backbone have not been reported before. They combine the benefits of the CVD coatings with complete degradability. Functional groups can also be introduced into the degradable polymer structure.

Two different studies are presented in Chapter 5 to exemplify the applications of reactive CVD polymer coatings on complex structures and integrated devices. The first study describes a two-step CVD method for fabrication of hierarchical polymer-coated carbon nanotube microstructures with tunable mechanical properties and accessible chemical functionality. Ultrasmall implantable composite microelectrodes with functional CVD coatings for chronic neural recordings are presented as the second example. These studies demonstrate easy integration of the CVD polymer coating into micro- or nano- device fabrications. The CVD coatings not only provide desired chemical composition changes to the surface, but also improve mechanical and electrical properties of the integrated structures and devices.

In summary, the vapor-based reactive/functional polymer coatings provide a powerful platform for biointerface design and research.

CHAPTER 1

Introduction

1.1 Motivation

Over the past half-century, we have seen tremendous development in biomedical technologies along with the recent advances in medicine, molecular biology, materials science, computers and electronics, spectroscopic techniques and other characterization methods.¹ Biointerface, a critical aspect to consider in many biomedical applications, has attracted attention in many interdisciplinary research areas such as medical implants, tissue engineering, biosensors and biochips, bioelectronics, artificial photosynthesis and biomimetic materials.¹⁻² Early efforts focused on biologically inert materials and surfaces with minimal biological response due to poor understanding of cell-surface interaction mechanisms.^{1b, 3} Recent progress in cell and molecular biology has provided us with rich information on how biomolecules affect cellular processes and eventually the functions of tissues and organs.^{1b, 3} This enables us to actively design surfaces and incorporate instructive biological cues into the biointerface to guide biological responses.^{1b, 3}

With this goal in mind, we are in search of an ideal surface modification platform that can meet the following three criteria: (1) Surface functionalization-it provides functional groups for precise immobilization of biomolecules according to specific needs; (2) Wide applicability-it is preferably substrate-independent, and

applicable to 3D substrates with complex geometries; (3) Easy integration in micro- and nano- fabrication processes.

Chemical vapor deposition (CVD) polymerization process of functionalized [2.2]paracyclophanes is the surface modification platform used in this dissertation. This process meets all three of the above-mentioned criteria. More details and comparison with other methods are elaborated below.

Surface Functionalization

Non-functionalized chemical vapor deposition of [2.2]paracyclophanes was developed by Gorham at Union Carbide in the 1960s.⁴ The polymer product of this process is called poly(p-xylylene) (PPX), commercially developed under the parylene brand (including parylene N, parylene C, and parylene D).⁵ In the Gorham CVD process, [2.2]paracyclophane is sublimated in the vapor phase in vacuum, pyrolyzed, followed by adsorption/condensation of the pyrolysis products on cooled substrates and simultaneous polymerization, forming solvent-free and pinhole-free films.^{4, 6} Since this development, many functionalized/substituted [2.2]paracyclophanes were synthesized by organic chemists and used in the CVD process to produce polymer films with a wide variety of functional groups.⁷ Figure 1.1 shows the CVD polymerization scheme for substituted [2.2]paracyclophanes and the functional groups library used to accommodate specific application needs. This library includes many commonly used functional groups such as aldehyde, ketones, amine, alkyne, vinyl, maleimide, anhydride, active ester, hydroxyl, fluorine, photo-reactive benzoyl group and initiator groups for atom transfer radical polymerization (ATRP) and reversible addition-fragmentation chain-transfer (RAFT)

polymerization. This established and constantly updating functional group library is the most prominent advantage for using the CVD polymerization as a surface modification/surface design platform. Moreover, the CVD polymerization process can introduce multiple functional groups on the surface with defined ratios and generate functional group gradients,⁸ which are not easily achievable by other surface modification methods. Subsequently, a wide variety of biomolecules (proteins, peptides, DNAs) can be immobilized on the functional/reactive coatings through bioconjugation chemistries.⁹

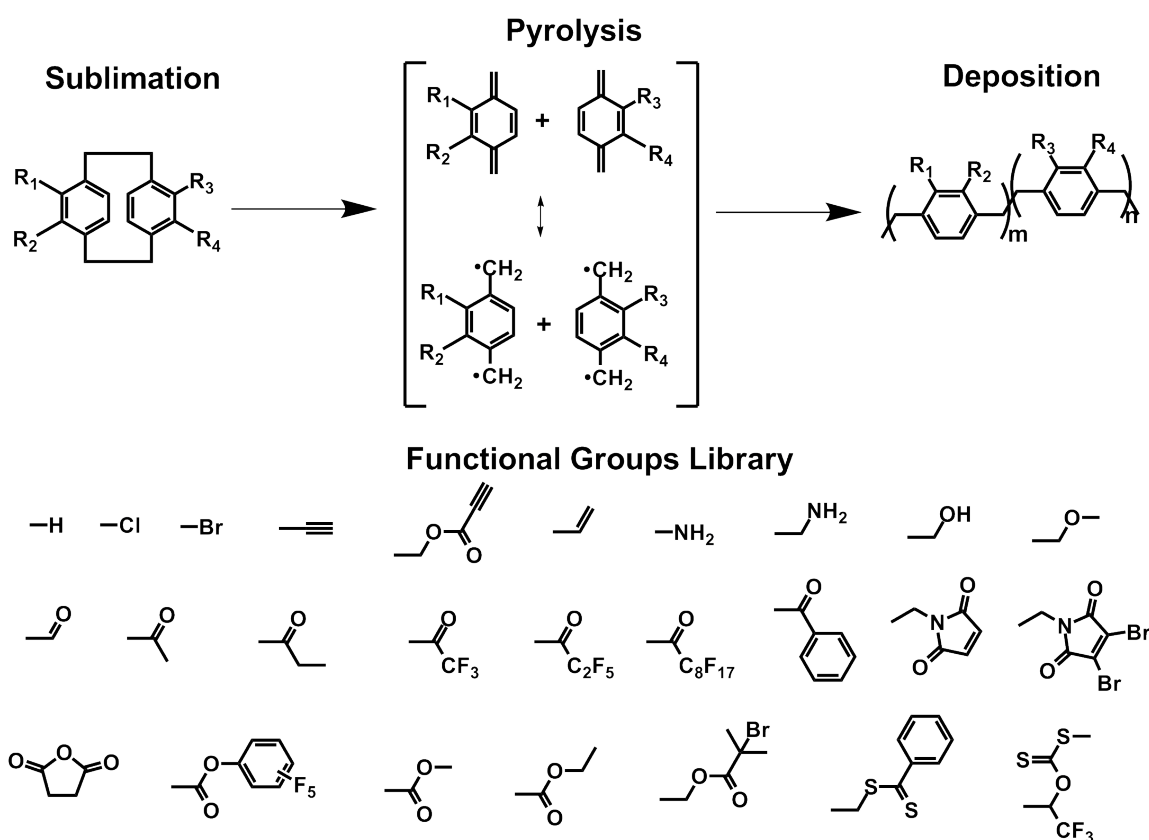


Figure 1.1 CVD polymerization scheme for the substituted [2.2]paracyclophanes and the established functional groups library.

Widely Applicability and Substrate-Independence

In biomedical applications, surface modification is meant to retain the key bulk material properties while modifying the surface to improve biocompatibility.¹⁰ Thus, substrate-independent methods are better than substrate-dependent surface modification chemistries such as the commonly used silane chemistries for silica or silica-like substrates and thiol chemistries for gold substrates. CVD polymerization is a versatile coating process that decouples the surface chemistry from the bulk material composition.¹¹ It not only can be used for flat surfaces but also can conformally coat 3D structures with complex geometries.^{7, 11} This makes CVD polymerization a surface functionalization platform for coating and functionalizing almost any solid surface as long as the materials are stable under vacuum at room temperature or below. The CVD polymerization of [2.2]paracyclophanes has been used in a wide range of electronic and biomedical applications, such as gate insulators,¹² organic light-emitting devices,¹³ implanted microelectrodes,¹⁴ micro PCR chips,¹⁵ stents,¹⁶ pacemakers,¹⁷ CMOS based chemical sensors,¹⁸ BioMEMS (biomedical or biological micro-electro-mechanical systems),¹⁹ or drug releasing.²⁰ Due to their good biocompatibility, the FDA has approved PPX derivatives, such as Parylene C and Parylene N as Class VI polymers.¹⁶ The good biocompatibility inspires us to further study biomedical surface design based on functionalized PPXs polymer coatings for this dissertation.

Easy Integration in Micro- and Nano- Fabrication Processes

Miniaturization is a clear trend not only for electronics but also for biomedical devices.^{1b} It enables us to achieve better precision, high throughput and lower cost.^{1b} Many experiments need to be performed at the precision of a single cell, which requires device miniaturization. For instance, recording signals from a single neuron requires that the neural probe/cell contacting area be smaller than the size of a neuron (more details on this are discussed in Chapter 5). As for high throughput, DNA and protein microarrays are cases in point. Techniques such as array-based integrated chips, microfluidics and soft lithography are all high-throughput approaches for systematically analyzing biomolecules.²¹ In terms of cost, miniaturized engineered biosystems can lower the expensive biological reagent volumes needed for the assays, shorten reaction times and allow multiple analyses performed in series or in parallel.^{1b} All these benefits lead to significant cost reduction. The popular and important concepts of BioMEMs, total microanalysis and lab-on-a-chip are all generated from the need for miniaturization. For the best performance of miniaturized systems, a widely applicable surface modification method, which can easily integrate into the micro- and nano-fabrication processes, becomes an essential need. The reactive coatings platform *via* CVD polymerization provides the solution on demand here. Previous studies have demonstrated its successful application in functionalizing microfluidic channels,²² coating 3D structures with complex shapes²³ or high aspect ratios¹¹ and generating micro- and nano- patterns.²³⁻²⁴ This advantage is also shown in the specific studies included in this dissertation.

In summary, CVD polymerization of functionalized [2.2]paracyclophanes is an excellent surface functionalization platform for biomedical applications. The specific surface designs are demonstrated in different studies included in this dissertation.

1.2 Overview of the Dissertation

The biomedical surface design based on the CVD polymerization platform is studied in four different aspects. Figure 1.2 shows the four aspects with specific studies included in different chapters of this dissertation.

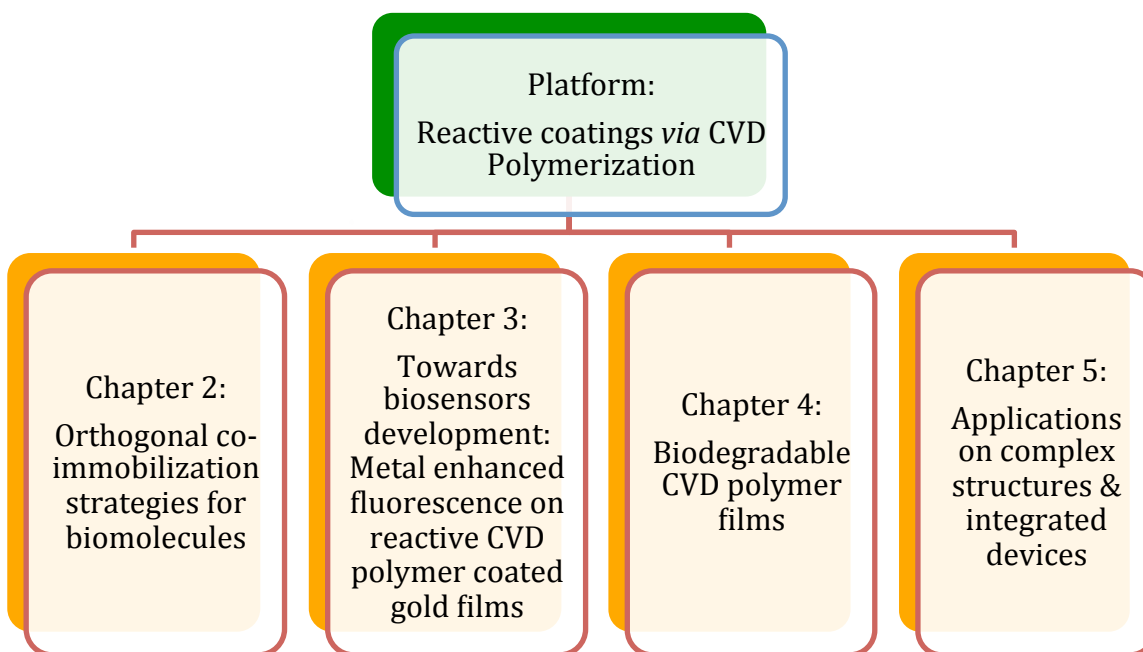


Figure 1.2 Overview of the four different aspects of biomedical surface design based on CVD polymerization platform in this dissertation.

Chapter 2 discusses the precision immobilization strategies when more than one biomolecule needs to be tethered to the surface. Because it is not as straightforward as single-molecule immobilization, orthogonal immobilization strategies are developed. Three specific studies are included in this chapter.

Chapter 3 describes metal enhanced fluorescence on reactive CVD polymer coated gold films. This study shows the advantages of using the functional polymer as spacer layer for modulating fluorescence intensity of surface immobilized fluorescent molecules on gold. It is potentially very useful for biosensor applications.

Chapter 4 explores a method to synthesize biodegradable CVD polymer films. Degradability is an essential requirement for materials used in packaging and some biomedical applications such as tissue engineering. The degradable CVD polymer film, which has not been reported before, has both the benefits of the vapor-based polymer coatings and complete degradability. Functional groups can also be introduced to the degradable coating.

Chapter 5 includes two different studies to exemplify the applications of reactive CVD polymer coatings on complex structures and integrated devices. This shows that our coating platform can be easily integrated in micro- or nano- device fabrications.

References

1. (a) Chilkoti, A.; Hubbell, J. A., Biointerface science. *Mrs Bull* **2005**, *30* (3), 175-176; (b) Ratner, B. D.; Bryant, S. J., Biomaterials: Where we have been and where we are going. *Annu Rev Biomed Eng* **2004**, *6*, 41-75; (c) Castner, D. G.; Ratner, B. D., Biomedical surface science: Foundations to frontiers. *Surf Sci* **2002**, *500* (1-3), 28-60.
2. Kasemo, B., Biological surface science. *Surf Sci* **2002**, *500* (1-3), 656-677.
3. Gersbach, C. A., 5.510 - Engineered Bioactive Molecules. In *Comprehensive Biomaterials*, Editor-in-Chief: Paul, D., Ed. Elsevier: Oxford, 2011; pp 131-145.
4. Gorham, W. F., A New, General Synthetic Method for the Preparation of Linear Poly-p-xylylenes. *Journal of Polymer Science Part A-1: Polymer Chemistry* **1966**, *4* (12), 3027-3039.
5. Lahann, J., Vapor-based polymer coatings for potential biomedical applications. *Polym Int* **2006**, *55* (12), 1361-1370.
6. Simon, P.; Mang, S.; Hasenhindl, A.; Gronski, W.; Greiner, A., Poly(p-xylylene) and its derivatives by chemical vapor deposition: Synthesis, mechanism, and structure. *Macromolecules* **1998**, *31* (25), 8775-8780.
7. Chen, H. Y.; Lahann, J., Designable Biointerfaces Using Vapor-Based Reactive Polymers. *Langmuir* **2011**, *27* (1), 34-48.
8. (a) Elkasabi, Y.; Chen, H. Y.; Lahann, J., Multipotent polymer coatings based on chemical vapor deposition copolymerization. *Adv Mater* **2006**, *18* (12), 1521-+; (b) Elkasabi, Y.; Lahann, J., Vapor-Based Polymer Gradients. *Macromol Rapid Comm* **2009**, *30* (1), 57-63.
9. (a) Lahann, J.; Balcells, M.; Rodon, T.; Lee, J.; Choi, I. S.; Jensen, K. F.; Langer, R., Reactive polymer coatings: A platform for patterning proteins and mammalian cells onto a broad range of materials. *Langmuir* **2002**, *18* (9), 3632-3638; (b) Lahann, J.; Klee, D.; Pluester, W.; Hoecker, H., Bioactive immobilization of r-hirudin on CVD-coated metallic implant devices. *Biomaterials* **2001**, *22* (8), 817-826; (c) Thevenet, S.; Chen, H. Y.; Lahann, J.; Stellacci, F., A generic approach towards nanostructured surfaces based on supramolecular nanostamping on reactive polymer coatings. *Adv Mater* **2007**, *19* (24), 4333-+.
10. Kurella, A.; Dahotre, N. B., Review paper: Surface modification for bioimplants: The role of laser surface engineering. *J Biomater Appl* **2005**, *20* (1), 5-50.
11. Alf, M. E.; Asatekin, A.; Barr, M. C.; Baxamusa, S. H.; Chelawat, H.; Ozaydin-Ince, G.; Petruczok, C. D.; Sreenivasan, R.; Tenhaeff, W. E.; Trujillo, N. J.; Vaddiraju, S.; Xu, J.; Gleason, K. K., Chemical Vapor Deposition of Conformal, Functional, and Responsive Polymer Films. *Adv Mater* **2010**, *22* (18), 1993-2027.
12. Podzorov, V.; Pudalov, V. M.; Gershenson, M. E., Field-effect transistors on rubrene single crystals with parylene gate insulator. *Appl Phys Lett* **2003**, *82* (11), 1739-1741.
13. Ghosh, A. P.; Gerenser, L. J.; Jarman, C. M.; Fornalick, J. E., Thin-film encapsulation of organic light-emitting devices. *Appl Phys Lett* **2005**, *86* (22).
14. Schmidt, E. M.; Mcintosh, J. S.; Bak, M. J., Long-Term Implants of Parylene-C Coated Microelectrodes. *Med Biol Eng Comput* **1988**, *26* (1), 96-101.

15. Shin, Y. S.; Cho, K.; Lim, S. H.; Chung, S.; Park, S. J.; Chung, C.; Han, D. C.; Chang, J. K., PDMS-based micro PCR chip with parylene coating. *J Micromech Microeng* **2003**, *13* (5), 768-774.
16. Westedt, U.; Wittmar, M.; Hellwig, M.; Hanefeld, P.; Greiner, A.; Schaper, A. K.; Kissel, T., Paclitaxel releasing films consisting of poly(vinyl alcohol)-graft-poly(lactide-co-glycolide) and their potential as biodegradable stent coatings. *J Control Release* **2006**, *111* (1-2), 235-246.
17. Dery, J. P.; Gilbert, M.; O'Hara, G.; Champagne, J.; Desaulniers, D.; Cartier, P.; Philippon, F., Pacemaker contact sensitivity: Case report and review of the literature. *Pace* **2002**, *25* (5), 863-865.
18. Prodromakis, T.; Michelakis, K.; Zoumpoulidis, T.; Dekker, R.; Toumazou, C., Biocompatible Encapsulation of CMOS based Chemical Sensors. *2009 Ieee Sensors, Vols 1-3* **2009**, 791-794.
19. Meng, E.; Tai, Y. C., Parylene etching techniques for microfluidics and biomems. *Proc Ieee Micr Elect* **2005**, 568-571.
20. Zeng, J.; Aigner, A.; Czubayko, F.; Kissel, T.; Wendorff, J. H.; Greiner, A., Poly(vinyl alcohol) nanofibers by electrospinning as a protein delivery system and the retardation of enzyme release by additional polymer coatings. *Biomacromolecules* **2005**, *6* (3), 1484-1488.
21. Bashir, R., BioMEMS: state-of-the-art in detection, opportunities and prospects. *Adv Drug Deliver Rev* **2004**, *56* (11), 1565-1586.
22. Chen, H. Y.; Elkasabi, Y.; Lahann, J., Surface modification of confined microgeometries via vapor-deposited polymer coatings. *J Am Chem Soc* **2006**, *128* (1), 374-380.
23. Chen, H. Y.; Rouillard, J. M.; Gulari, E.; Lahann, J., Colloids with high-definition surface structures. *P Natl Acad Sci USA* **2007**, *104* (27), 11173-11178.
24. (a) Jiang, X. W.; Chen, H. Y.; Galvan, G.; Yoshida, M.; Lahann, J., Vapor-based initiator coatings for atom transfer radical polymerization. *Adv Funct Mater* **2008**, *18* (1), 27-35; (b) Chen, H. Y.; Hirtz, M.; Deng, X. P.; Laue, T.; Fuchs, H.; Lahann, J., Substrate-Independent Dip-Pen Nanolithography Based on Reactive Coatings. *J Am Chem Soc* **2010**, *132* (51), 18023-18025.

CHAPTER 2

Orthogonal Co-Immobilization Strategies for Biomolecules Based on Multifunctional Chemical Vapor Deposition Polymer Coatings

This chapter has been adapted from the following published articles with minor modifications (Reproduced by permission of Wiley):

1. Deng, X., Friedmann, C. and Lahann, J. (2011), Bio-orthogonal “Double-Click” Chemistry Based on Multifunctional Coatings. *Angew. Chem. Int. Ed.*, 50: 6522–6526.

2. Deng, X., Eyster, T. W., Elkasabi, Y. and Lahann, J. (2012), Bio-Orthogonal Polymer Coatings for Co-Presentation of Biomolecules. *Macromol. Rapid Commun.*, 33: 640–645.

3. Deng, X. and Lahann, J. (2012), A Generic Strategy for Co-Presentation of Heparin-Binding Growth Factors Based on CVD Polymerization. *Macromol. Rapid Commun.*, 33: 1459–1465.

As a consequence of recent progress in biotechnology, regenerative medicine, and developments concerning medical implants, an increasing need for precise and flexible conjugation methods has emerged.¹ For the immobilization of biomolecules, chemical reactions with high specificity towards the molecule of

interest, mild reaction conditions compatible with physiological milieu, and rapid as well as quantitative conversion are essential.² If defined immobilization of two or more biomolecules on the same surface in controlled ratios is required, the individual reactions not only need to be orthogonal with respect to ongoing biological events, but also with respect to each other.³ This prerequisite puts major constraints on the type of chemical reactions that can be exploited for bio-orthogonal immobilization. The development of bio-orthogonal reaction schemes has been heavily influenced by the concept of “click” chemistry, which was first introduced by Sharpless and co-workers in 2001.⁴ As the archetypal example of click chemistry, the copper(I)-catalyzed Huisgen 1,3-dipolar cycloaddition of azides and terminal alkynes (CuAAC) has since been widely used as a surface modification strategy.⁵ CuAAC is a highly efficient reaction under mild conditions, with complete regioselectivity for the 1,4-triazole product.⁶ Triazoles are stable linkers that are resistant to hydrolysis, oxidation, or reduction.^{6b} Initial work was conducted on model surfaces, such as gold⁷ and silicon,⁸ but was recently extended to a wide range of different substrates.⁹

Chemical vapor deposition (CVD) polymerization is a versatile coating process that effectively decouples the surface chemistry from the bulk composition.¹⁰ The CVD polymerization of functionalized [2.2]paracyclophanes can result in functionalized poly(*p*-xylylene) coatings with a wide range of different groups including aldehyde, ketones, amine, alkyne, vinyl, anhydride, active ester, hydroxyl, fluorine, photo-reactive benzoyl group and bromoisobutyrate group for initiating atom transfer radical polymerization.¹¹ These coatings have been used for

the immobilization of proteins,¹² peptides,¹³ DNA,¹⁴ and cells.¹⁵ CVD coatings can be conformally deposited on a broad range of materials with different geometry¹⁰ and are useful for applications including functional electrically conductive polymer films,¹⁶ polymer gradients,¹⁷ protein-resistant surfaces,¹⁸ solventless adhesive bonding,¹⁹ 3D photoresists,²⁰ and polymer/carbon nanotube composites.²¹ This powerful platform to functionalize virtually any solid surface also allows us to apply different functional groups on the same surface by copolymerization^{3b} or surface micro-engineering.²²

In this chapter, three different combinations of bio-orthogonal reactions for biomolecule immobilizations on three different multifunctional polymer coatings (Figure 2.1) are explored. An invariable component for the three combinations we tried is the alkyne functional group (R_1), which can react with azide *via* CuAAC. R_2 changes with different combinations of the orthogonal reactions. For the first combination, R_2 is an alkyne with an electron-withdrawing ester group, which makes the alkyne-azide cycloaddition occur without the copper catalyst. This allows us immobilize two different biomolecules with azide group sequentially, first without and then with copper catalyst (Section 2.1).²² For the second combination, we choose pentafluorophenyl ester (Pfp-ester) as R_2 . Pfp-ester is an active ester that can rapidly react with amine to form amide bond with no side reactions under mild conditions, thus suitable for one-step immobilizations of proteins onto surfaces (Section 2.2).²³ Another well-known bio-orthogonal reaction is the aldehyde-hydrazide condensation, which is used after the surface is coated with polymer **3** (section 2.3).²⁴

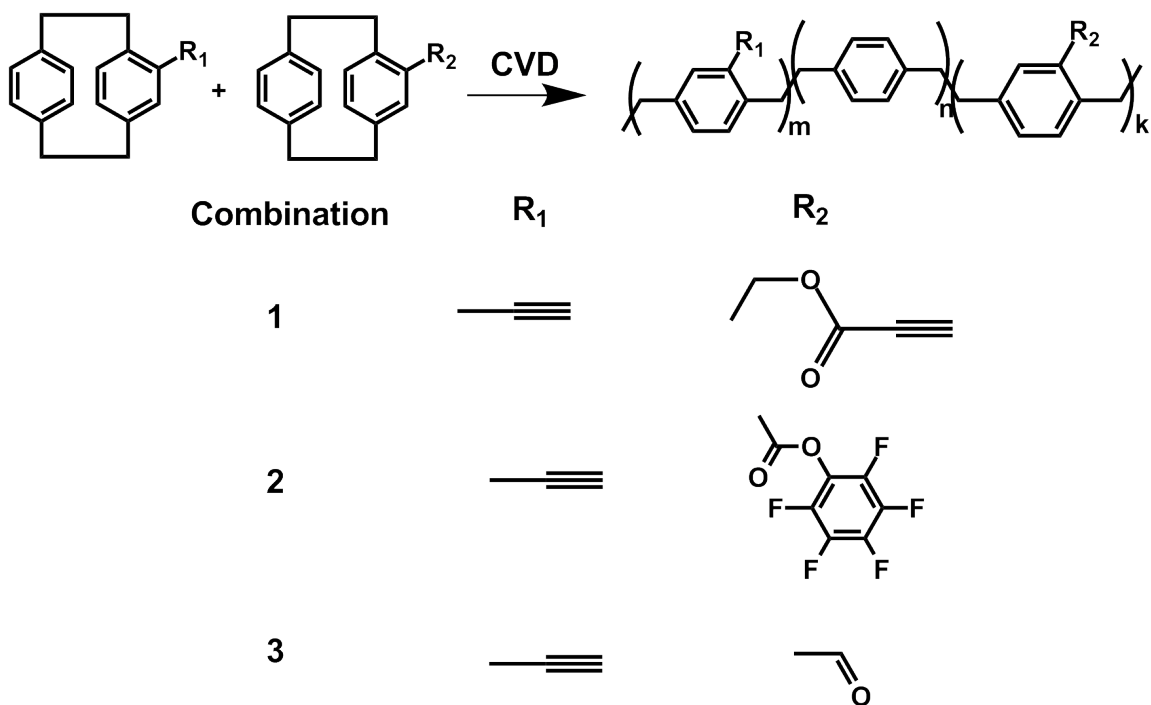


Figure 2.1 Combinations of chemical functional groups for orthogonal immobilizations of multiple biomolecules.

After picking the chemistry combination, we also need to consider the spatial arrangement of the functional groups. Two methods were used to apply multiple functional groups on surface. First, by copolymerizing paracyclophanes with different functional groups as outlined in Figure 2.1, we got homogeneous copolymer films with the two different functional groups distributed randomly everywhere (Figure 2.2a). This is ideal for applications requiring two immobilized molecules evenly distributed and close together. In addition, more than two functional groups can present on the same surface by introducing more paracyclophanes with other orthogonal functional groups (R₃, R₄...). The second method is generating micro-engineered surfaces (Figure 2.2b) with the vapor-assisted micropatterning in replica structures (VAMPIR) technique previously

developed in the Lahann group.^{18, 25} In this case, the two functional groups were distributed in separated yet defined areas on the surface. This is desired for applications requiring patterned surface and it is more convenient for directly observing the orthogonality of the reactions used for the two different functional groups. Details of specific studies are described below in sections 2.1, 2.2 and 2.3.

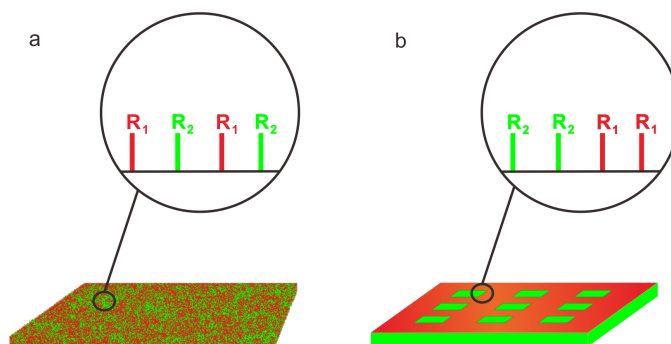


Figure 2.2 Two types of spatial arrangements for the orthogonal functional groups.

2.1 Bio-Orthogonal "Double-Click" Chemistry Based on Multifunctional Coatings

2.1.1 Introduction

The CVD process has been successfully applied for the deposition of alkyne-functionalized polymers on a range of different substrates and can even support micro- and nanopatterning by CuAAC.^{8b,9} Despite the success of CuAAC, the requirement of a potentially cytotoxic copper catalyst may limit its biomedical applications.²⁶ To develop Cu-free click chemistry, alkynes were activated by applying ring-strain, incorporating an electron-withdrawing group, or both.^{26a}

Bertozzi and co-workers conducted extensive studies on the synthesis of cyclooctyne derivatives for copper-free azide-alkyne cycloadditions.²⁷ They successfully improved the cyclooctyne reactivity by introducing electron-withdrawing fluorine atoms and used the copper-free click reactions for selective modifications of biomolecules and living cells.²⁷ Boons and co-workers achieved a similar rate enhancement by fusing two aryl rings to the cyclooctyne scaffold.²⁸ The strain-promoted cycloaddition of functionalized cyclooctynes to azides is an efficient reaction, but their challenging synthesis has prevented them from being more widely investigated and applied to bioimmobilization.^{26a}

Herein, we report a synthetically straightforward approach towards reactive coatings for copper-free 1,3-dipolar cycloadditions and demonstrate a bio-orthogonal reaction scheme based on two sequential click reactions. Our approach is based on CVD polymerization of appropriately functionalized

[2.2]paracyclophanes. The development of a CVD coating that presents alkyne groups capable of copperfree click chemistry poses a number of challenges: 1) The reactive groups must readily react with azide groups at room temperature in benign solvents (e.g., water); 2) The functional groups have to be compatible with the processing conditions during CVD polymerization without decomposition or side reactions; 3) The precursors should be accessible by straightforward synthesis. Herein, we chose to synthesize [2.2]paracyclophane-4-methyl propiolate, which provides an electron-deficient alkynyl group for the spontaneous reaction with azide groups even in the absence of a catalyst. Neighboring electron-withdrawing groups are known to increase the reactivity of alkyne groups.^{26a} Functional moieties such as sulfonyl and carbonyl groups were investigated in different studies.²⁹ Applications of electron-deficient alkyne moieties include DNA modification, gold nanoparticle functionalization, or hydrogel crosslinking.^{29b, 30}

2.1.2 Experimental Section

Synthesis of [2.2]Paracyclophane-4-methyl propiolate

All chemicals were purchased from Aldrich and VWR and used without further purification. Routine monitoring of reactions was performed using Silica gel coated alumina plates (silica gel 60), which were analyzed under UV-light at 254 nm. ¹H-NMR and ¹³C-NMR spectra were recorded on a Bruker Avance III spectrometer as solutions. Mass spectra were recorded on a Finnigan MAT95. IR spectra were recorded on a Bruker Alpha T using ATR (attenuated total reflectance) sampling technique. Melting points were measured on a Stanford Research Systems Optimelt.

The synthesis of 4-ethynyl[2.2]paracyclophane was described elsewhere.^{8b}

[2.2]Paracyclophane-4-methyl propiolate was synthesized from previously published 4-hydroxymethyl[2.2]paracyclophane.¹⁸ 4-Hydroxymethyl[2.2]paracyclophane (2.53 g, 10.6 mmol) and 4-dimethylaminopyridine (13.0 mg, 0.11 mmol) were dissolved in dichloromethane (60 mL). Propiolic acid (724 μ l, 820 mg, 11.7 mmol) was added and the solution was cooled to 0 °C. Then *N,N'*-diisopropylcarbodiimide (1.82 mL, 1.48 g, 11.6 mmol) was added dropwise over 10 minutes and the mixture was warmed to room temperature and stirred for another 6 hours. The solvent was evaporated in vacuo and the residue was purified by column chromatography (eluent: dichloromethane/hexane 2:1). [2.2]Paracyclophane-4-methyl propiolate (2.38g, 77%) was obtained as a white solid.

¹H NMR (500 MHz, CDCl₃): 6.60 (dd, *J* = 7.9 Hz, 1.8 Hz, 1H, CH), 6.57–6.48 (m, 4H, CH), 6.41–6.38 (m, 2H, CH), 5.18 (d, *J* = 12.4 Hz, 1H, CH₂O), 4.99 (d, *J* = 12.4 Hz, 1H, CH₂O), 3.35 (ddd, *J* = 13.5 Hz, 10.2 Hz, 2.3 Hz, 1H, CH₂), 3.17 (ddd, *J* = 13.4 Hz, 11.0 Hz, 2.4 Hz, 1H, CH₂), 3.14–2.97 (m, 5H, CH₂), 2.92 (ddd, *J* = 13.7 Hz, 10.8 Hz, 5.8 Hz, 1H, CH₂), 2.88 (s, 1H, CH) ppm. ¹³C NMR (125 MHz, CDCl₃): 152.7, 140.3, 139.6, 139.1, 138.5, 135.2, 134.1, 133.4, 133.3, 133.2, 132.9, 132.2, 129.7, 75.0, 74.6, 67.0, 35.2, 34.9, 34.5, 32.9 ppm.

EI-MS [70 eV, *m/z* (%): 290 (9) [M⁺], 220 (14) [C₁₇H₁₆⁺], 132 (36) [C₉H₈O⁺], 104 (100) [C₈H₈⁺], 77 (38) [C₆H₅⁺]. HR-MS (EI): 290.1307 (calculated for [M⁺], C₂₀H₁₈O₂), 290.1304 (observed).

FT-IR (ATR): 3259 (vw), 2923 (vw), 2850 (vw), 2116 (vw), 1696 (w), 1497 (vw), 1461 (vw), 1435 (vw), 1413 (vw), 1377 (vw), 1250 (w), 1221 (m), 953 (w), 903 (w), 873 (vw), 797 (w), 753 (w), 716 (w), 643 (w), 616 (vw), 578 (w), 512 (w), 479 (vw), 410 (vw) cm⁻¹.

m.p.: 145 °C.

CVD Polymerization

Poly[(4-ethynyl-*p*-xylylene)-*co*-(*p*-xylylene)] (**1**) and poly[(*p*-xylylene-4-methyl-propiolate)-*co*-(*p*-xylylene)] (**2**) were synthesized via CVD polymerization as shown in Figure 2.3. The CVD process was carried out at 0.07 Torr, with 20 sccm argon as carrier gas. The precursor was sublimed at 90-110°C in vacuum and converted into corresponding diradical by pyrolysis (>500°C). The diradicals spontaneously polymerized on the cooled (15°C) substrate placed on top of a rotating stage. The pyrolysis temperature was set to be 670 °C for polymer **1** and 510 °C for polymer **2**. The resulted film thickness was around 50 nm for all the experiments. To generate micro-engineered surface by 2-step CVD as shown in Figure 2.7, polymer **1** was first coated on the whole surface, followed by polymer **2** coated on selected areas of the surface with the help of PDMS microstencil. The fabrication of PDMS microstencil was described in our previous papers.^{18, 25}

Surface Characterization

IR spectra were recorded on a Nicolet 6700 spectrometer with the grazing angle accessory (Smart SAGA) at a grazing angle of 80°. XPS were performed on an Axis Ultra X-ray photoelectron spectrometer (Kratos Analyticals, UK) equipped with a monochromatized AlK α X-ray source. All spectra were calibrated with respect to

the non-functionalized aliphatic carbon with a binding energy of 285.0 eV. Thicknesses were measured on silicon substrate by Imaging Spectroscopic Ellipsometer (Accurion, Nanofilm EP³-SE). Ellipsometric parameters were fitted using Cauchy model. Both multi-wavelength 4-zone nulling and mapping experiments were performed at an angle of incidence of 70°. The imaging lateral resolution is ~2 micron for the 10× objective.

Surface Immobilization

For microcontact printing, PDMS stamps were inked with water solution of Biotin-dPEG[®]₃₊₄-azide (10mg/ml, Quanta BioDesign, Ltd.) and printed for 3 h on different polymer surfaces. After thorough washing, the samples were incubated in TRITC conjugated streptavidin (10µg/ml, Fisher Scientific) in PBS containing 0.1 % (w/v) bovine albumin and Tween 20 (0.02 % (v/v)) for 1 h. Subsequently, the samples were washed, dried and observed under fluorescence microscope (Nikon Eclipse 80i).

Similarly, for solution reactions on microengineered surfaces, samples were incubated in solution of Biotin-dPEG[®]₃₊₄-azide (10mg/ml, without copper for Figure 2.6 and with copper for Figure 2.7) for 12h followed by washing and TRITC-streptavidin incubation described above. For the experiment in Figure 2.7, the sample was first incubated in copper-free water solution of Oregon Green[®] 488 azide (20µg/ml, Invitrogen) for 12h. Subsequently, the sample was washed and incubated in Biotin-dPEG[®]₃₊₄-azide solution with sodium ascorbate (50mg/ml) and copper sulfate (0.1mM).

2.1.3 Results and Discussion

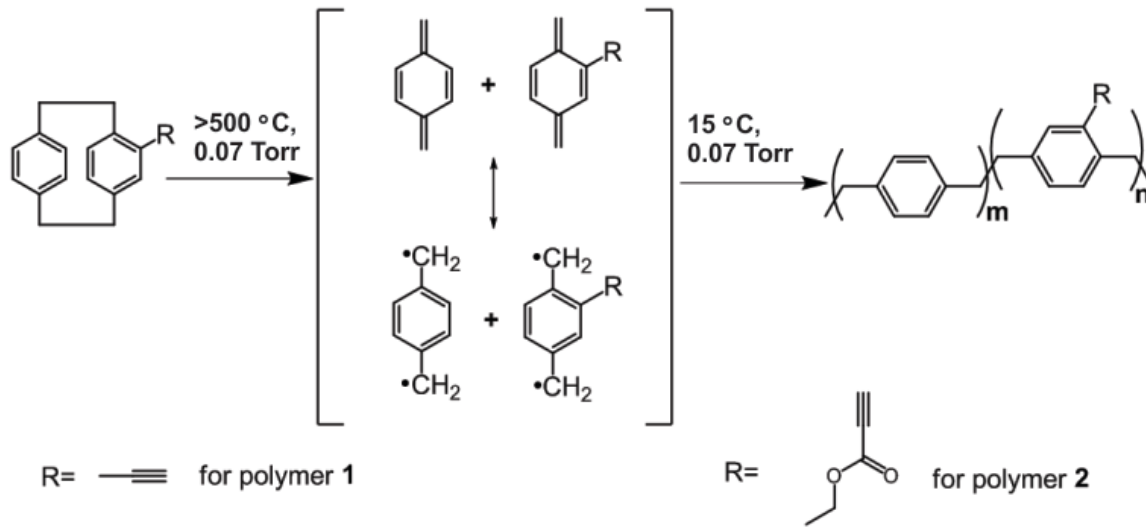
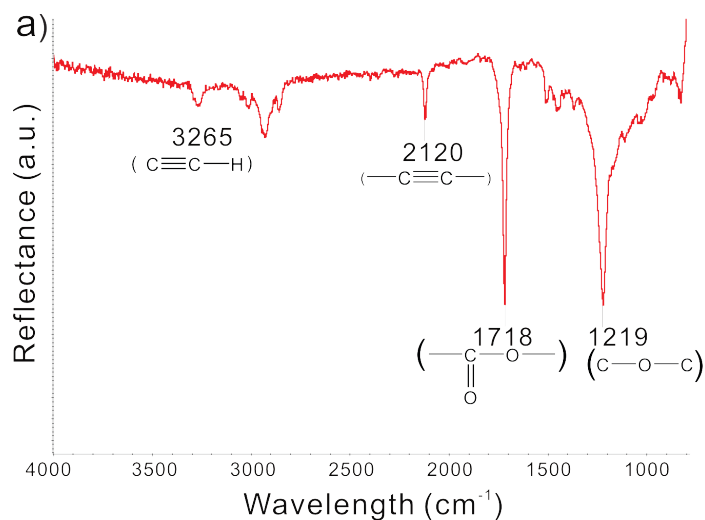


Figure 2.3 CVD polymerization process of polymers with inactivated (1) and activated alkyne groups (2).

As shown in Figure 2.3, [2.2]paracyclophane-4-methyl propiolate was sublimed at 100 °C and 0.07 Torr and then subjected to thermal pyrolysis at 510 °C in vacuum to generate reactive species that spontaneously polymerized upon adhesion onto the cooled substrate, which was maintained at 15 °C. This procedure resulted in a homogenous polymer film that was stable in aqueous solutions and organic solvents such as ethanol, acetone, dichloromethane, or chloroform.



b)	B.E. (eV)	Experimental [%]	Calculated [%]
<u>C</u> -C/H	285.0	73.7	77.5
<u>C</u> -C=O	285.8	4.3	4.5
<u>C</u> -O	286.8	5.5	4.5
O- <u>C</u> =O	289.2	4.3	4.5
$\pi \rightarrow \pi^*$	291.3	3.1	-
O-C= <u>O</u>	532.6	4.7	4.5
O=C- <u>O</u>	534.0	4.4	4.5

Figure 2.4 a) FTIR spectrum for poly[(*p*-xylylene-4-methyl-propiolate)-*co*-(*p*-xylylene)] (**2**); b) chemical composition of polymer **2** determined by XPS. Experimental values are compared with calculated values. Spectra are shown in supplemental Figure 2.8.

FTIR spectroscopy and X-ray photoelectron spectroscopy (XPS) were used to assess the chemical structure of this newly synthesized polymer film and confirmed that the resulting polymer was indeed poly[(*p*-xylylene-4-methyl propiolate)-*co*-*p*-xylylene] (**2**, Figure 2.4). The FTIR spectrum clearly shows C-H stretches at 3265 cm^{-1} and $\text{-C}\equiv\text{C-}$ stretches at 2120 cm^{-1} , which are characteristic of the terminal alkyne groups. The carbonyl C=O stretch at 1718 cm^{-1} and C-O stretch at 1219 cm^{-1} identify the presence of ester bonds. No signs of decomposition or side reactions

were observed. XPS was used to further confirm the chemical composition of the polymer films. From the XPS survey spectrum, the atomic ratios of C1s and O1s were found to be 90.9% (calcd: 90.9%) and 9.1% (calcd: 9.1%), respectively. The calculated values based on the structure of the starting material [2.2]paracyclophane-4-methyl propiolate were consistent with the experimental results shown in Figure 2.4b. This observation confirmed that polymer **2** was successfully synthesized by CVD polymerization.

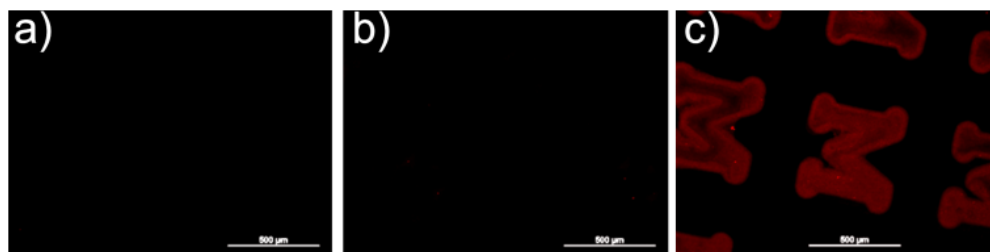


Figure 2.5 Chemical reactivity comparison of polymer **1** and **2** at copper-free condition using μ CP for 3 h at room temperature. CVD polymer coatings on the samples: (a) poly-*p*-xylylene (no reactive functional group, R=H in Figure 2.3); (b) polymer **1** (with inactivated alkyne); (c) polymer **2** (with activated alkyne). After CVD coating, the same treatment was done to samples in all the 3 images: μ CP of biotin-PEG-azide followed by TRITC streptavidin solution incubation. Scale bars represent 500 μ m.

After verification of the chemical composition of polymer **2**, we tested the chemical reactivity of polymer **2** towards azide groups under copper-free conditions and compared it to the previously reported poly[4-ethynyl-*p*-xylylene-*co-p*-xylylene] (**1**);^{8b} reactions were carried out by microcontact printing (μ CP; Figure 2.5). μ CP is a commonly used method to generate micro-scale patterns and has been used in the past to modify functionalized poly(*p*-xylylene)s.^{8b, 31} By using μ CP, high local concentrations of reagents in the contact area can be achieved that can lead to

significantly increased reaction rates.³² Rozkiewics et al. reported printing of acetylene groups onto azide-functionalized self-assembled monolayers without the use of a copper catalyst.^{32a} The microcontact printing approach further enables the selective reaction of defined surface areas embedded in a background of unreacted material; this unreacted material can be used as internal control in subsequent immobilization steps. Herein, a water-based solution of biotin-PEG-azide was used as ink to print onto three different surfaces: polymer **2**, polymer **1**, and unfunctionalized poly(*p*-xylylene). Poly(*p*-xylylene) has the same backbone as coatings **1** and **2**, but does not contain reactive functional groups (R=H in Figure 2.3). This polymer was used as control compound to assess nonspecific adsorption onto the surfaces. Biotin was immobilized on polymer **2** through the triazole linker formed under copper-free conditions in water. Tetramethylrhodamine-5(6)-isothiocyanate (TRITC) conjugated streptavidin was then used to visualize the patterns.³³ In Figure 2.5, fluorescence patterns that are indicative of immobilized TRITC-streptavidin bound to biotin are only observed on polymer **2**, but not on polymer **1** or the unfunctionalized polymer. This result verifies that under copper-free conditions at room temperature, polymer **2** successfully reacted with biotin-PEG-azide, while polymer **1** and poly(*p*-xylylene) showed no reaction.

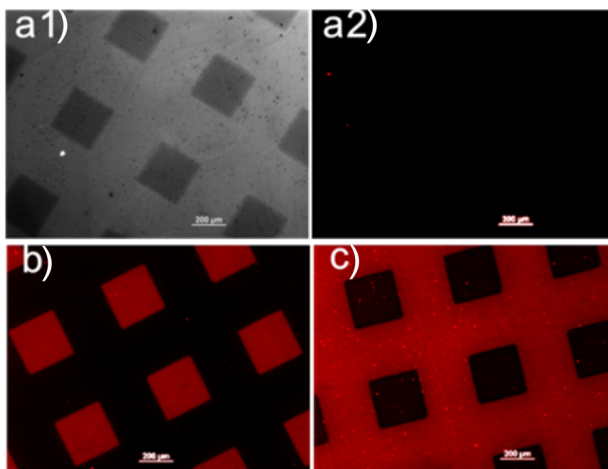


Figure 2.6 Chemical reactivity comparison of polymer **1** and **2** under copper-free conditions in solution reactions at room temperature. Samples coated by a 2-step CVD process using the VAMPIR technique resulted in surfaces with different polymer coatings inside and outside the squares. a1), a2), b) polymer **2** inside the squares and polymer **1** outside as shown in Figure 2.7, c) the reverse pattern, where polymer **1** is inside the squares. a1) bright field image of sample incubated in deionized water and then TRITC-streptavidin, a2) same sample as in (a1) but under red channel. b) and c) samples incubated in biotin-PEG-azide water solution and then TRITC-streptavidin solution. Scale bars represent 200 μm .

We then prepared microengineered surfaces that contained either polymer **1** or polymer **2** in different surface areas (Figure 2.6). We hypothesized that such an approach would enable a head-to-head comparison of the activated versus nonactivated polymer coatings under otherwise identical reaction conditions. This approach was carried out by first coating the entire substrate with one layer of polymer **1** and then depositing a second layer of polymer **2** onto selected surface areas using the previously developed vapor-assisted micropatterning in replica structures (VAMPIR) technique.^{18, 25} The only exception is shown in Figure 2.6c, where the coating sequence was reversed. The difference in thickness between the two polymer layers for all microengineered samples used in this study was measured to be 3–4 nm by imaging ellipsometry. An example of a representative

thickness measurement is shown in Figure 2.9. To ensure that the fluorescence contrast does not stem from possible auto-fluorescence of the polymers, the sample shown in Figure 2.6a1 and a2 was never in contact with any azide compound, but was exposed to deionized water and then TRITC–streptavidin solution only. The microengineered surface did not show any fluorescence signal (Figure 2.6a2), hence confirming that auto-fluorescence of the polymers was negligible and thus would not interfere with the bioconjugation study. The contrast in the bright-field image (Figure 2.6a1) was caused by differences in thickness between the polymer layers and confirmed that the surface was successfully microengineered. Figure 2.6b and c show fluorescence images of two different surfaces that were modified to present inverse polymer patterns, which were achieved by simply reversing the coating sequence. Independent of the sequence of deposition, the results were the same, that is, only polymer **2** reacted with biotin–PEG–azide, while polymer **1** did not reveal any significant fluorescence signal. Note that the reaction time for solution-based reaction was 12 h and thus longer than for the μ CP experiments, which were allowed to proceed for 3 h only. Even under prolonged exposure times, the selectivity was high and biotin–azide molecules were confined to areas that present propiolate groups. We observed that the copper-free reaction for polymer **2** started within seconds, as we could already observe initial contrast in the fluorescence signal after printing for 10 seconds (Figure 2.10).

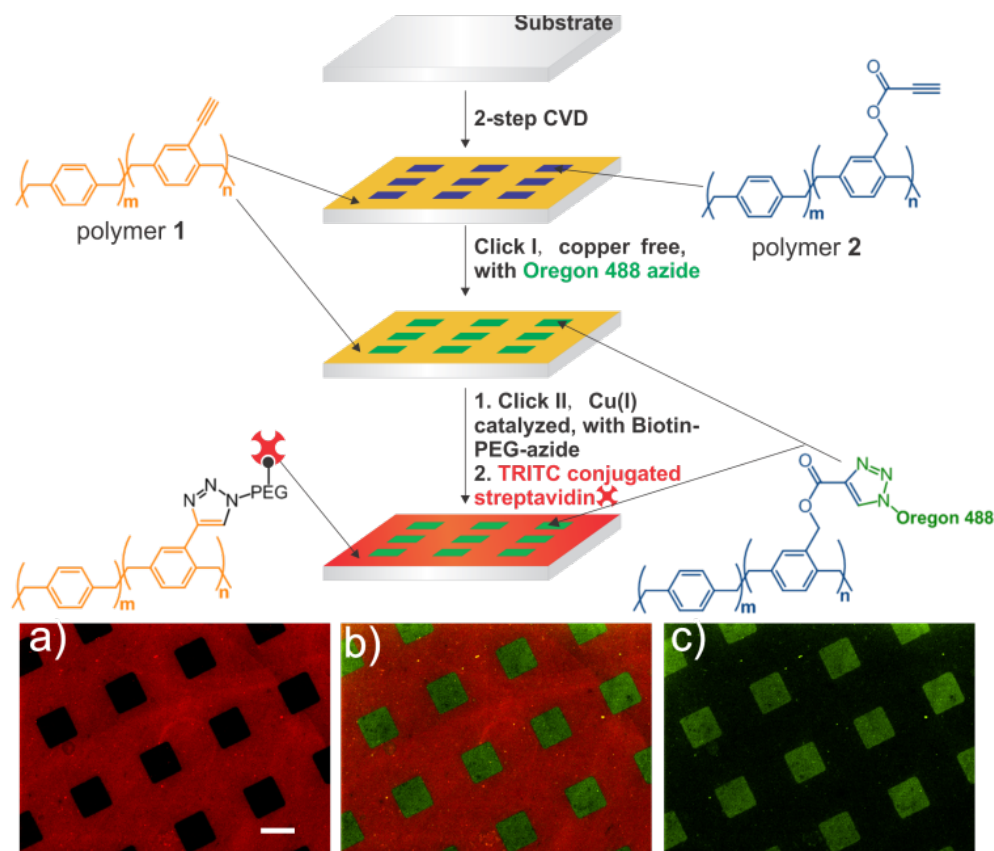


Figure 2.7 Scheme of two-step click reactions on surface coated with different polymers in different selected areas. The goal is to achieve sequential immobilization of molecules on defined areas of the same surface by utilizing the different reactivity of activated and nonactivated alkynyl groups towards azide groups. a), b), c) Fluorescence images of samples prepared exactly as shown in the schematic representation. b) overlay image of green and red channels shown in (a) and (c). Scale bar represents 200 μm .

Finally, we took advantage of the difference in reactivity between polymers **1** and **2** and developed a cascade of bioorthogonal reactions.²⁻³ We devised a 2-step “click” chemistry procedure for sequential immobilization of different molecules on separate areas of the same surface (Figure 2.7). The cascade was put into effect by azide–alkyne reactions on the surface, first without and then with Cu catalyst (only in this order). Using microengineered substrates similar to the ones used above, the

electron-deficient alkyne groups were first reacted inside the squares with Oregon 488 azide in deionized water at room temperature. Under these conditions, the nonactivated alkyne groups that were located in the remaining areas did not react. In a second reaction step, we used CuAAC to immobilize biotin-PEG-azide moieties on the remaining background. Subsequent self-assembly of a TRITC-streptavidin allowed for visualization of the selective surface modification. Figure 2.7b shows the overlay image of green and red channels, clearly with two different molecules immobilized on separate defined areas of the same surface. No cross-reaction of different areas was observed, thus indicating a high degree of selectivity as well as complete conversion during the copper-free reaction of polymer **2** (first reaction step).

2.1.4 Conclusion

A potential limitation of this work is that the copper-free reaction has always to occur first. Reversal of the reaction sequence is not possible in this specific example. However, the newly synthesized CVD coating with activated alkyne groups could also be used in conjunction with other bioorthogonal reactions that have been previously shown to be compatible with CVD coatings.^{31,34} Ultimately, the “double-click” approach proposed herein as well as other bioorthogonal immobilization strategies²⁻³ will likely find applications in areas, in which controlled immobilization of multiple ligands is needed.

Supplemental Figures (Figure 2.8 to 2.10)

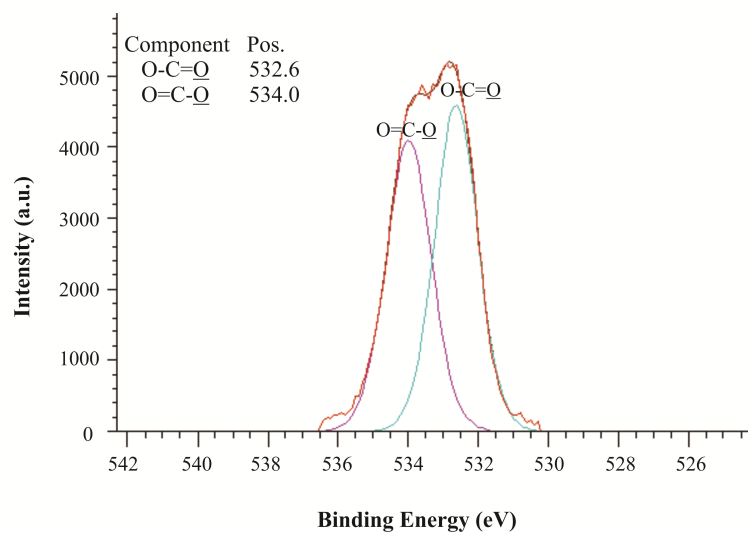
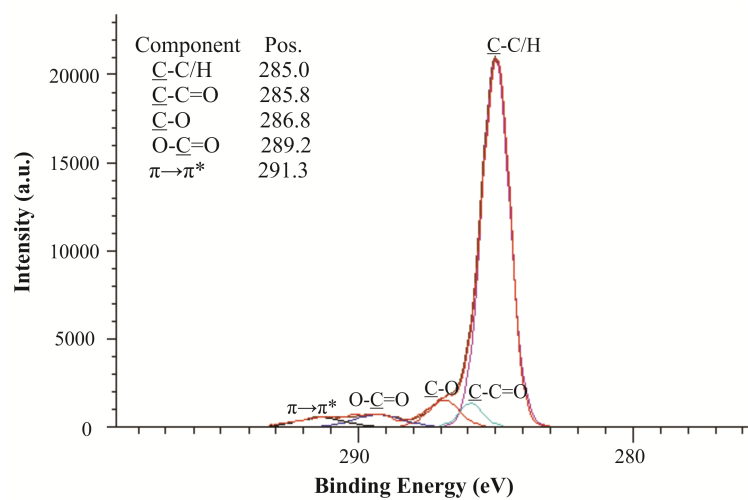
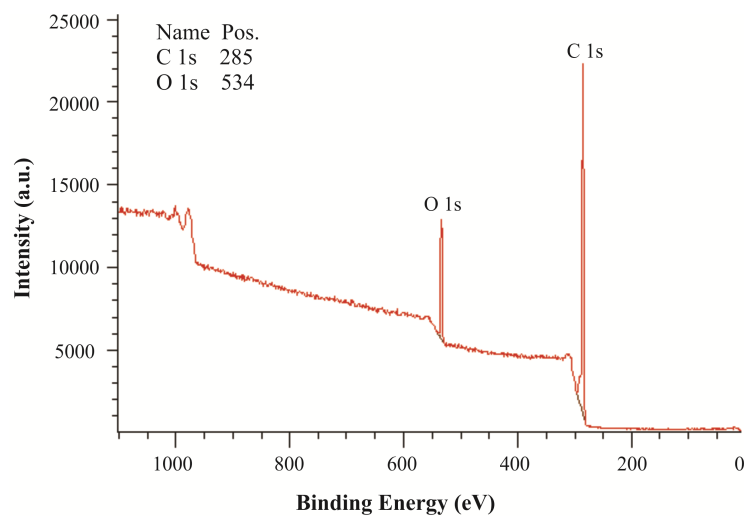


Figure 2.8 XPS survey spectrum and high-resolution peak fittings corresponding to the reported in the table of Figure 1.

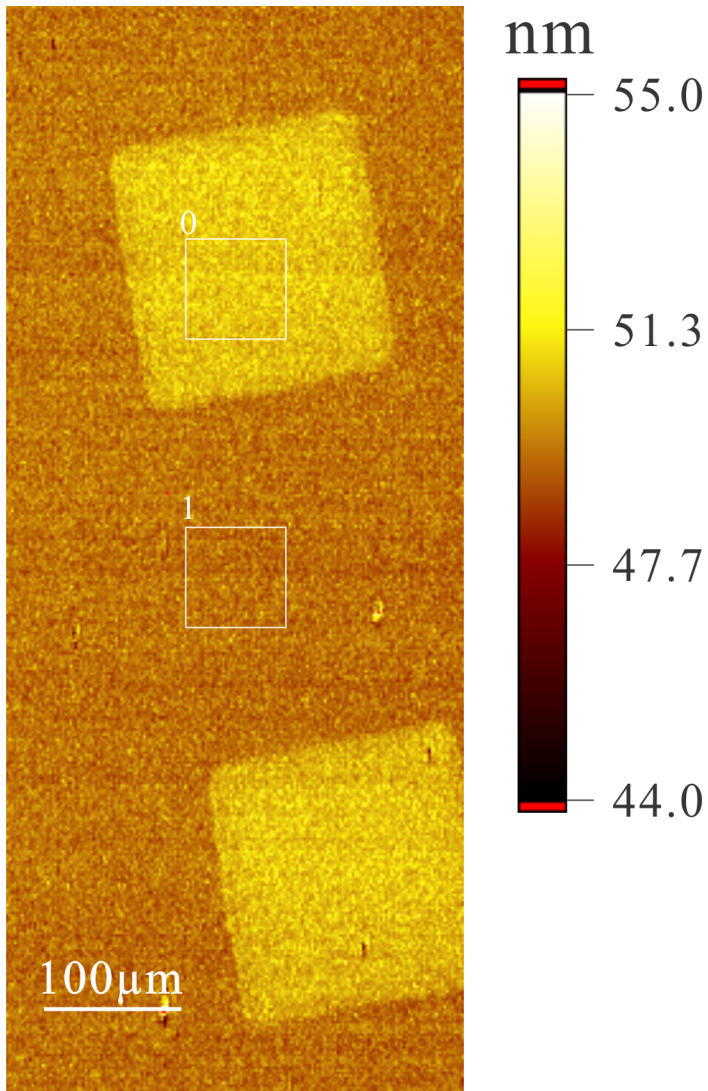


Figure 2.9 Thickness measurement on the micro-engineered surface by Imaging Ellipsometry. The thickness map was generated from delta map at 658nm by modeling. For more accurate measurement, multiwavelength 4-zone nulling was used to measure the average thickness of the region of interest (ROI) 0 and 1 in the image. For this particular sample, thickness for ROI 0 and ROI 1 is 51.2 nm and 48.1 nm respectively.

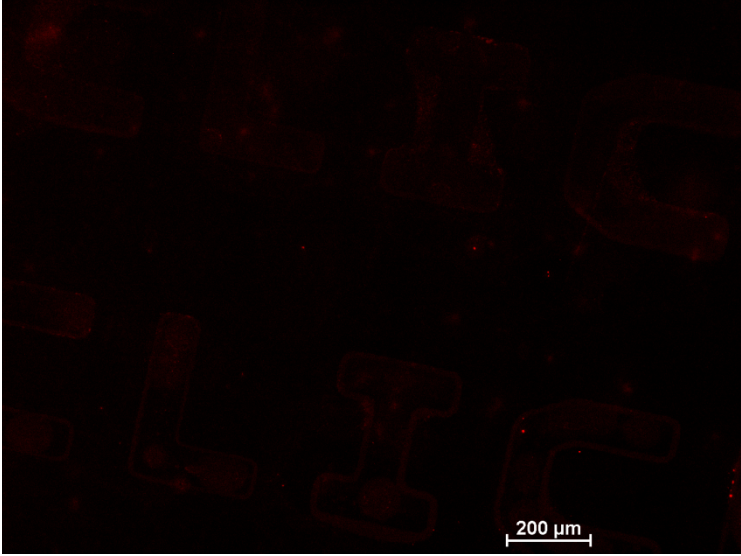


Figure 2.10 Fluorescence image for 10 seconds printing on polymer 2.

2.2 Bio-Orthogonal Polymer Coatings for Co-Presentation of Biomolecules

2.2.1 Introduction

The fate of cells cultured in a synthetic environment is, at least in part, governed by interactions with biomolecules on the substrate surface.¹ The latter act as recognition sites that can induce and mitigate vital cellular functions such as adhesion, migration, and differentiation.^{1b} Potential applications include modification of implants³⁵ such as stents, pacemakers, or grafts; use of polymer substrates for in vitro cell culture;³⁶ or design of bioanalytical tools such as microarrays for protein, DNA, or polysaccharide detection.³⁷ Because of the central role that cell–protein interactions play in biology, advanced applications in medicine and biotechnology require precise presentation of signaling molecules on the substrate surfaces. This revelation fueled a wide range of research activities focused on the controlled presentation of biomolecules on synthetic substrates. Initial work has included physisorption of proteins on substrate surfaces and covalent attachment using a number of nonspecific crosslinking reactions.³⁸ More recent activities have taken advantage of novel immobilization concepts, such as click chemistry, to achieve controlled orientation of biomolecules on surfaces.³⁹ The high specificity of click reactions may potentially provide an additional advantage: the possibility of presenting a combination of multiple biomolecules on the same surface using orthogonal chemical reactions, that is, reactions that do not show cross-reactivity toward their biological target molecules.^{2, 3b}

Previously, we have developed chemical vapor deposition (CVD) polymerization technology to coat a range of functionalized poly-*p*-xylylenes on a variety of substrates.^{9, 15} These reactive coatings provide different functional groups on different coatings that were used for immobilization of biomolecules such as peptides, proteins, and DNA.^{14-15, 35a} Moreover, it has been established that CVD copolymerization of [2.2]paracyclophanes containing different functional groups can be realized. This produces multipotent polymer coatings, which can be used for simultaneous presentation of multiple molecules in controlled ratios.^{3b}

With a number of specific chemical reactions in hand,¹¹ the focus of biomedical engineers is now shifting from model systems to technology platforms that are equally applicable to a wide range of different substrate materials. Copper-catalyzed azide-alkyne 1,3-dipolar cycloaddition is one of the bio-orthogonal reactions, as defined by Sletten and Bertozzi.² The reaction is also known as one of the “click” reactions,⁴ which are characterized by high reaction rate and selectivity. The azide-alkyne 1,3-dipolar cycloaddition has been used in a wide variety of applications, such as bioconjugation, drug design, organic synthesis, and polymer design.⁴⁰ Pentafluorophenyl ester (Pfp-ester) groups are active esters commonly used in peptide synthesis, organic synthesis, polymer chemistry, and surface chemistry.^{31, 41} Pentafluorophenyl ester groups can rapidly react with amines to form amide bond with no side reactions under mild conditions thus suitable for one-step immobilizations of proteins onto surface.^{41c}

Vapor-based coatings provide an attractive solution to major requirements associated with biomolecule immobilization applications, as they can result in

ultrathin, conformal coatings that de facto decouple the surface properties from the underlying bulk material.¹⁰ In this chapter section, we design a multifunctional coating for simultaneous click reaction and active ester chemistry to achieve co-presentation of epidermal growth factor (EGF) and cyclic arginine-glycine-aspartic acid (cRDG) adhesion peptides. Cell responses on the surface immobilized with two different biomolecules were then tested. (Scheme shown in Figure 2.13a) Our approach builds on recent progress with CVD co-polymerization, to develop multifunctional coatings that (1) can present two different biomolecules, that is, cyclic RGD peptide (cRGD) and epidermal growth factor (EGF); (2) offer orthogonal immobilization pathways; and (3) are applicable to a wide range of different substrate materials.

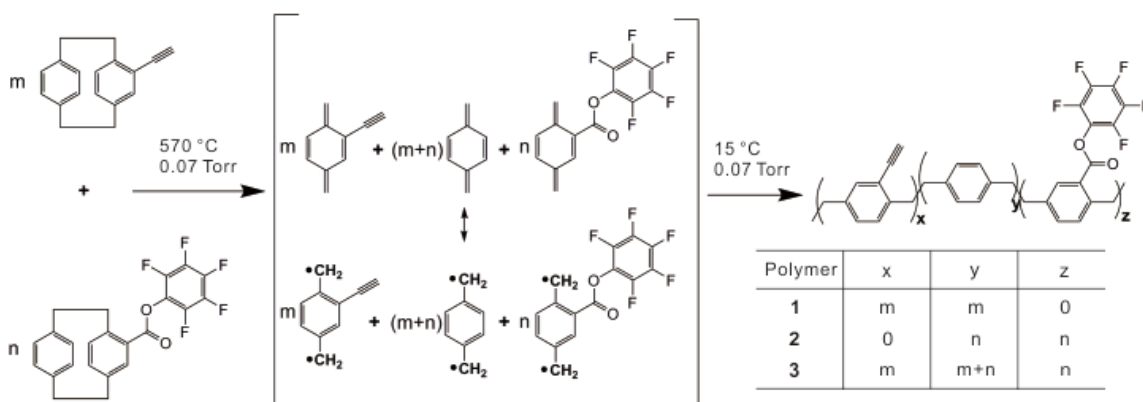


Figure 2.11 CVD copolymerization of [2.2]paracyclophanes with pentafluorophenyl ester and alkyne groups; $m = n$ for the copolymer **3** discussed in this chapter section.

2.2.2 Experimental Section

All materials were purchased from Sigma–Aldrich and used without further purification unless otherwise indicated.

CVD Co-Polymerization

The synthesis of the two precursors used in this study, 4-pentafluorophenyl ester[2.2]paracyclophane and 4-ethynyl[2.2] paracyclophane was described elsewhere.^{8b, 15} CVD co-polymerization was performed using 1:1 molar mixtures of the two precursors as shown in Figure 2.11 . The precursors sublimated under 0.07 Torr at temperatures above 100 °C and were transferred in a stream of argon carrier gas (20 sccm) to the pyrolysis zone (560 °C). Following pyrolysis, the diradicals were transferred into the deposition chamber, with the chamber wall temperature adjusted to 120 °C and substrates cooled to 15 °C to optimize the deposition. Moreover, rotation of the substrates ensured uniform film thickness.

Surface Characterization

IR spectroscopy was performed on a Nicolet 6700 spectrometer with the MCT-A detector and the grazing angle accessory (Smart SAGA) at a grazing angle of 80°. The coatings for IR characterization were all controlled at 50–60 nm. XPS data were recorded on an Axis Ultra X-ray photoelectron spectrometer (Kratos Analyticals, UK) equipped with a monochromatized AlK α X-ray source (takeoff angle 90 °). All spectra were calibrated with respect to the non-functionalized aliphatic carbon with a binding energy of 285.0 eV. Thicknesses were measured by Imaging Spectroscopic Ellipsometer (Accurion, Nanofi lm EP³ -SE). Ellipsometric

parameters were fitted using Cauchy model. The imaging lateral resolution is $\approx 2 \mu\text{m}$ for the $10 \times$ objective.

Immobilization of EGF

The procedure of immobilization of epidermal growth factor (EGF) and adhesion peptide is shown in Figure 2.13a. Microcontact printing (μCP) was used in this study to confirm each immobilization step. PDMS stamps were created as described elsewhere.²⁵ Stamps were oxidized for 20 min using UV-ozone cleaner before use. The stamps inked with EGF solution ($10 \mu\text{g mL}^{-1}$ in PBS) were kept in contact with the sample surface for 10 min. After stamp removal, the patterned samples were thoroughly washed with PBS. The immobilization reactions in solution without using μCP were the same as described above. The substrates immobilized with EGF were incubated with an anti-EGF antibody (a mouse IgG antibody) diluted in PBS containing 0.1% (w/v) bovine albumin and Tween 20 (0.02% (v/v)) ($10 \mu\text{g mL}^{-1}$) for 1 h. After washing with the PBS/BSA/Tween buffer, the samples were incubated in the PBS/BSA/Tween buffer containing FITC conjugated antimouse IgG ($10 \mu\text{g mL}^{-1}$) for 1 h. The stained samples were then washed with PBS, rinsed with distilled water, and observed under a fluorescence microscope (Olympus BX-51, Japan).

Immobilization of the cRGD Peptide

cRGD peptide with an azide end group (cyclo(azidoK-RGDf), Kinexus, Canada) was dissolved in an aqueous solution of sodium ascorbate (50 mg mL^{-1}) and copper(II) sulfate ($0.1 \times 10^{-3} \text{ M}$). The peptide concentration was $50 \mu\text{g mL}^{-1}$. The stamp inked with the peptide azide solution was then kept in contact with the

sample surface for 4 h, followed by stamp removal and repeated washing with PBS and deionized water. The condition was the same for reaction in solution without using μ CP.

Adhesion and Spreading of Endothelial Cells

Copolymer **3** was deposited via CVD onto silicon and modified as outlined above to present tethered EGF, cRGD, EGF+cRGD, or passivated with 2-(2-aminoethoxy)ethanol (AEE). Once modified, these surfaces were washed thoroughly and placed in a 24-well plate. Human umbilical vein endothelial cells (HUVEC, Lonza) were cultured on the modified surfaces at a concentration of 5×10^4 cells/ml for 4 hours in serum-free EBM (Lonza). Passages 3-6 were used for all experiments. The cells were then fixed with 4% paraformaldehyde in DPBS and stained for actin with Alexa Fluor[®] 568-phalloidin (Invitrogen). The surfaces were mounted with ProLong Gold + DAPI (Invitrogen) and imaged using an Olympus BX-51 fluorescence microscope. The average area of the cells was measured via ImageJ, and performed by dividing total cell area by total number of cells (equated to total number of individually counted DAPI stains). The results show three independent trials averaged; error bars are standard error (standard deviation divided by the square root of the total number of images taken over three trials), and p-values are calculated using all images from all trials.

Phosphorylated EGFR Immunofluorescence

The epidermal carcinoma line A431 (ATCC, Manassas, VA) was cultured in polystyrene flasks (Corning, Lowell, MA) at 37 °C and in a humidified 5% CO₂

atmosphere until 100% cell confluence were observed. Passage 3 was used for all experiments. 18 hours prior to incubation with the modified surfaces, the A431 culture was serum-starved. A431 cells were trypsinized, spun down at 100xg, and resuspended with serum-free DMEM (ATCC) to a cell concentration of 5×10^4 cells/ml. A volume of 0.5 ml of A431 suspension was added to each well containing a surface. After 90 minutes of incubation at 37 °C/5% CO₂, the cells were briefly washed with PBS, then fixed with 4% paraformaldehyde. After three five-minute PBS washes, the surfaces were incubated with blocking buffer (5% normal goat serum (Invitrogen, Carlsbad, CA), 0.3% Triton-X 100 (Sigma-Aldrich) in PBS) for one hour followed by overnight incubation with primary antibody Phospho-EGF Receptor (Tyr1068) (D7A5) XP™ Rabbit mAb (Cell Signaling Technology, Danvers, MA). Incubation with secondary antibody Anti-rabbit IgG (H+L), F(ab')₂ Fragment (Alexa Fluor® 488 Conjugate) for two hours followed; finally the surfaces were cured on glass slides with ProLong Gold + DAPI (Invitrogen) and imaged using an Olympus BX-51 fluorescence microscope. The quantity of immunofluorescence as a ratio of total grey pixelation to cell area minus threshold was measured via ImageJ. The results show three independent trials averaged; error bars are standard error (standard deviation divided by the square root of the total number of images taken over three trials), and p-values are calculated using all images from all trials.

EGF EC₅₀ Measurement

A431 cells were cultured as previously described, and starved for 18 hours prior to incubation. Cells were trypsonized and cultured on AEE-modified surfaces, then incubated with a range of soluble EGF concentrations from 0.1 to 1000 ng/ml

for 1 hour. pEGFR was then measured via the immunofluorescence protocol described above, including the same primary and secondary antibodies. EC₅₀ data was fitted and analyzed using GraphPad Prism version 5.01 for Windows (GraphPad Software, San Diego California USA) using the modified variable slope model.

Image and Statistical Analysis

The software package ImageJ (NIH) was used to analyze all images. Normalized cell spreading was quantified by measuring the total cell area and dividing by the total number of cells (counted by DAPI spot). Magnitude of fluorescence quantification was performed by converting the images to a 32-bit gray scale and then measuring the mean gray value. All error bars with the exception of the EC₅₀ graph (which show standard deviation) represent standard error (one standard deviation from the mean divided by the square root of the total number of images averaged). Statistical significance was determined using Students two-tailed T-test assuming unequal variance, with $p < 0.001$ considered significant.

2.2.3 Results and Discussion

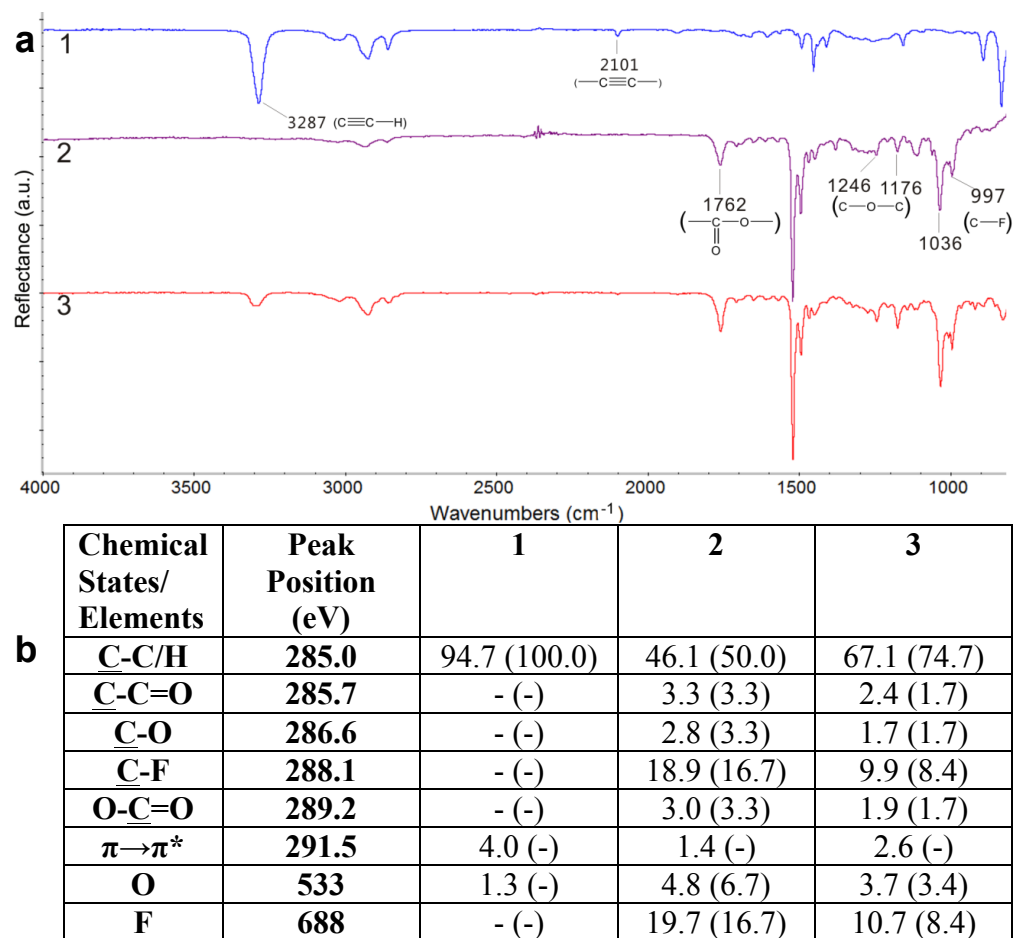


Figure 2.12 a): FTIR spectra for polymer **1**, **2** and **3** and **b):** chemical composition in atom-% shown as experimental value (calculated value in the bracket) determined by XPS; Experimental values of O and F atom ratios [%] were from survey results and other experimental values are from high resolution C 1s spectra peak fitting calculated based on a equimolar distribution of starting materials.

To achieve controlled immobilization of multiple biomolecules, we first had to develop a polymer coating with multiple functional groups, which can covalently bind to different molecules using orthogonal reaction pathways. The copolymer to be developed in this study is poly[(4-ethynyl-*p*-xylylene)-*co*-(4-pentafluorophenyl ester-*p*-xylylene)-*co*-(*p*-xylylene)] (**3**). Poly[(4-ethynyl-*p*-xylylene)-*co*-(*p*-xylylene)] (**1**) and poly[(4-pentafluorophenyl ester-*p*-xylylene)-*co*-(*p*-xylylene)] (**2**), which

only have one of the two functional groups (either alkyne or pentafluorophenyl ester), are shown in Figure 2.11 and Figure 2.12 for comparison. The Fourier transform infrared (FTIR) spectrum of copolymer **3** shown in Figure 2.12 reveals characteristic bands of alkyne groups (3287 and 2101 cm^{-1}) and pentafluorophenyl ester groups (1762 , 1523 , and $1250\text{--}990\text{ cm}^{-1}$). In addition, no sign of crossreactions between functional groups were observed during CVD polymerization. Next, the polymer films were analyzed by X-ray photoelectron spectroscopy (XPS), which has routinely been used to confirm the chemical composition of the outermost 10 nm of polymer films. The experimental values shown in Figure 2.12 are in good agreement with the calculated surface composition, which was obtained according to the chemical formula of the starting materials assuming stoichiometric conversion into the polymer. Detailed XPS analysis revealed concentrations of **F** and **C—F** in the copolymer **3** to be approximately half of polymer **2**, which only carries pentafluorophenyl ester groups on the surface. It shows that by feeding 1:1 molar ratio of the different precursors, approximately 1:1 ratio of each functional group was observed on the surface.

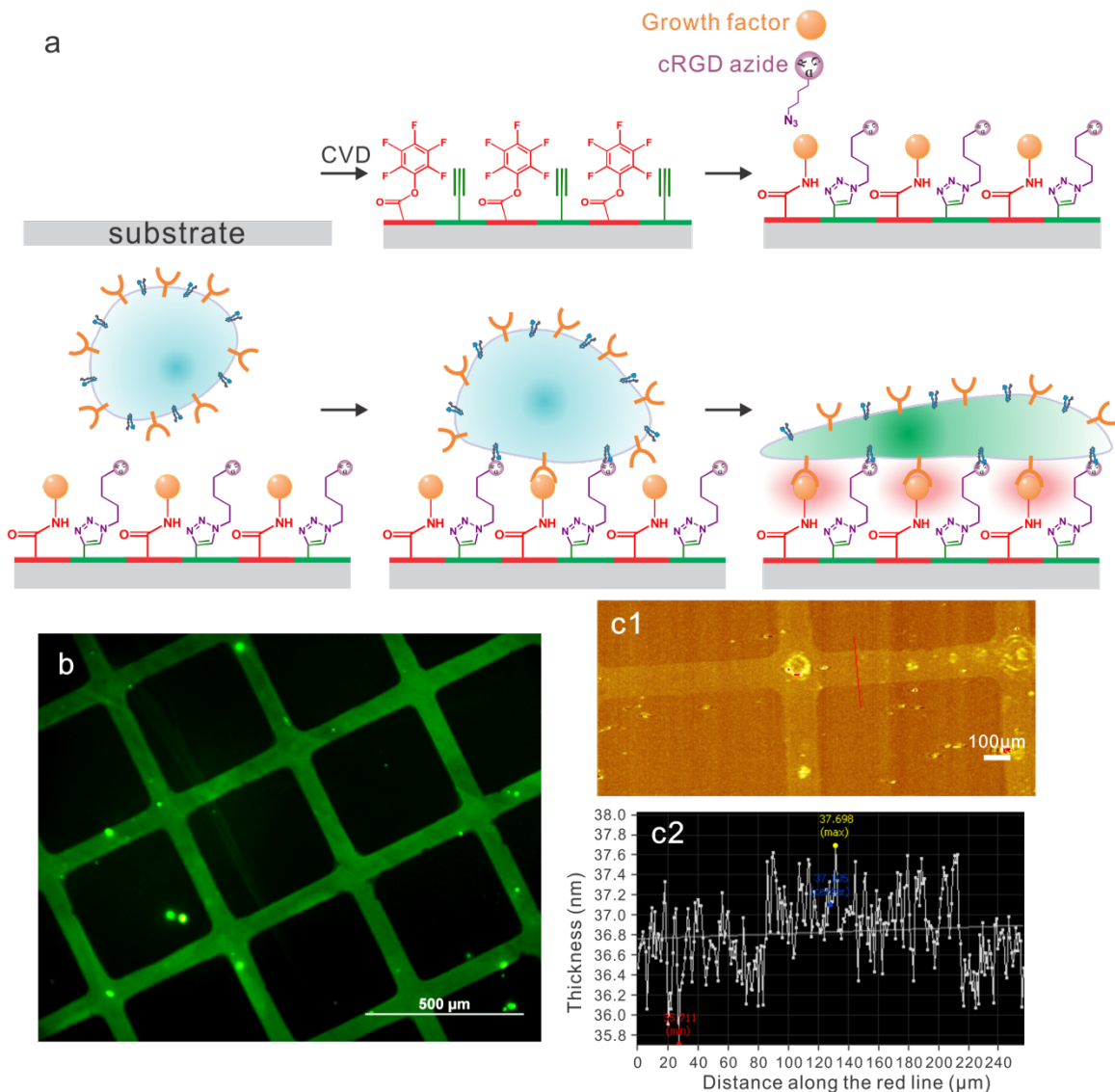


Figure 2.13 a): Scheme for CVD copolymerization, biomolecules immobilization and potential cell responses. b) Fluorescence micrograph of epidermal growth factor (EGF) immobilized in patterned area after μ CP and immunostaining. c1) Imaging ellipsometry thickness map of cRGD peptide pattern. c2) Thickness profile representing thickness difference along the red line shown in (c1).

To confirm that the simultaneous surface conjugation of both the peptide and growth factor was feasible, microcontact printing was used to create patterned substrates of protein or peptide. Areas not modified during microcontact printing were used as an internal reference. The cRGD peptide was immobilized using click

chemistry (i.e., Huisgen's [1,3]dipolar cycloaddition catalyzed by Cu^+ ions), and EGF was tethered covalently by reaction with the highly reactive Pfp-ester group to form an amide bond with the terminal primary amine. Immunostaining was used to visualize the immobilized EGF. The polymer 3 coated substrates functionalized with EGF at the patterned area were incubated in anti-EGF antibody (primary antibody) solution, washed and then immersed in the solution of FITC conjugated antimouse IgG (secondary antibody). Figure 2.13b shows that after immunostaining of the entire surface, only the area with EGF showed fluorescence. This suggests that the active ester chemistry for growth factor immobilization (Figure 2.13a) was successful. The cRGD peptide immobilization was characterized by imaging ellipsometry. Figure 2.13c1 and c2 show that the thickness of the area patterned with cRGD peptide via click chemistry was approximately 0.5 nm higher than the unpatterned area, which confirmed that the cRGD peptide was immobilized on the surface of polymer 3.

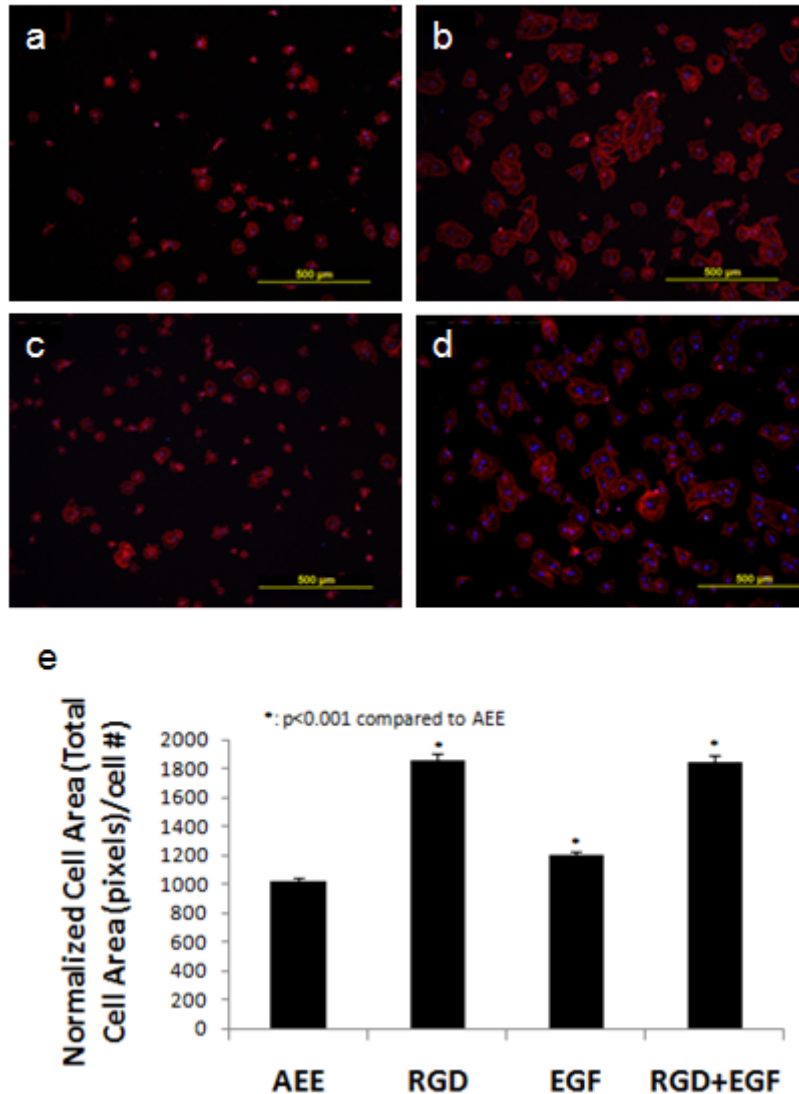


Figure 2.14 Fluorescence micrographs of HUVEC line seeded onto modified surfaces of polymer 3 after 4 h incubation. The surfaces were tethered with: (a) AEE (b) cRGD-only (c) EGF-only (d) cRGD + EGF (e) Quantification of spreading by ImageJ (three trials combined).

We then evaluated the immobilization of cRGD via click reaction and assessed peptide activity in the presence of immobilized growth factor. The RGD tripeptide is a well-studied cell adhesion motif present in many proteins, but perhaps most prominently in extracellular matrix (ECM) molecules, such as fibronectin and vitronectin (among others).⁴² RGD (and other small peptide

adhesion molecules) have been widely explored for use in tissue engineering and presents several advantages over full-length proteins such as fibronectin, including issues such as enzymatic denaturation and overall molecular size.⁴³ The cRGD peptide was employed in this study. The major advantages of these cyclic peptides are automatable synthesis, resistance against proteolysis, weak immunogenicity, high specificity to integrin $\alpha_v\beta_3$, and enhanced biological activity (up to 240 times of linear analogues).⁴⁴ Human umbilical vein endothelial cells (HUVEC) spreading on polymer **3** surfaces with different treatments was shown in Figure 2.14. The surfaces were passivated with 2-(2-aminoethoxy)ethanol (AEE),³¹ immobilized only with cRGD, only with EGF or with both biomolecules, respectively. HUVEC spreading is significantly enhanced by the presence of cRGD. The cell area on the surface with both cRGD and EGF was approximately the same as the one with only cRGD. The surface immobilized only with EGF only had a slight increase in cell area. The observance that EGF did not have any obvious effect on HUVECs is consistent with other studies showing the absence of EGFR expression in normal HUVECs.⁴⁵

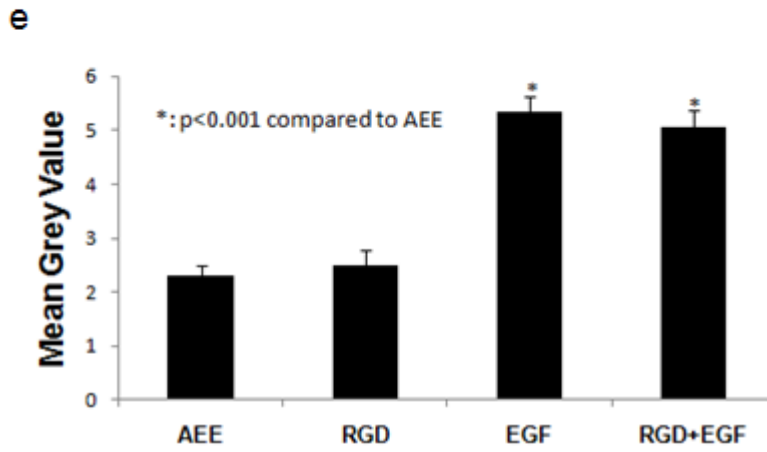
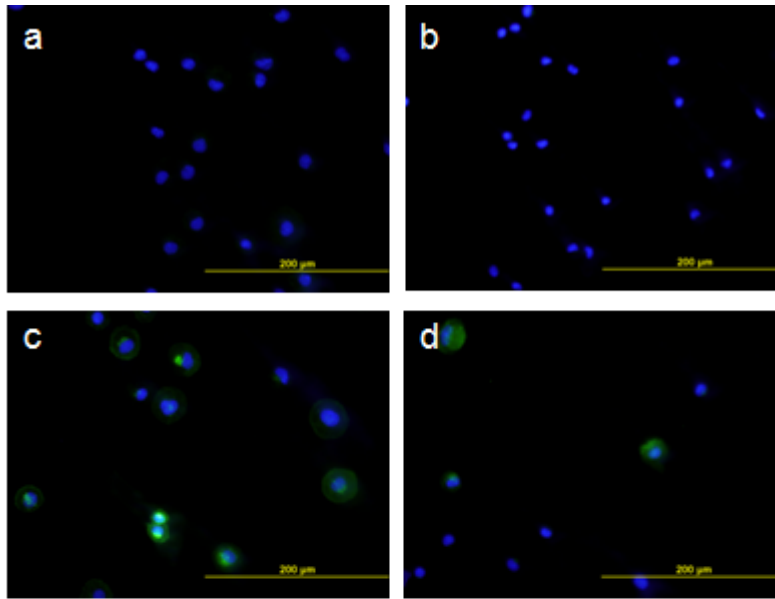


Figure 2.15 Immunofluorescence of phosphorylated EGFR in A431 cells cultured on CVD-coated surfaces with tethered (a) AEE (b) cRGD (c) EGF and (d) cRGD+EGF. (e) Quantification of pEGFR immunofluorescence (three trials combined).

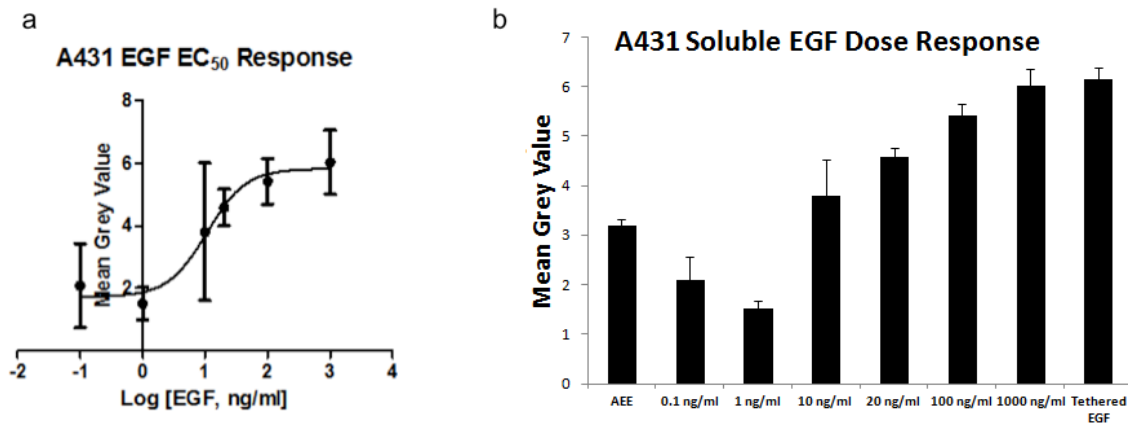


Figure 2.16 a) EC₅₀ plot for EGF (individual trial); b) Quantification of pEGFR immunofluorescence of phosphorylated EGFR in A431 cells in bar graph form (individual trial). The cells were cultured on CVD-coated surfaces passivated with AEE and in media with soluble EGF from 0-1000 ng/ml, in comparison with surface with tethered EGF in soluble EGF-free media.

Tethering growth factors has gained more interest from the scientific community within the last three decades.⁴⁶ Studies showed that the immobilized growth factors, compared to the soluble ones, had higher mitogenic effect, longer-term signal transduction and were resistant to endocytosis, degradation and diffusion.⁴⁷ In order to verify that the immobilized EGF still has biological activity, we investigated our modified surfaces' ability to induce phosphorylation of EGFR (pEGFR), the receptor of EGF. The A431 line is a human epidermal carcinoma and a well-characterized positive control for EGFR activity.⁴⁸ A431 cells overexpress EGFR roughly 10–50-fold over many other cell lines, and thus are an ideal cell type for examining the bioactivity of tethered EGF.⁴⁹ Surfaces with tethered EGF successfully induce phosphorylation of EGFR in serum-starved A431 cells, as observed using immunofluorescence (Figure 2.15). This shows that the immobilized EGF on polymer 3 maintained its biological activity. Surfaces exhibiting both the adhesion

factor cRGD and EGF show statistically similar ($p < 0.001$) pEGFR phosphorylation compared to those exhibiting EGF alone, demonstrating that multiple biofactors do not affect this particular growth factor's ability to interact with its receptor. We next examined A431 EGFR phosphorylation in response to soluble EGF and compared it to tethered EGF (Figure 2.16). Various literature indicate that A431 respond to EGF with EC_{50} values of 12.1 ng mL^{-1} and 20 ng mL^{-1} , respectively.⁵⁰ From four independent trials, an average EC_{50} value was $14.8 \text{ ng mL}^{-1} \pm 3.02 \text{ ng mL}^{-1}$ (standard error), well matching the reported literature values previously cited. In all four trials, EGFR phosphorylation of tethered EGF as measured by quantification of immunofluorescence was either statistically equivalent to or higher ($p < 0.05$) than the highest concentration of soluble EGF tested (1000 ng mL^{-1}), demonstrating the potency of tethered EGF.

2.2.4 Conclusion

The herein developed immobilization scheme has been successfully developed to immobilize a peptide and a growth factor. In independent experiments, we have further been able to demonstrate biological activity of the respective factor in the presence of the second biomolecules. Future work include validating this technique for other growth factors and chemokines, tethering patterns of different factors to induce topology-specific differentiation of human mesenchymal stem cells, and using two-source CVD to create precise gradients of factors for induction of differential morphogenesis in various epithelial lines.

2.3 A Generic Strategy for Co-Presentation of Heparin-Binding Growth Factors Based on CVD Polymerization

2.3.1 Introduction

Precise surface engineering is one of the major challenges in biotechnology.¹ While it is widely recognized that the fate of cells cultured in vitro is determined by their local microenvironment consisting of both soluble and solid components, many biological studies focus mainly on the role of soluble factors, which can be controlled by simple methods.⁵¹ However, the defined presentation of biomolecules on the cell culture substrates can contribute in equal ways to a specific cellular response.^{1, 47b} For example, extracellular matrix proteins, such as fibronectin, laminin, or collagen, are routinely attached to cell culture dishes to facilitate cell adhesion.⁵² While there exists a multitude of immobilization methods for single biomolecules,⁵³ these approaches typically do not account for the multivalency of biological interactions. Controlled co-immobilization of multiple biomolecules is an essential requisite for certain biomedical applications, such as in vitro cell culture or biosensors.^{36b, 54} If proteins are immobilized through simple physisorption, the outcomes are governed by complex adsorption/desorption equilibria.¹ If multiple proteins are presented on a surface, the physisorption dynamics are governed by the Vroman effect leading to a continuous exchange of proteins until coverage with the largest protein is obtained.⁵⁵ Thus, physisorption methods are unable to precisely engineer stable protein compositions on a surface. Alternatively, chemical immobilization can be employed. Simultaneous presentation of multiple

biomolecules to a substrate with a single surface chemistry (e.g., via active esters) has been previously reported.^{36b, 54a} However, this method is still not precise, as the cross-reactivity of the biomolecules may be associated with a range of different complications. For example, the solution composition of the biomolecules is not necessarily the final composition encountered on the surface after immobilization.

A more appropriate approach is the use of orthogonal immobilization strategies, where a substrate presents multiple types of functional groups without cross-reactivity.^{23, 27a, 56} Recently, we have established an orthogonal co-immobilization method for the cyclic RGD (cRGD) adhesion peptide and the epidermal growth factor (EGF), which uses chemical vapor deposition (CVD) copolymerization of two different functionalized [2.2]paracyclophanes yielding a polymer surface that presented acetylene and pentafluorophenyl ester groups in an equimolar ratio.²³ In this case, coupling of the peptide was achieved via copper-catalyzed heterocycloaddition and the growth factor was linked through primary amino groups via pentafluorophenyl ester groups. In our previous studies, we found that the choice of pentafluorophenyl ester groups is lacking specificity towards the growth factor because of the abundance of amino groups in biomolecules. We also found that the immobilization of proteins through potentially vital amino acids can potentially reduce their bioactivity.⁵⁷ Whether or not the direct immobilization via primary amino groups is applicable will thus need to be validated on a case-by-case basis for each different growth factor. In addition, the direct immobilization approach does not reflect the fact that growth factors immobilized on abiotic

surfaces can easily undergo denaturation and that the use of appropriate linkers may effectively stabilize the immobilized growth factors.

In this chapter section, we develop a generic immobilization approach for heparin-binding growth factors, which includes numerous commonly used growth factors, such as fibroblast growth factors (FGFs), vascular endothelial growth factor, heparin-binding EGF-like growth factor (HBEGF), platelet-derived growth factor, or hepatocyte growth factor (HGF). As an example, we selected the basic fibroblast growth factor (bFGF) as a model of a heparin-binding growth factor. However, we note that the herein developed procedure is equally applicable to other heparin-binding growth factors. It has been previously reported that binding to heparin protects FGF from denaturation at variant pH, at high temperatures, and proteolysis.⁵⁸ Moreover, binding either to heparin or heparan sulfate is a prerequisite for the binding of FGF to its high-affinity receptor on the cell surface.⁵⁹ Considering the importance of heparin for protecting bFGF and enhancing its bioactivity, we designed a method to first immobilize heparin on the surface and then tether the growth factor through the heparin-binding domain and charge interactions.⁶⁰ We further demonstrate the compatibility of this approach with the co-immobilization of an additional biological moiety via the well-established and widely employed copper-catalyzed heterocycladdition.^{8b, 23} However, the CVD coatings may carry a wide range of different functional groups including anhydrides, active esters, aldehydes, ketones, amines, alkyne, as well as photo-reactive benzoyl groups.¹¹

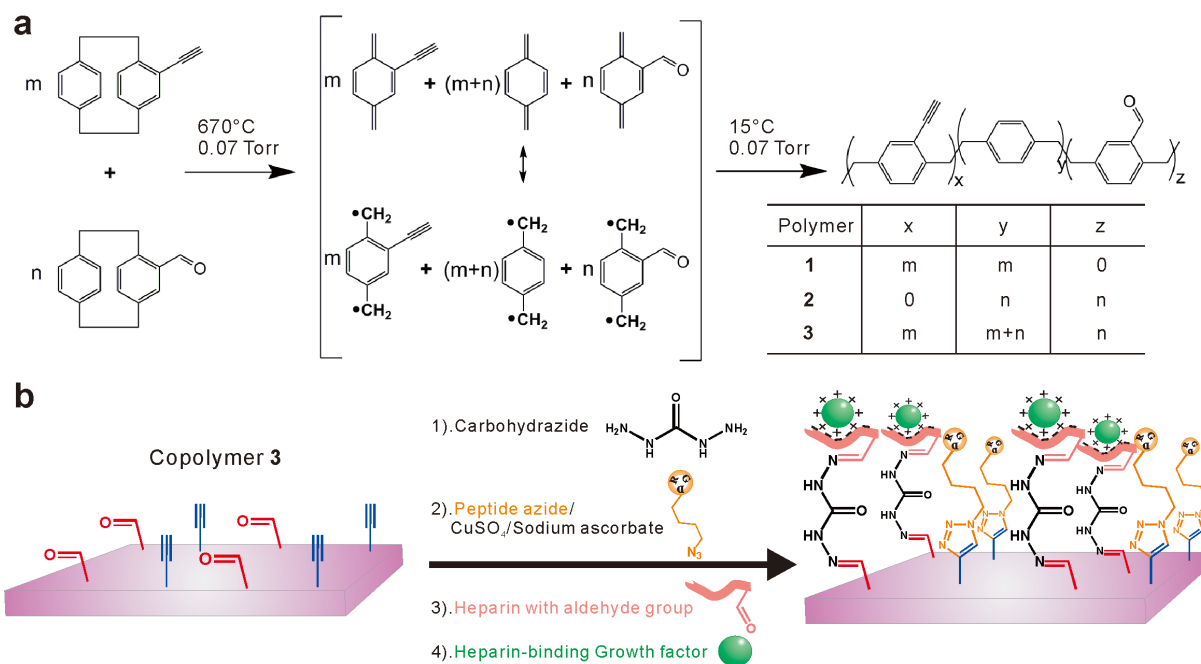


Figure 2.17 a) CVD copolymerization of [2.2]paracyclophanes with aldehyde and alkyne groups. $m = n$ for the copolymer **3** discussed in this chapter section. Polymer **1** and **2** are used as controls. b) Co-immobilization scheme for heparin-binding growth factor and adhesion peptide on the copolymer **3**.

2.3.2 Experimental Section

All materials were purchased from Sigma–Aldrich and used without further purification unless otherwise indicated.

CVD Co-Polymerization

The synthesis of the two CVD precursors used in this study, 4-formyl[2.2]paracyclophane and 4-ethynyl[2.2]paracyclophane was described elsewhere.^{8b, 34a} As shown in Figure 2.17a, CVD co-polymerization was performed using 1:1 molar mixtures of the two precursors. The precursors sublimated under 0.07 Torr at temperatures above 100 °C and were transferred in a stream of argon carrier gas (20 sccm) to the pyrolysis zone (670 °C). Following pyrolysis, the diradicals were transferred into the deposition chamber, with the chamber wall

temperature set at 120 °C and rotating sample holder cooled to 15 °C to optimize the deposition. The coatings were controlled at 80–100 nm.

Surface Characterization

FTIR analysis of the coatings was carried out on a Nicolet 6700 spectrometer with the MCT-A detector and the grazing angle accessory (Smart SAGA) at a grazing angle of 80 °. XPS was performed on an axis ultra X-ray photoelectron spectrometer (Kratos Analyticals, UK) equipped with a monochromatized Al-K α X-ray source. All spectra were calibrated with respect to the non-functionalized aliphatic carbon with a binding energy of 285.0 eV. An imaging spectroscopic ellipsometer (Accurion, Nanofilm EP³-SE, Germany) was used to measure film thickness. Ellipsometric parameters were fitted using a Cauchy model.⁶¹ The imaging lateral resolution is ≈ 2 μm for the 10 \times objective. Time-of-flight secondary ion mass spectrometry (TOF-SIMS) was performed on a PHI TRIFTV nanoTOF instrument (Physical Electronics, USA). The analysis conditions are the following: primary ion 30 kV Au⁺, DC current 2.5 nA, mass range 0–1850 m/z , analysis area 400 $\mu\text{m} \times 400 \mu\text{m}$ (256 \times 256 pixels), charge compensation 15 eV e⁻, post acceleration 5 kV, acquisition time 10 min ($< 1 \times 10^{11}$ ions cm^{-2}) per data set. Data was collected in both ion polarities in an automated fashion using AutoTool. The diagnostic mass peaks were observed < 300 m/z .

Immobilization of Biomolecules

The details and sequence for co-immobilization of the adhesion peptide and the heparin-binding growth factor are shown in Figure 2.17b. Microcontact printing (μCP) with PDMS stamps (preparation process reported elsewhere^{8b}) was used for

elucidating the surface chemistries and creating internal reference areas that can be directly observed by microscopy. The method for adhesion peptide immobilization followed a literature-known procedure.²³ Briefly, cRGD peptide with an azide end group [cyclo(azidoK-RGDf), Kinexus, Canada] was dissolved in an aqueous solution of sodium ascorbate (50 mg mL^{-1}) and copper(II) sulfate ($0.1 \times 10^{-3} \text{ M}$). The peptide solution ($50 \text{ } \mu\text{g mL}^{-1}$) was in contact with the CVD copolymer coating (polymer 3) for 4 h followed by thorough washing. For the heparin immobilization, the periodated heparin (Celsus Laboratories, Inc.) with aldehyde functional groups was used. A bivalent carbonylhydrazide linker was used to link the aldehyde groups on the polymer surface and heparin. The PDMS stamps inked with carbonylhydrazide solution ($10 \text{ } \mu\text{g mL}^{-1}$) were kept in contact with the coating surface for 20 min. After stamp removal, the patterned samples were thoroughly washed with distilled water and incubated in the periodated heparin solution (10 mg mL^{-1} , pH 5) overnight. To confirm the success of the heparin immobilization, immunostaining was performed with the heparin antibody (anti-heparin/Heparan Sulfate, clone T320.11, Isotype: mouse IgG1, Millipore) and the Alexa Fluor[®] 555 antimouse IgG1 (Life Technologies Corporation). More specifically, the surface was incubated in a heparin antibody solution ($5 \text{ } \mu\text{g mL}^{-1}$ solution in PBS with 0.1% (w/v) bovine albumin (BSA) and 0.02% (v/v) Tween 20 for 1 h. After washing thoroughly, the surface was incubated in a PBS/BSA/Tween buffer containing Alexa Fluor[®] 555 anti-mouse IgG1 ($10 \text{ } \mu\text{g mL}^{-1}$) for 1 h. The stained samples were then washed with PBS, rinsed with distilled water, and visualized using fluorescence microscopy (Olympus BX-51, Japan). For immobilization of the human bFGF (Sigma–Aldrich) on

heparin, a heparin-presenting surface (without antibody) was incubated in the PBS/BSA/Tween buffer containing bFGF ($5 \mu\text{g mL}^{-1}$) for 1 h and washed thoroughly. To confirm the success of the bFGF immobilization, immunostaining was performed, as described for heparin. The only difference was that instead of using heparin antibody, we used an anti-human bFGF (Isotype: mouse IgG1, BioLegend) as the primary antibody. Other conditions (buffer, concentration, incubation time, secondary antibody, and washing procedure) were identical.

2.3.3 Results and Discussion

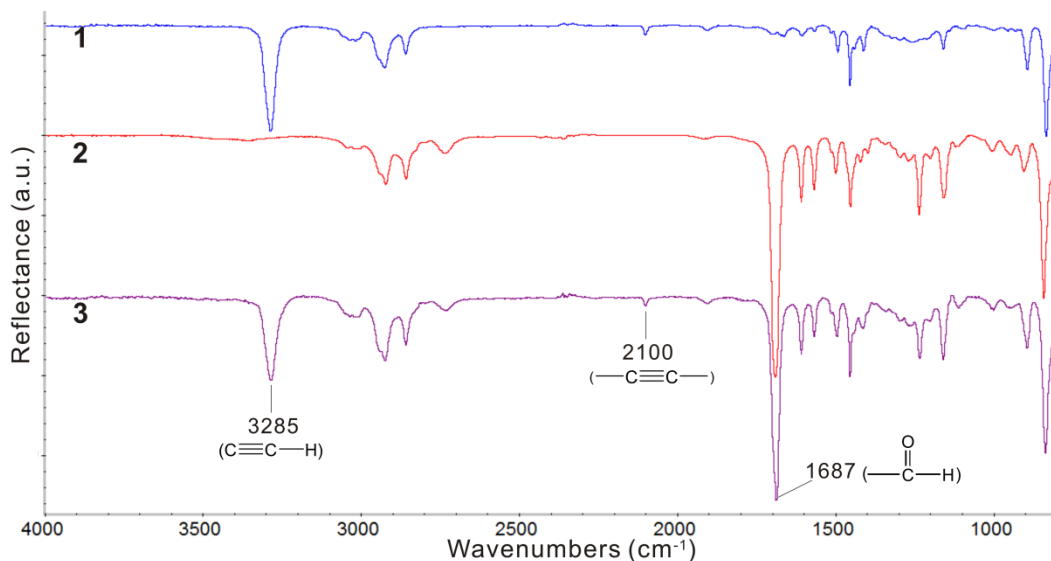


Figure 2.18 FTIR spectra for polymers **1**, **2** and **3**.

Table 2.1 Chemical Composition of polymers **1**, **2** and **3** in atom-% shown as experimental values determined by XPS. Theoretically calculated compositions are included for comparison.

	<u>C-C/H</u>	<u>C-C=O</u>	<u>C=O</u>	<u>$\pi \rightarrow \pi^*$</u>	<u>O</u>
B.E.[eV]	285.0	285.7±0.1	287.7±0.1	291.3±0.1	532^{a)}
1	94.7 (100.0)	- (-)	- (-)	4.0 (-)	1.3 (-)
2	75.7 (83.2)	6.7 (5.6)	5.8 (5.6)	4.3 (-)	7.5 (5.6)
3	85.6 (91.6)	3.5 (2.8)	3.1 (2.8)	4.0 (-)	3.8 (2.8)

^{a)} Experimental values of oxygen ratio[%] are from survey results; Other experimental values for different carbon atoms with different chemical states are from high resolution C1s spectra.

A novel polymer coating with orthogonal functional groups, poly[4-formyl-*p*-xylylene-*co*-4-ethynyl-*p*-xylylene-*co*-*p*-xylylene] (polymer **3**), was synthesized by CVD copolymerization as shown in Figure 2.17a. The precursors 4-ethynyl[2.2]paracyclophane and 4-formyl[2.2]paracyclophane were sublimated with a controlled feed ratio (m:n, m = n in this study). The mixture was then transferred through the pyrolysis zone (670 °C, 0.07 Torr) with help of an argon carrier gas. Free radicals were generated by pyrolysis and subsequently deposited and polymerized on the cooled substrate (15 °C, 0.07 Torr). Under these reaction conditions, CVD co-polymerization yielded polymer **3** as shown in Figure 2.17. Polymers **1** and **2**, which are shown for comparison, denote polymers generated using only one precursor and thus featuring only one reactive functional group (alkyne for **1**; aldehyde for **2**). **1**, **2**, and **3** were characterized by Fourier transform

infrared (FTIR) spectroscopy (Figure 2.18) and X-ray photoelectron spectroscopy (XPS) (Table 2.1). It is clearly shown from the FTIR spectra that **3** has both alkyne (3285, 2100 cm^{-1}) and aldehyde (1687 cm^{-1}) functional groups, while **1** or **2** displays only one type of functional groups. XPS was used to further confirm the surface composition of the films within the outermost 10 nm.¹⁷ The percentage of total carbon and oxygen was obtained from the XPS survey results. High-resolution peak fitting of the C1s signal was used to determine the ratios of different carbon atoms at different chemical states. The position for C—C/H was set to be 285.0 eV for binding energy calibration. Other carbon atoms with different chemical states have different binding energies as shown in Table 2.1. The quantitative XPS experimental data were in good agreement with the theoretical values calculated according to the chemical structures of the starting materials (Figure 2.17a).

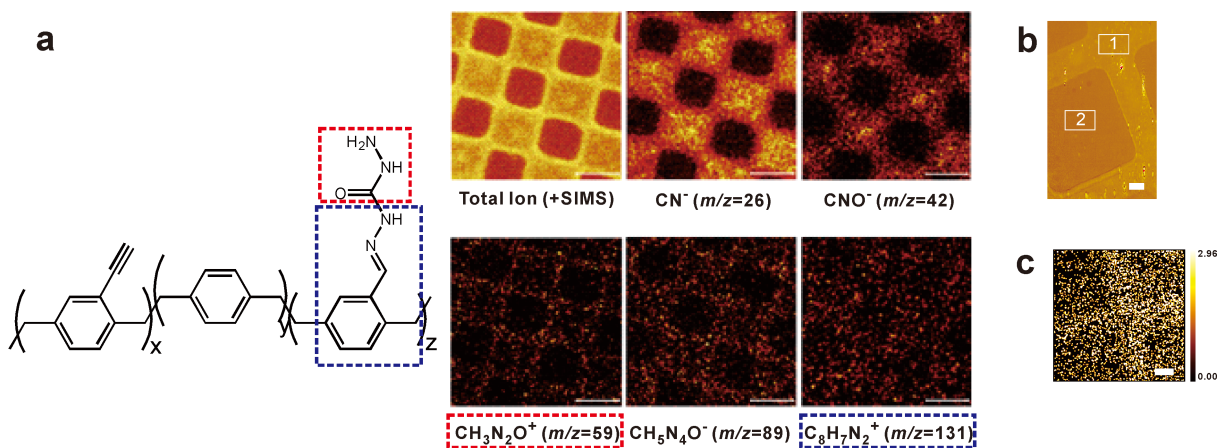


Figure 2.19 a) TOF-SIMS images of carbohydrazide patterned on polymer **3**. The m/z values and their corresponding chemical structures are denoted by squares of different colors. b) Imaging ellipsometry thickness map of carbohydrazide pattern by μ CP, the thickness difference between the marked area 1 and 2 is 0.3 nm. c) Imaging XPS N1s elemental map of the carbohydrazide pattern at 400.0 eV. All scale bars represent 50 μm .

After confirming the successful preparation of the multifunctional reactive coating, each step for the biomolecules immobilization had to be validated. The overall design for our co-immobilization process is shown in Figure 2.17. Heparin was immobilized on the copolymer surface through the hydrazide–aldehyde reaction, which is highly efficient, commonly used for bioconjugation and classified as one of the bioorthogonal reactions.² Carbohydrazide with a hydrazide group on both ends was used to link the aldehyde group of heparin and the aldehyde group on the copolymer **3** surface. To confirm that the carbohydrazide is indeed attached to the surface through covalent reaction, we conducted a ToF-SIMS study. ToF-SIMS is a surface-sensitive analytical tool that provides information on the uppermost few molecular layers. ToF-SIMS has been previously used in materials science,⁶² semiconductor industry,⁶³ geology,⁶⁴ archaeometry,⁶⁵ cosmochemistry,⁶⁶ and biology.⁶⁷ The mass imaging capability of ToF-SIMS combines the potential benefits of chemical imaging and mass spectroscopy.⁶⁸ Sample surfaces in this study were coated with the copolymer **3** and then modified by microcontact printing of the carbohydrazide linker. The resultant patterns were clearly observable in the ToF-SIMS images. For all the images shown in Figure 2.19a, the brighter areas were patterned with carbohydrazide, while the darker areas were not (with only the copolymer **3** coating). Signals at m/z 26 and 42, which corresponded to CN^- and CNO^- signals were predominantly observed within the area patterned with carbohydrazide. Since the polymer itself does not have any nitrogen, the nitrogen-containing mass peaks can be exclusively attributed to the presence of the carbohydrazide. Similarly, mass peaks of m/z 59 and 89, which are characteristic

fragments of the carbonyl linker, are significantly enhanced in the surface-modified areas. Moreover, the mass fragment m/z 131, which coincides with the m/z 59 signal further supports the formation of a covalent bond between the linker and the polymer, albeit with lower contrast. Imaging ellipsometer was also used to investigate thickness variations after carbonyl patterning (Figure 2.19b). The film thickness of the carbonyl immobilized onto copolymer **3** was measured to be 0.3 nm. For comparison, microcontact printing of carbonyl onto polymer **1** was used as a control experiment, which showed no patterns based on imaging ellipsometry (data not shown). This contrast clearly demonstrates the orthogonality of the surface chemistries (i.e., alkyne–azide reaction versus aldehyde–hydrazide reaction). Moreover, XPS mapping of the element nitrogen (Figure 2.19c), which was used as a reporter for the carbonyl linker, further confirmed the ToF-SIMS results. A cross pattern is shown in Figure 2.19c. The relatively low signal-to-noise ratio in the XPS mapping experiment can be attributed to the overall low content of nitrogen on the surface (less than 3%). Still, taken together, the images shown in Figure 2.19 confirm that the carbonyl was covalently attached to the copolymer **3** through the aldehyde–hydrazide reaction.

A surface displaying carbonyl patterns was incubated in periodated heparin (with aldehyde groups) solution overnight followed by thorough rinsing with distilled water. After this heparin immobilization step, a heparin antibody and a dye-conjugated secondary antibody were used for immunostaining (Figure 2.20, top scheme). From the image shown on the top right of Figure 2.20, it is evident that heparin was immobilized only at the surface areas that presented carbonyl.

Two control experiments were performed. For the first one, we used a carbohydrate patterned surface (without the heparin immobilization step) for the immunostaining. For the second control experiment, the heparin-presenting surface was in contact with the secondary antibody only, but not the primary antibody (anti-heparin). Both control experiments did not show fluorescence contrast for the patterns (data not shown).

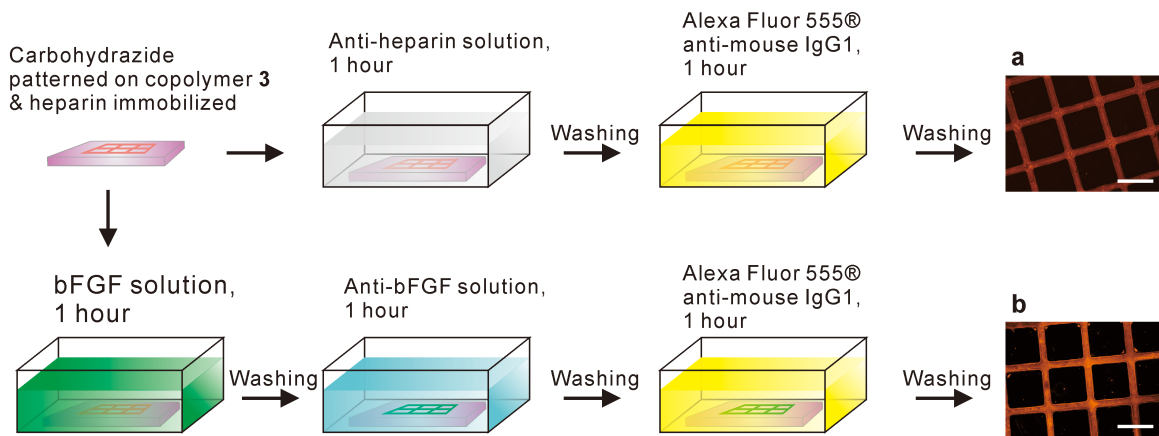


Figure 2.20 Scheme and fluorescence microscope images (a & b) after immunostaining the heparin and bFGF immobilized surface, respectively. In the scheme for this Figure, we use pink to represent heparin and green to represent bFGF, the same colors used in Scheme 1b. a) Fluorescence micrograph after immunostaining the immobilized heparin on the patterned carbohydrate. b) Fluorescence micrograph after immunostaining the immobilized bFGF on the heparin. Scale bars are 500 μm .

After validating the heparin immobilization approach, the heparin-presenting surface was incubated in a bFGF solution (Figure 2.20, bottom scheme), followed by washing and bFGF immunostaining. The bottom right fluorescence micrograph in Figure 2.20 shows that bFGF was only immobilized at the area that presented heparin. Again, we included two control experiments to validate the bFGF

immunostaining. First, the surface was patterned with carbohydrazide (no heparin immobilization), followed by the same bFGF incubation and immunostaining shown as in the bottom scheme of Figure 2.20. Second, we performed every immobilization step for carbohydrazide, heparin and bFGF, but omitted the primary antibody. With other words, the resultant surface was only in contact with the secondary antibody. Both control experiments did not show fluorescence contrast for the patterns (data not shown). For the heparin and the bFGF immunostaining, we used different primary antibody (heparin antibody and bFGF antibody, respectively). Because both antibodies belong to the isotype mouse IgG1 family, we were able to image both with the same secondary antibody (Alexa Fluor® 555 anti-mouse IgG1), hence the identical colors in Figure 2.20. Nevertheless, a clear contrast is observed in both cases confirming the selectivity of both reactions. At this point, we have established the success of each immobilization step towards tethering the heparin-binding growth factor. We finally wanted to establish co-immobilization with a second biomolecule, specifically cRGD, via azide-acetylene coupling.

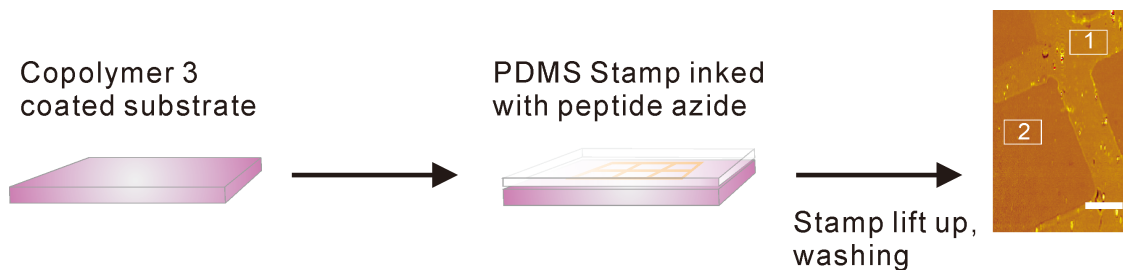


Figure 2.21 Imaging ellipsometry thickness map (on the right side) of a cRGD azide pattern created by μ CP. The thickness difference between the marked area 1 and 2 is 0.5 nm. Scale bar represents 100 μ m.

The results for patterning an azide-functionalized cRGD peptide onto polymer **3** are shown in Figure 2.21. Imaging ellipsometry was used to generate the thickness map for the patterned adhesion peptide on the newly synthesized copolymer **3** (Figure 2.21). The immobilized peptide layer was measured to be 0.5 nm. A control experiment with the same peptide patterned on polymer 2 did not show any pattern contrast (data not shown). This again demonstrates the orthogonality of the alkyne–azide chemistry and the aldehyde–hydrazide chemistry we use. The alkyne–azide chemistry is chosen for immobilization of a second biomolecule, here a cyclic RGD (cRGD) peptide, because of its high efficiency and natural orthogonality to other commonly used bioconjugation chemistries.²³

2.3.4 Conclusion

We successfully prepared a new CVD copolymer for orthogonal co-immobilization of heparin-binding growth factors with an adhesion peptide. To establish a generic growth factor immobilization scheme, the CVD co-polymer was modified to allow for immobilization of heparin onto the surface. The presence of heparin leads to non-covalent binding of heparin-binding growth factors and can potentially enhance the bioactivity of the growth factor. In parallel, an adhesion peptide is also immobilized to the surface using orthogonal bioconjugation schemes. Due to the substrate-independent nature of the CVD polymerization process, this novel procedure is rather generic and can be widely applied as a surface engineering platform for a broad range of biomedical applications. Further

biological studies are under way to identify the quantitative information about the co-immobilization ratios that will be associated with the highest biological activity in cell culture. We note that the biomolecules that can be orthogonally immobilized via the herein reported procedure are not limited to adhesion peptides and growth factors. While other biomolecules such as enzymes, antibodies, or polysaccharides are also compatible with this approach, this strategy is not suitable for co-immobilization of multiple heparin-binding growth factors. In this case, more traditional orthogonal immobilization strategies will need to be employed.²³

References

1. (a) Ratner, B. D.; Bryant, S. J., Biomaterials: Where we have been and where we are going. *Annu Rev Biomed Eng* **2004**, *6*, 41-75; (b) Castner, D. G.; Ratner, B. D., Biomedical surface science: Foundations to frontiers. *Surf Sci* **2002**, *500* (1-3), 28-60.
2. Sletten, E. M.; Bertozzi, C. R., Bioorthogonal Chemistry: Fishing for Selectivity in a Sea of Functionality. *Angew Chem Int Edit* **2009**, *48* (38), 6974-6998.
3. (a) Jewett, J. C.; Bertozzi, C. R., Cu-free click cycloaddition reactions in chemical biology. *Chem Soc Rev* **2010**, *39* (4), 1272-1279; (b) Elkasabi, Y.; Chen, H. Y.; Lahann, J., Multipotent polymer coatings based on chemical vapor deposition copolymerization. *Adv Mater* **2006**, *18* (12), 1521-+.
4. Kolb, H. C.; Finn, M. G.; Sharpless, K. B., Click chemistry: Diverse chemical function from a few good reactions. *Angew Chem Int Edit* **2001**, *40* (11), 2004-+.
5. Johnson, J. A.; Finn, M. G.; Koberstein, J. T.; Turro, N. J., Construction of linear polymers, dendrimers, networks, and other polymeric architectures by copper-catalyzed azide-alkyne cycloaddition "Click" chemistry. *Macromol Rapid Comm* **2008**, *29* (12-13), 1052-1072.
6. (a) Tornøe, C. W.; Christensen, C.; Meldal, M., Peptidotriazoles on solid phase: [1,2,3]-triazoles by regioselective copper(I)-catalyzed 1,3-dipolar cycloadditions of terminal alkynes to azides. *J Org Chem* **2002**, *67* (9), 3057-3064; (b) Rostovtsev, V. V.; Green, L. G.; Fokin, V. V.; Sharpless, K. B., A stepwise Huisgen cycloaddition process: Copper(I)-catalyzed regioselective "ligation" of azides and terminal alkynes. *Angew Chem Int Edit* **2002**, *41* (14), 2596-+.
7. (a) Collman, J. P.; Devaraj, N. K.; Eberspacher, T. P. A.; Chidsey, C. E. D., Mixed azide-terminated monolayers: A platform for modifying electrode surfaces. *Langmuir* **2006**, *22* (6), 2457-2464; (b) Brennan, J. L.; Hatzakis, N. S.; Tshikhudo, T. R.; Dirvianskyte, N.; Razumas, V.; Patkar, S.; Vind, J.; Svendsen, A.; Nolte, R. J. M.; Rowan, A. E.; Brust, M., Bionanoconjugation via click chemistry: The creation of functional hybrids of lipases and gold nanoparticles. *Bioconjugate Chem* **2006**, *17* (6), 1373-1375.
8. (a) Ciampi, S.; Bocking, T.; Kilian, K. A.; James, M.; Harper, J. B.; Gooding, J. J., Functionalization of acetylene-terminated monolayers on Si(100) surfaces: A click chemistry approach. *Langmuir* **2007**, *23* (18), 9320-9329; (b) Nandivada, H.; Chen, H. Y.; Bondarenko, L.; Lahann, J., Reactive polymer coatings that "click". *Angew Chem Int Edit* **2006**, *45* (20), 3360-3363.
9. Chen, H. Y.; Hirtz, M.; Deng, X. P.; Laue, T.; Fuchs, H.; Lahann, J., Substrate-Independent Dip-Pen Nanolithography Based on Reactive Coatings. *J Am Chem Soc* **2010**, *132* (51), 18023-18025.
10. Alf, M. E.; Asatekin, A.; Barr, M. C.; Baxamusa, S. H.; Chelawat, H.; Ozaydin-Ince, G.; Petruczuk, C. D.; Sreenivasan, R.; Tenhaeff, W. E.; Trujillo, N. J.; Vaddiraju, S.; Xu, J.; Gleason, K. K., Chemical Vapor Deposition of Conformal, Functional, and Responsive Polymer Films. *Adv Mater* **2010**, *22* (18), 1993-2027.
11. Chen, H. Y.; Lahann, J., Designable Biointerfaces Using Vapor-Based Reactive Polymers. *Langmuir* **2011**, *27* (1), 34-48.

12. Elkasabi, Y.; Nandivada, H.; Chen, H. Y.; Bhaskar, S.; D'Arcy, J.; Bondarenko, L.; Lahann, J., Partially Fluorinated Poly-p-xylylenes Synthesized by CVD Polymerization. *Chem Vapor Depos* **2009**, *15* (4-6), 142-149.
13. Elkasabi, Y.; Yoshida, M.; Nandivada, H.; Chen, H. Y.; Lahann, J., Towards multipotent coatings: Chemical vapor deposition and biofunctionalization of carbonyl-substituted copolymers. *Macromol Rapid Comm* **2008**, *29* (11), 855-870.
14. Thevenet, S.; Chen, H. Y.; Lahann, J.; Stellacci, F., A generic approach towards nanostructured surfaces based on supramolecular nanostamping on reactive polymer coatings. *Adv Mater* **2007**, *19* (24), 4333-+.
15. Lahann, J.; Balcells, M.; Rodon, T.; Lee, J.; Choi, I. S.; Jensen, K. F.; Langer, R., Reactive polymer coatings: A platform for patterning proteins and mammalian cells onto a broad range of materials. *Langmuir* **2002**, *18* (9), 3632-3638.
16. (a) Trujillo, N. J.; Barr, M. C.; Im, S. G.; Gleason, K. K., Oxidative chemical vapor deposition (oCVD) of patterned and functional grafted conducting polymer nanostructures. *J Mater Chem* **2010**, *20* (19), 3968-3972; (b) Im, S. G.; Gleason, K. K., Systematic control of the electrical conductivity of poly(3,4-ethylenedioxythiophene) via oxidative chemical vapor deposition. *Macromolecules* **2007**, *40* (18), 6552-6556.
17. Elkasabi, Y.; Lahann, J., Vapor-Based Polymer Gradients. *Macromol Rapid Comm* **2009**, *30* (1), 57-63.
18. Jiang, X. W.; Chen, H. Y.; Galvan, G.; Yoshida, M.; Lahann, J., Vapor-based initiator coatings for atom transfer radical polymerization. *Adv Funct Mater* **2008**, *18* (1), 27-35.
19. (a) Chen, H. Y.; McClelland, A. A.; Chen, Z.; Lahann, J., Solventless adhesive bonding using reactive polymer coatings. *Anal Chem* **2008**, *80* (11), 4119-4124; (b) Im, S. G.; Bong, K. W.; Lee, C. H.; Doyle, P. S.; Gleason, K. K., A conformal nano-adhesive via initiated chemical vapor deposition for microfluidic devices. *Lab Chip* **2009**, *9* (3), 411-416.
20. Chen, H. Y.; Rouillard, J. M.; Gulari, E.; Lahann, J., Colloids with high-definition surface structures. *P Natl Acad Sci USA* **2007**, *104* (27), 11173-11178.
21. (a) Tawfick, S.; Deng, X. P.; Hart, A. J.; Lahann, J., Nanocomposite microstructures with tunable mechanical and chemical properties. *Phys Chem Chem Phys* **2010**, *12* (17), 4446-4451; (b) Lau, K. K. S.; Bico, J.; Teo, K. B. K.; Chhowalla, M.; Amaratunga, G. A. J.; Milne, W. I.; McKinley, G. H.; Gleason, K. K., Superhydrophobic carbon nanotube forests. *Nano Lett* **2003**, *3* (12), 1701-1705.
22. Deng, X. P.; Friedmann, C.; Lahann, J., Bio-orthogonal "Double-Click" Chemistry Based on Multifunctional Coatings. *Angew Chem Int Edit* **2011**, *50* (29), 6522-6526.
23. Deng, X. P.; Eyster, T. W.; Elkasabi, Y.; Lahann, J., Bio-Orthogonal Polymer Coatings for Co-Presentation of Biomolecules. *Macromol Rapid Comm* **2012**, *33* (8), 640-645.
24. Deng, X. P.; Lahann, J., A Generic Strategy for Co-Presentation of Heparin-Binding Growth Factors Based on CVD Polymerization. *Macromol Rapid Comm* **2012**, *33* (17), 1459-1465.

25. Chen, H. Y.; Lahann, J., Vapor-assisted micropatterning in replica structures: A solventless approach towards topologically and chemically designable surfaces. *Adv Mater* **2007**, *19* (22), 3801-+.
26. (a) Inglis, A. J.; Barner-Kowollik, C., Ultra Rapid Approaches to Mild Macromolecular Conjugation. *Macromol Rapid Comm* **2010**, *31* (14), 1247-1266; (b) Debets, M. F.; van der Doelen, C. W. J.; Rutjes, F. P. J. T.; van Delft, F. L., Azide: A Unique Dipole for Metal-Free Bioorthogonal Ligations. *ChemBiochem* **2010**, *11* (9), 1168-1184.
27. (a) Sletten, E. M.; Nakamura, H.; Jewett, J. C.; Bertozzi, C. R., Difluorobenzocyclooctyne: Synthesis, Reactivity, and Stabilization by beta-Cyclodextrin. *J Am Chem Soc* **2010**, *132* (33), 11799-11805; (b) Agard, N. J.; Prescher, J. A.; Bertozzi, C. R., A strain-promoted [3+2] azide-alkyne cycloaddition for covalent modification of biomolecules in living systems. *J Am Chem Soc* **2004**, *126* (46), 15046-15047; (c) Baskin, J. M.; Prescher, J. A.; Laughlin, S. T.; Agard, N. J.; Chang, P. V.; Miller, I. A.; Lo, A.; Codelli, J. A.; Bertozzi, C. R., Copper-free click chemistry for dynamic in vivo imaging. *P Natl Acad Sci USA* **2007**, *104* (43), 16793-16797.
28. Ning, X. H.; Guo, J.; Wolfert, M. A.; Boons, G. J., Visualizing metabolically labeled glycoconjugates of living cells by copper-free and fast Huisgen cycloadditions. *Angew Chem Int Edit* **2008**, *47* (12), 2253-2255.
29. (a) Gouin, S. G.; Kovensky, J., A Procedure for Fast and Regioselective Copper-Free Click Chemistry at Room Temperature with p-Toluenesulfonyl Alkyne. *Synlett* **2009**, (9), 1409-1412; (b) Li, Z. M.; Seo, T. S.; Ju, J. Y., 1,3-dipolar cycloaddition of azides with electron-deficient alkynes under mild condition in water. *Tetrahedron Lett* **2004**, *45* (15), 3143-3146.
30. (a) Limapichat, W.; Basu, A., Reagentless functionalization of gold nanoparticles via a 3 + 2 Huisgen cycloaddition. *J Colloid Interf Sci* **2008**, *318* (1), 140-144; (b) Clark, M.; Kiser, P., In situ crosslinked hydrogels formed using Cu(I)-free Huisgen cycloaddition reaction. *Polym Int* **2009**, *58* (10), 1190-1195.
31. Lahann, J.; Choi, I. S.; Lee, J.; Jenson, K. F.; Langer, R., A new method toward microengineered surfaces based on reactive coating. *Angew Chem Int Edit* **2001**, *40* (17), 3166-+.
32. (a) Rozkiewicz, D. I.; Janczewski, D.; Verboom, W.; Ravoo, B. J.; Reinhoudt, D. N., "Click" chemistry by microcontact printing. *Angew Chem Int Edit* **2006**, *45* (32), 5292-5296; (b) Sullivan, T. P.; van Poll, M. L.; Dankers, P. Y. W.; Huck, W. T. S., Forced peptide synthesis in nanoscale confinement under elastomeric stamps. *Angew Chem Int Edit* **2004**, *43* (32), 4190-4193.
33. (a) Weber, P. C.; Ohlendorf, D. H.; Wendoloski, J. J.; Salemme, F. R., Structural Origins of High-Affinity Biotin Binding to Streptavidin. *Science* **1989**, *243* (4887), 85-88; (b) Sano, T.; Smith, C. L.; Cantor, C. R., Immuno-Pcr - Very Sensitive Antigen-Detection by Means of Specific Antibody-DNA Conjugates. *Science* **1992**, *258* (5079), 120-122.
34. (a) Nandivada, H.; Chen, H. Y.; Lahann, J., Vapor-based synthesis of poly [(4-formyl-p-xylylene)-co-(p-xylylene)] and its use for biomimetic surface modifications. *Macromol Rapid Comm* **2005**, *26* (22), 1794-1799; (b) Lahann, J.;

- Klee, D.; Hocker, H., Chemical vapour deposition polymerization of substituted [2.2]paracyclophanes. *Macromol Rapid Comm* **1998**, *19* (9), 441-444.
35. (a) Lahann, J.; Klee, D.; Pluester, W.; Hoecker, H., Bioactive immobilization of r-hirudin on CVD-coated metallic implant devices. *Biomaterials* **2001**, *22* (8), 817-826; (b) Morra, M., Biomolecular modification of implant surfaces. *Expert Rev Med Devic* **2007**, *4* (3), 361-372; (c) Hanefeld, P.; Westedt, U.; Wombacher, R.; Kissel, T.; Schaper, A.; Wendorff, J. H.; Greiner, A., Coating of poly(p-xylylene) by PLA-PEO-PLA triblock copolymers with excellent polymer-polymer adhesion for stent applications. *Biomacromolecules* **2006**, *7* (7), 2086-90.
36. (a) Zhang, Y.; Deng, X. P.; Scheller, E. L.; Kwon, T. G.; Lahann, J.; Franceschi, R. T.; Krebsbach, P. H., The effects of Runx2 immobilization on poly (epsilon-caprolactone) on osteoblast differentiation of bone marrow stromal cells in vitro. *Biomaterials* **2010**, *31* (12), 3231-3236; (b) Hatakeyama, H.; Kikuchi, A.; Yamato, M.; Okano, T., Patterned biofunctional designs of thermoresponsive surfaces for spatiotemporally controlled cell adhesion, growth, and thermally induced detachment. *Biomaterials* **2007**, *28* (25), 3632-3643.
37. (a) Oh, S. J.; Hong, B. J.; Choi, K. Y.; Park, J. W., Surface modification for DNA and protein microarrays. *Omics* **2006**, *10* (3), 327-343; (b) Wang, D. N.; Liu, S. Y.; Trummer, B. J.; Deng, C.; Wang, A. L., Carbohydrate microarrays for the recognition of cross-reactive molecular markers of microbes and host cells. *Nat. Biotechnol.* **2002**, *20* (3), 275-281.
38. Hoffman, A. S.; Hubbell, J. A., Surface-Immobilized Biomolecules. In *Biomaterials Science: An Introduction to Materials in Medicine*, 2nd ed.; Ratner, B. D.; Hoffman, A. S.; Schoen, F. J.; Lemons, J. E., Eds. Elsevier Academic Press: San Diego, 2004; p 225.
39. Dedola, S.; Hughes, D. L.; Nepogodiev, S. A.; Rejzek, M.; Field, R. A., Synthesis of alpha- and beta-D-glucopyranosyl triazoles by CuAAC 'click chemistry': reactant tolerance, reaction rate, product structure and glucosidase inhibitory properties. *Carbohydr. Res.* **2010**, *345* (9), 1123-1134.
40. Nandivada, H.; Jiang, X. W.; Lahann, J., Click chemistry: Versatility and control in the hands of materials scientists. *Adv Mater* **2007**, *19* (17), 2197-2208.
41. (a) Albericio, F., Orthogonal protecting groups for N alpha-amino and C-terminal carboxyl functions in solid-phase peptide synthesis. *Biopolymers* **2000**, *55* (2), 123-139; (b) Zhao, H.; Burke, T. R., Pentafluorophenyl ester activation for the preparation of N,N'-diaroylhydrazines. *Tetrahedron* **1997**, *53* (12), 4219-4230; (c) Theato, P., Synthesis of Well-Defined Polymeric Activated Esters. *J Polym Sci Pol Chem* **2008**, *46* (20), 6677-6687.
42. Ruoslahti, E.; Pierschbacher, M. D., New Perspectives in Cell-Adhesion - Rgd and Integrins. *Science* **1987**, *238* (4826), 491-497.
43. (a) Shakesheff, K. M.; Cannizzaro, S. M.; Langer, R., Creating biomimetic micro-environments with synthetic polymer-peptide hybrid molecules. *J Biomat Sci-Polym E* **1998**, *9* (5), 507-518; (b) Kantlehner, M.; Schaffner, P.; Finsinger, D.; Meyer, J.; Jonczyk, A.; Diefenbach, B.; Nies, B.; Holzemann, G.; Goodman, S. L.; Kessler, H., Surface coating with cyclic RGD peptides stimulates osteoblast adhesion and proliferation as well as bone formation. *Chembiochem* **2000**, *1* (2), 107-114.

44. Haubner, R.; Gratiyas, R.; Diefenbach, B.; Goodman, S. L.; Jonczyk, A.; Kessler, H., Structural and functional aspects of RGD-containing cyclic pentapeptides as highly potent and selective integrin $\alpha(v)\beta(3)$ antagonists. *J Am Chem Soc* **1996**, *118* (32), 7461-7472.
45. (a) Al-Nedawi, K.; Meehan, B.; Kerbel, R. S.; Allison, A. C.; Rak, J., Endothelial expression of autocrine VEGF upon the uptake of tumor-derived microvesicles containing oncogenic EGFR. *P Natl Acad Sci USA* **2009**, *106* (10), 3794-3799; (b) Amin, D. N.; Hida, K.; Bielenberg, D. R.; Klagsbrun, M., Tumor endothelial cells express epidermal growth factor receptor (EGFR) but not ErbB3 and are responsive to EGF and to EGFR kinase inhibitors. *Cancer Res* **2006**, *66* (4), 2173-2180.
46. Liberelle, B.; Boucher, C.; Chen, J. K.; Jolicoeur, M.; Durocher, Y.; De Crescenzo, G., Impact of Epidermal Growth Factor Tethering Strategy on Cellular Response. *Bioconjugate Chem* **2010**, *21* (12), 2257-2266.
47. (a) Kuhl, P. R.; Griffiths, L. G., Tethered epidermal growth factor as a paradigm for growth factor-induced stimulation from the solid phase. *Nat Med* **1996**, *2* (9), 1022-1027; (b) Ito, Y., Covalently immobilized biosignal molecule materials for tissue engineering. *Soft Matter* **2008**, *4* (1), 46-56.
48. Grandis, J. R.; Melhem, M. F.; Gooding, W. E.; Day, R.; Holst, V. A.; Wagener, M. M.; Drenning, S. D.; Tweardy, D. J., Levels of TGF- α and EGFR protein in head and neck squamous cell carcinoma and patient survival. *J Natl Cancer I* **1998**, *90* (11), 824-832.
49. Ullrich, A.; Coussens, L.; Hayflick, J. S.; Dull, T. J.; Gray, A.; Tam, A. W.; Lee, J.; Yarden, Y.; Libermann, T. A.; Schlessinger, J.; Downward, J.; Mayes, E. L. V.; Whittle, N.; Waterfield, M. D.; Seeburg, P. H., Human Epidermal Growth-Factor Receptor Cdna Sequence and Aberrant Expression of the Amplified Gene in A431 Epidermoid Carcinoma-Cells. *Nature* **1984**, *309* (5967), 418-425.
50. (a) Westover, E. J.; Covey, D. F.; Brockman, H. L.; Brown, R. E.; Pike, L. J., Cholesterol depletion results in site-specific increases in epidermal growth factor receptor phosphorylation due to membrane level effects - Studies with cholesterol enantiomers. *J Biol Chem* **2003**, *278* (51), 51125-51133; (b) Waddleton, D.; Ramachandran, C.; Wang, Q. P., Development of a time-resolved fluorescent assay for measuring tyrosine-phosphorylated proteins in cells. *Anal Biochem* **2002**, *309* (1), 150-157.
51. (a) Maeno, S.; Niki, Y.; Matsumoto, H.; Morioka, H.; Yatabe, T.; Funayama, A.; Toyama, Y.; Taguchi, T.; Tanaka, J., The effect of calcium ion concentration on osteoblast viability, proliferation and differentiation in monolayer and 3D culture. *Biomaterials* **2005**, *26* (23), 4847-4855; (b) Walsh, W. R.; Guzelsu, N., Ion Concentration Effects on Bone Streaming Potentials and Zeta-Potentials. *Biomaterials* **1993**, *14* (5), 331-336.
52. (a) Attia, M.; Santerre, J. P.; Kandel, R. A., The response of annulus fibrosus cell to fibronectin-coated nanofibrous polyurethane-anionic dihydroxyoligomer scaffolds. *Biomaterials* **2011**, *32* (2), 450-460; (b) Hynes, R. O., Integrins - Versatility, Modulation, and Signaling in Cell-Adhesion. *Cell* **1992**, *69* (1), 11-25.
53. Ahuja, T.; Mir, I. A.; Kumar, D.; Rajesh, Biomolecular immobilization on conducting polymers for biosensing applications. *Biomaterials* **2007**, *28* (5), 791-805.

54. (a) Teymourian, H.; Salimi, A.; Hallaj, R., Low potential detection of NADH based on Fe₃O₄ nanoparticles/multiwalled carbon nanotubes composite: Fabrication of integrated dehydrogenase-based lactate biosensor. *Biosens Bioelectron* **2012**, *33* (1), 60-68; (b) Sassolas, A.; Blum, L. J.; Leca-Bouvier, B. D., Immobilization strategies to develop enzymatic biosensors. *Biotechnol Adv* **2012**, *30* (3), 489-511.
55. Vroman, L.; Adams, A. L.; Fischer, G. C.; Munoz, P. C., Interaction of High Molecular-Weight Kininogen, Factor-Xii, and Fibrinogen in Plasma at Interfaces. *Blood* **1980**, *55* (1), 156-159.
56. Wendeln, C.; Rinnen, S.; Schulz, C.; Kaufmann, T.; Arlinghaus, H. F.; Ravoo, B. J., Rapid Preparation of Multifunctional Surfaces for Orthogonal Ligation by Microcontact Chemistry. *Chem. Eur. J.* **2012**, *18* (19), 5880-5888.
57. Lahann, J.; Pluster, W.; Rodon, T.; Fabry, M.; Klee, D.; Gattner, H. G.; Hocker, H., Universal approach towards r-Hirudin derivatives with high anti-thrombin activity based on chemical differentiation of primary amino groups. *Macromol Biosci* **2002**, *2* (2), 82-87.
58. (a) Gospodarowicz, D.; Cheng, J., Heparin Protects Basic and Acidic Fgf from Inactivation. *J Cell Physiol* **1986**, *128* (3), 475-484; (b) Vemuri, S.; Beylin, I.; Sluzky, V.; Stratton, P.; Eberlein, G.; Wang, Y. J., The Stability of Bfgf against Thermal-Denaturation. *J Pharm Pharmacol* **1994**, *46* (6), 481-486; (c) Sommer, A.; Rifkin, D. B., Interaction of Heparin with Human Basic Fibroblast Growth-Factor - Protection of the Angiogenic Protein from Proteolytic Degradation by a Glycosaminoglycan. *J Cell Physiol* **1989**, *138* (1), 215-220.
59. Yayon, A.; Klagsbrun, M.; Esko, J. D.; Leder, P.; Ornitz, D. M., Cell-Surface, Heparin-Like Molecules Are Required for Binding of Basic Fibroblast Growth-Factor to Its High-Affinity Receptor. *Cell* **1991**, *64* (4), 841-848.
60. Thompson, L. D.; Pantoliano, M. W.; Springer, B. A., Energetic Characterization of the Basic Fibroblast Growth-Factor Heparin Interaction - Identification of the Heparin-Binding Domain. *Biochemistry-Us* **1994**, *33* (13), 3831-3840.
61. Lahann, J.; Langer, R., Novel poly(p-xylylenes): Thin films with tailored chemical and optical properties. *Macromolecules* **2002**, *35* (11), 4380-4386.
62. (a) Leute, A.; Rading, D.; Benninghoven, A.; Schroeder, K.; Klee, D., Static Sims Investigation of Immobilized Molecules on Polymer Surfaces. *Adv Mater* **1994**, *6* (10), 775-780; (b) Hagenhoff, B.; Benninghoven, A.; Stoppeklangner, K.; Grobe, J., Surface Investigations of Silylated Substrates by Tof-Sims. *Adv Mater* **1994**, *6* (2), 142-144.
63. (a) Mowat, I.; Lindley, P.; McCaig, L., A correlation of TOF-SIMS and TXRF for the analysis of trace metal contamination on silicon and gallium arsenide. *Appl Surf Sci* **2003**, *203*, 495-499; (b) Keller, B. A.; Hug, P., Time-of-flight secondary ion mass spectrometry of industrial materials. *Anal Chim Acta* **1999**, *393* (1-3), 201-212.
64. Hou, X. Q.; Ren, D. Y.; Mao, H. L.; Lei, J. J.; Jin, K. L.; Chu, P. K.; Reich, F.; Wayne, D. H., Application of Imaging Tof-Sims to the Study of Some Coal Macerals. *Int J Coal Geol* **1995**, *27* (1), 23-32.
65. McPhail, D. S., Some applications of SIMS in conservation science, archaeometry and cosmochemistry. *Appl Surf Sci* **2006**, *252* (19), 7107-7112.

66. Stephan, T., Tof-Sims in Cosmochemistry. *Planet Space Sci* **2001**, *49* (9), 859-906.
67. (a) Brunelle, A.; Laprevote, O., Recent advances in biological tissue Imaging with time-of-flight secondary ion mass spectrometry: Polyatomic ion sources, sample preparation, and applications. *Curr Pharm Design* **2007**, *13* (32), 3335-3343; (b) Fletcher, J. S., Cellular imaging with secondary ion mass spectrometry. *Analyst* **2009**, *134* (11), 2204-2215.
68. Colliver, T. L.; Brummel, C. L.; Pacholski, M. L.; Swanek, F. D.; Ewing, A. G.; Winograd, N., Atomic and molecular imaging at the single-cell level with TOF-SIMS. *Anal Chem* **1997**, *69* (13), 2225-2231.

CHAPTER 3

Towards Biosensors Development: Metal Enhanced Fluorescence on CVD Polymer Coated Gold Films

3.1. Introduction

Fluorescence-based detection techniques are widely used in biotechnology and medical detection, sensing and diagnostics.¹ Recent advances in biodetection,² an increasingly refined understanding of biological processes,³ and continuous reconsiderations of environmental threshold values⁴ have contributed to efforts to push detection limits of fluorescence-based detection methods to even lower levels. Lower detection limits are facilitated by higher fluorescence signals as well as reliable methods to minimize background fluorescence.

Over the past years, an increasing number of fluorescence dyes with higher brightness and improved photostability have been introduced.⁵ Quantum dots (Qdots) have also been intensively studied since their first discovery in the early 1980s.^{5c, 6} However, the development of new fluorescence dyes and quantum dots involves complicated synthesis process and the resulted quantum yield could still be low.^{5c, 7} Traditionally, a quantum yield above 0.1 is already considered “high”.^{5c, 7}

While the improvement that can be expected from further improved fluorophores is limited, the actual imaging substrates can actively contribute to the

fluorescence detection. Fluorescence interference contrast (FLIC) microscopy, for instance, is based on the self-interference of fluorescent light emitted by fluorophores in the vicinity of a reflecting surface (usually a polished silicon wafer).⁸ The fluorescence intensity oscillates as a function of distance between the fluorescent molecules and the silicon surface, which has been proposed to act as a nanoscale ruler for distance measurements.⁸ Metal enhanced fluorescence (MEF) is another substrate-based phenomenon that can increase fluorescence signals.^{1,9} MEF has been studied for many applications, such as antibody-based bioassays,¹⁰ plasmonic nanoantennas,¹¹ biosensors¹ and the quantification of bacterial adhesion.¹² Surface plasmon coupling and interference effects are among the proposed mechanisms for MEF, although many fundamental aspects remain unanswered.^{1,9a,b,12-13}

If metal films are used as imaging substrates, quenching of the fluorescence signal occurs for fluorophores located within ~10 nm from the surface.^{10,14} Dielectric spacer layers have been used to avoid quenching and even to increase the fluorescence signal. The most widely employed material has been silica,^{10,14a,b} but other materials, such as layers of proteins, have also been used.^{14c,15}

In this study, we introduce a novel class of dielectric spacer layers based on reactive polymer films, which offer three distinct advantages: (1) The CVD polymerization platform provides a wide selection of functional groups, including aldehyde, ketones, amine, alkyne, vinyl, anhydride, active ester, hydroxyl, fluorine, photo-reactive benzoyl group and bromoisobutyrate group for initiating atom

transfer radical polymerization.¹⁶ Moreover, surface functionalization and spacer layer deposition is achieved through a highly defined one-step process. This is advantageous compared to silica substrates, which needs to be modified *via* silane chemistries. In addition, the CVD polymerization process can lead to multiple functional groups in defined surface ratios and gradients,¹⁷ which is not easily achievable by other methods. (2) The CVD polymer coatings are conformal and pinhole-free, with extremely well controlled thickness in the nanometer range. This is prerequisite for optimizing the spacer layer thickness to achieve maximum fluorescence enhancement. Furthermore, micro-patterns with different polymer thicknesses and different functional groups can be produced *via* CVD polymerization.¹⁸ (3) The CVD polymer coating can be easily integrated with micro- and nano- fabrication processes,¹⁹ which are commonly used in high-throughput bioassays and biosensor fabrication.^{3a} The CVD process is not only applicable for the planar surfaces shown here, but also complex geometries providing access to a wide range of sensor designs.

3.2 Experimental Section

3.2.1 Electron Beam Evaporation Metal Coating

One-side polished 4-inch silicon wafers (Silicon Valley Microelectronics, Inc.) were coated by a Denton Vacuum DV-502A E-Beam Evaporator according to the standard operation procedure. First, a 5 nm Ti adhesion layer and then 35 nm or

100 nm gold was coated at 1.0 Å/s. Metal patterns were generated by applying polydimethylsiloxane (PDMS) micro-stencils on the wafers before loading them into the E-beam evaporator. The micro-stencils were well adhered to the wafers during the coating process. We reported the details for the micro-stencils preparation in our previous papers.^{18a, 20}

3.2.2 CVD Precursor Synthesis

All chemicals were purchased from Aldrich and VWR and used as received. Routine monitoring of reactions was performed using silica gel coated aluminium plates (silica gel 60), which were analysed under UV-light at 254 nm. All NMR spectra were recorded on a *Bruker Avance III* spectrometer as solutions. ¹H-NMR: chemical shifts are given in parts per million (ppm, δ) and are referenced to CHCl₃ (7.26 ppm) as an internal standard. All coupling constants are absolute values and *J* values expressed in Hertz (Hz). The description of signals include: s = singlet, d = doublet, q = quartet, m = multiplet, dd = doublet of doublets, ddd = doublet of dd, etc. The spectra were analysed according to first order. ¹³C-NMR: Chemical shifts are expressed in parts per million (ppm, δ) referenced to CDCl₃ (77.0 ppm) as an internal standard. ¹⁹F-NMR: Chemical shifts were calculated from the spectrometer without internal standard. Mass spectra were recorded on a *Finnigan MAT95*. IR spectra were recorded on a *Bruker IFS 88*. Samples were measured on KBR or directly (ATR).

The polymer **1** precursor 4,12-diformyl[2.2]paracyclophane started with the synthesis of the compound 4,12-dibromo[2.2]paracyclophane, which was

synthesized by a slightly modified literature procedure.²¹ First, bromine (12.4 ml, 38.8 g, 243 mmol) was dissolved in 100 ml tetrachloromethane and 15 ml of this solution was added dropwise to iron powder (250 mg, 4.48 mmol) in a 1 liter round bottom flask. After stirring for 1h the mixture was diluted with 350 ml tetrachloromethane and [2.2]paracyclophane (25.0 g, 120 mmol) was added. The remaining bromine solution was added dropwise over a period of 3h and stirring remained for 16h. A saturated aqueous thiosulfate solution (5ml) was carefully added and the solid was filtered off. The residue was washed with water (100 ml), ethanol (100 ml) and pentane (100 ml), then refluxed in dichloromethane (1.2 liter) and filtered again. The solution was now concentrated (to a total volume of 700 ml) and cooled to -30 °C. After filtration the 4,12-dibromo[2.2]paracyclophane compound (12.0 g, 27%) was obtained as a colorless solid. **¹H NMR** (500 MHz, CDCl₃): 7.15 (dd, *J* = 7.8 Hz, 1.7 Hz, 2H, aromatic), 6.52 (d, *J* = 1.7 Hz, 2H, aromatic), 6.44 (d, *J* = 7.8 Hz, 2H, aromatic), 3.45 (ddd, *J* = 13.1 Hz, 10.4 Hz, 2.4 Hz, 2H, CH₂), 3.16 (ddd, *J* = 12.9 Hz, 10.4 Hz, 5.0 Hz, 2H, CH₂), 2.95 (ddd, *J* = 12.9 Hz, 10.8 Hz, 2.4 Hz, 2H, CH₂), 2.85 (ddd, *J* = 13.1 Hz, 10.8 Hz, 5.0 Hz, 2H, CH₂) ppm. **¹³C NMR** (125 MHz, CDCl₃): 141.2, 138.5, 137.3, 134.1, 128.3, 126.7, 35.4, 32.8 ppm. **FT-IR** (ATR): 2933, 1583, 1535, 1473, 1390, 1186, 1030, 899, 855, 830, 706, 669, 648, 523, 464 cm⁻¹. **m.p.**: 225 °C (lit:²¹ 235 °C). **HR-MS (EI)**: 363.9462 (calculated for [M⁺], C₁₆H₁₄Br₂), 363.9640 (observed). Analytical data agree with literature.²¹

Under an argon atmosphere 4,12-dibromo[2.2]paracyclophane (3.51 g, 9.59 mmol) was dissolved in 175 ml THF and cooled to -78 °C. Then *n*-BuLi (21.4 ml, 34.2 mmol, 1.6 m in hexane) was slowly added and the solution was stirred at -78

°C for 9h. DMF (5.88 ml, 5.53 g, 75.6 mmol) was added dropwise and the solution was slowly warmed to room temperature (over 4 h) and stirred for further 16 h. After addition of sat. NH₄Cl solution (100 ml) the mixture was acidified by 1 M HCl solution. Ethyl acetate (150 ml) was added and the phases were separated. The aqueous phase was extracted with ethyl acetate (150 ml) and the combined organic phases were dried over MgSO₄. After filtration and evaporation of the solvent, the crude product was purified by column chromatography (eluent: CH₂Cl₂) yielding the product (1.13 g, 45%) 4,12-diformyl[2.2]paracyclophane as a colorless solid. **¹H NMR** (500 MHz, CDCl₃): 9.94 (s, 2H, CHO), 7.05 (d, *J* = 1.9 Hz, 2H, aromatic), 6.64 (dd, *J* = 7.8 Hz, 1.9 Hz, 2H, aromatic), 6.52 (d, *J* = 7.8 Hz, 2H, aromatic), 4.13 (ddd, *J* = 13.3 Hz, 10.5 Hz, 2.4 Hz, 2H, CH₂), 3.29 (ddd, *J* = 13.4 Hz, 10.7 Hz, 2.4 Hz, 2H, CH₂), 3.16 (ddd, *J* = 13.4 Hz, 10.5 Hz, 5.8 Hz, 2H, CH₂), 3.02 (ddd, *J* = 13.3 Hz, 10.7 Hz, 5.8 Hz, 2H, CH₂) ppm. **¹³C NMR** (125 MHz, CDCl₃): 191.9, 142.9, 140.5, 137.0, 136.8, 136.5, 135.2, 34.3, 32.8 ppm. **FT-IR** (ATR): 1670, 1587, 1223, 1137, 862, 721, 649 cm⁻¹. **m.p.**: 233 °C. **EI-MS** [70 eV, *m/z* (%)]: 264 (84) [M⁺], 209 (39) [C₁₅H₁₃O], 132 (91) [C₉H₈O]⁺, 104 (100) [C₈H₈]⁺. **HR-MS (EI)**: 264.1150 (calculated for [M⁺], C₁₈H₁₆O₂), 264.1152 (observed). Analytical data agree with literature.²²

3.2.3 CVD Polymerization

Poly(diformyl-*p*-xylylene) (polymer **1**) and poly[(4-aminomethyl-*p*-xylylene)-*co*-(*p*-xylylene)] (polymer **2**) were synthesized *via* CVD polymerization as shown in Figure 3.1. The CVD process was carried out at 0.07 torr, with 20 sccm argon as carrier gas. The precursor was sublimed at 90-110°C in vacuum and

converted into the corresponding diradical by thermal pyrolysis (670°C) under vacuum. The diradicals then spontaneously adsorbed and polymerized on the cooled (15°C) substrate placed on top of a rotating stage. The deposition rate was controlled at 0.5 Å/s and the resulted film thickness was controlled by different precursor feeding amount (Supplemental Figure 3.8). To generate surfaces with polymer micro-patterns by multiple-step CVD as shown in Figure 3.6, polymer **1** was coated on the surface multiple times with different monomer feeding amount and with the help of PDMS masks.

3.2.4 Polymer Coating Characterization

FTIR spectra of the CVD polymer films were recorded on a Nicolet 6700 spectrometer with the grazing angle accessory (Smart SAGA) with a 80° fixed angle of incidence. XPS spectra were acquired on an Axis Ultra X-ray photoelectron spectrometer (Kratos Analyticals, UK) equipped with a monochromatized AlK α X-ray source. All spectra were calibrated with respect to the non-functionalized aliphatic carbon with a binding energy of 285.0 eV. Thicknesses were measured on silicon or gold substrates with an Imaging Spectroscopic Ellipsometer (Accurion, Nanofilm EP³-SE). Ellipsometric parameters were fitted using the Cauchy model. The imaging lateral resolution is ~2 μ m for the 10 \times objective.

3.2.5 Fluorescent Molecules Immobilization and Imaging

Three different types of molecules were used in this study and their immobilizations are respectively described below. Alexa Fluor® 488 conjugated

fibrinogen, Alexa Fluor® 555 hydrazide and the SYBR® Gold nuclear gel stain were purchased from Life Technologies Corporation. The lambda DNA (48,502bp) was acquired from Promega.

For the Alexa Fluor 488 conjugated fibrinogen immobilization, surfaces of different thicknesses with or without pattern were incubated in the Alexa Fluor® 488 conjugated fibrinogen PBS solutions for 5h. The concentration was 100 µg/ml for all the experiments except the concentration dependence study shown in Supplemental Figure 3.9. For the concentration dependence study, different concentrations ranging from 0.1 to 100 µg/ml were used. All samples were washed five times with PBS and five times with deionized water before air drying and imaging.

Alexa Fluor 555 hydrazide was dissolved in water with highly diluted hydrochloric acid (pH=5), with a final concentration of 10 µg/ml for all experiments except the concentration dependence study shown in Supplemental Figure 3.10. Different concentrations ranging from 0.01 to 10 µg/ml were used for the concentration dependence study. Surfaces were incubated in the Alexa Fluor 555 hydrazide solutions for 12 h, followed by thorough washing with deionized water and air drying.

For the lambda DNA experiments, SYBR® Gold nuclear gel stain (10,000X Concentrate in DMSO) was diluted 10,000 fold in Tris-EDTA (TE) 1X Solution (pH 7.6). 10 µl Lambda DNA TE solution was added to 1 ml of the diluted SYBR gold TE solution, making the final DNA concentration 10 µg/ml. The DNA and the SYBR Gold

dye were well mixed and kept in the dark for 12 hours. For the immobilization experiments, the SYBR gold stained DNA solution was diluted in DNA grade pure water (Fisher Scientific) to 50 ng/ml. The polymer **2** coated surfaces were incubated in the 50 ng/ml SYBR Gold stained DNA solution for 30 min before thorough rinsing with the DNA grade pure water and air-drying.

All the procedures described above were carried out in the dark. All the air-dried surfaces with the fluorescent molecules were imaged with a fluorescence microscope (Nikon Eclipse 80i) within 15 min of drying. The exposure time for all fluorescence imaging acquisition is 100 ms. The software package ImageJ was used for quantifying fluorescence intensity. Background intensity was subtracted to calculate the final quantified result (Before in contact with the fluorophore solution, each piece of sample was measured under the fluorescence microscope with the acquisition settings the same as afterwards. These images were used as background.).

3.3 Results and Discussion

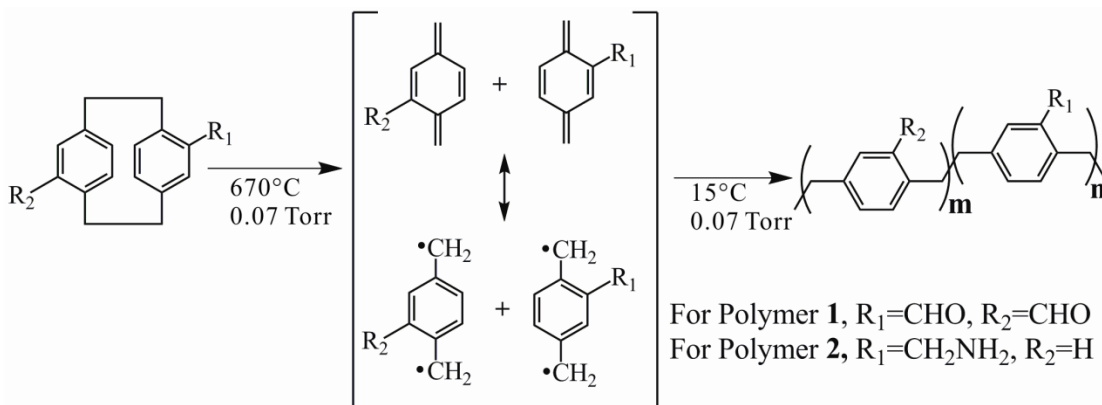


Figure 3.1 Chemical vapor deposition polymerization scheme for the two types of polymers used in this study.

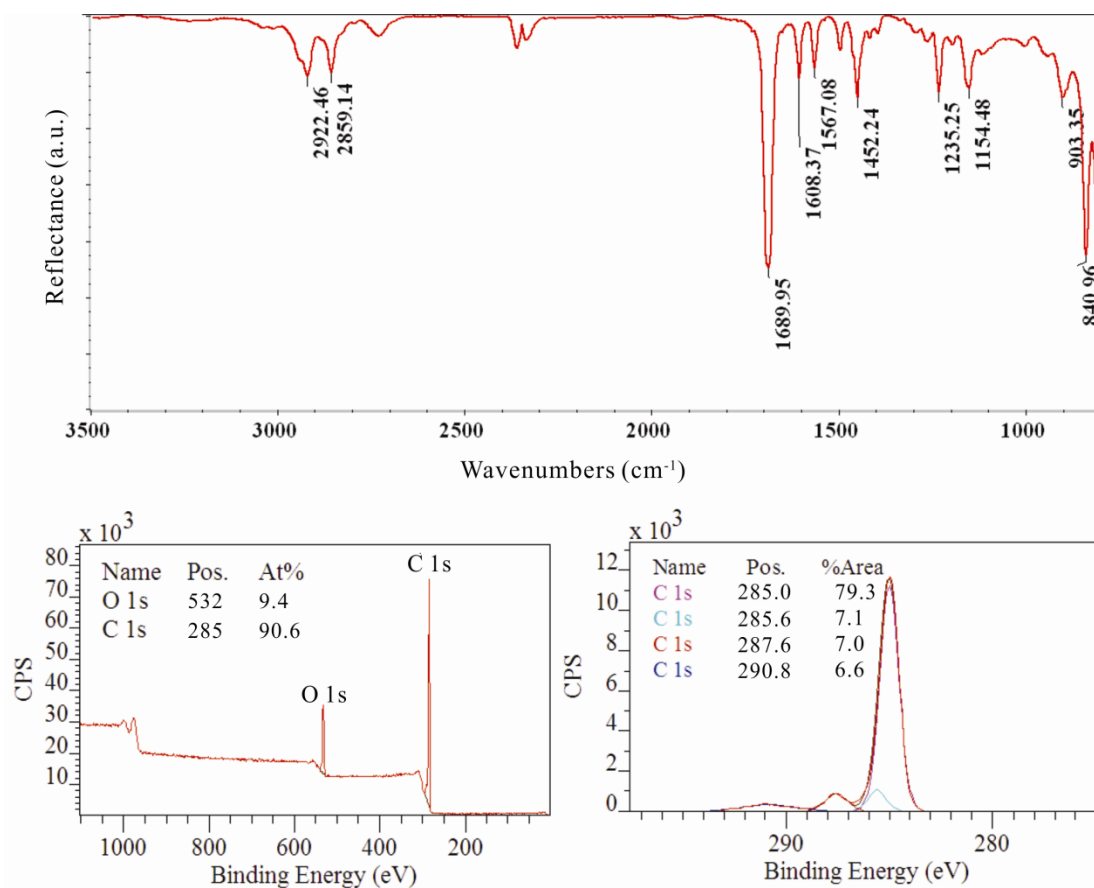


Figure 3.2 FTIR and XPS spectra of polymer 1.

As shown in Figure 3.1, two different types of polymer coatings were synthesized via CVD polymerization. Polymer **1** and polymer **2** differ in the type of functional groups that are available for further surface modification; i.e., aldehyde groups (polymer **1**) vs. amino groups (polymer **2**). For both polymers, the corresponding [2.2]paracyclophanes (dimer) were sublimed at around 100 °C in an argon carrier gas, heated to 670 °C and cleaved into monomers. The monomers were then adsorbed onto the cooled substrates and polymerized at 15 °C, forming conformal polymer coatings with controlled thicknesses. The CVD polymerization process is conducted in vacuum at 0.07 torr. The spectra shown in Figure 3.2 are reported for the newly synthesized polymer **1**. The strong IR peak at 1689 cm⁻¹ is characteristic of the aldehyde functional group. The XPS data present the surface composition of polymer **1** within the outermost 10 nm. Values generated from the experimental spectra by CasaXPS software are listed in Figure 3.2. The survey results indicate that the atom ratios of C and O are 90.6% and 9.4%, respectively. These experimental values are in good accordance with the theoretical calculated values from the chemical structure of polymer **1**, which show C 90.0% and O 10.0%. The high resolution C_{1s} region presents 3 carbon atoms with different chemical states: C-C/H at 285.0 eV, C-C=O at 285.6 eV, C=O at 287.6 eV, and the π→π* signal at 290.8 eV. The atom ratios of the three different carbon species are 79.3%, 7.1%, and 7.0%, respectively. The polymer **1** is stable in common organic solvents, such as acetone and chloroform. It remained intact after assessment of the adhesion by the scotch tape test method,²³ confirming excellent adhesion of polymer **1**. Polymer **2** was published previously^{17a} and the FTIR and XPS data the polymer prepared in this

study via CVD polymerization were in excellent agreement with previously reported data.

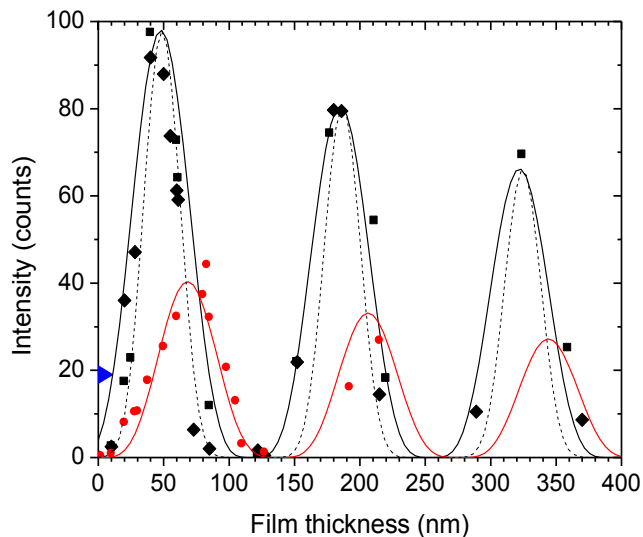


Figure 3.3 a) Fluorescence intensity of Alexa Fluor® 488 conjugated fibrinogen adsorbed on different substrates (35 nm gold – squares, 100 nm gold – diamonds, silicon – circles, triangle – glass) coated with polymer **1** films of different thicknesses. Black solid line: Eq. (1) with $I_0=105$ counts, $a=488$ nm, $b=700$ nm, $c=20$ nm; Black dashed line: same as black solid line but with $\sin^{10}(x)$ instead of $\sin^4(x)$ dependence; Red line: Eq. (2) with $I_0=45$ counts, $a=488$ nm, $b=700$ nm.

After the polymer **1** was synthesized and characterized, it was deposited on silicon, glass and gold substrates. Figure 3.3 shows the fluorescence intensity of different surfaces coated with polymer **1** after being incubated in Alexa Fluor 488 conjugated fibrinogen for 5 hours, washed and air-dried. Fibrinogen is selected here because it adsorbs strongly to hydrophobic surfaces and is usually used as a model for “sticky” serum proteins.²⁴ The concentration was sufficiently high to fully saturate the surface (Supplemental Figure 3.9).

On gold layers with a thickness of either 35 nm or 100 nm, the peak fluorescence signal was significantly enhanced, with peak intensity ~4 times the intensity that exhibits on polymer-coated glass. Previous reports suggest that a gold thickness in the range of 30 to 60 nm is optimal for field enhancement.²⁵ In this study, the observed fluorescence from fluorophores above 35 nm and 100 nm gold coated substrates shows no obvious difference. Importantly, the observed fluorescence is close to zero when the polymer thickness is <10 nm as well as near 120 nm. The fluorescence signal can be fit with equation (1):

$$I(h) = I_0 \cdot \sin^4(2\pi n(h+c)/a) \cdot \exp(-h/b) \quad \text{Eq. (1)}$$

where I_0 is a fit constant, n is the refractive index of the coating ($n=1.77$ for polymer **1** at $\lambda=500$ nm), a is a fit parameter in between the excitation and emission wavelengths of the dye, and b is a fit parameter capturing the decaying coherence between excitation and emission modulation and different angles of illumination and emission as well as the limited depth-of-field of the objective. Here, the constant $c=20$ nm represents an offset in the height which accounts for the slight penetration of the light into the gold film. The fit between the experimental data is further improved when the \sin^4 -dependence (solid line) is replaced by a \sin^{10} -dependence (dashed line). This sharpening of the height dependence is likely the result of multiple internal reflections of light passing through the coating, in a manner reminiscent of a Fabry-Perot etalon.

For comparison, we also assessed the case where silicon substrates were used instead of gold surfaces. The CVD coated silicon substrate showed a clear

interference contrast pattern (Figure 3.3), where the fluorescence intensity I as function of the layer thickness h can be approximated by^{8b, 26}:

$$I(h) = I_0 \sin^4(2\pi nh/a) \exp(-h/b) \quad \text{Eq. (2)}$$

While the maximal fluorescence intensity I_0 can theoretically be up to four-fold higher than the fluorescence signal without a reflecting surface, constructive interference is typically not achieved for all excitation/emission angles and wavelengths simultaneously. Additional complexity is introduced by the effect of the polymer coating with a high refractive index on the emission pattern of the fluorophores positioned at the coating-air interface.²⁷ Despite these complexities, equation (1) with a chosen to be equal to the excitation wavelength and $b=700$ nm captures the functional dependence of the fluorescence signal on the coating thickness well.

The peak fluorescence signal on polymer **1** coated silicon is approximately twice the fluorescence signal observed for a glass substrate covered with a 100 nm layer of polymer **1**. A glass substrate coated with 100 nm thick film of polymer **1** was chosen as the reference substrate for calculating the enhancement factor, because the polymer coated glass substrates did not show thickness-dependent fluorescence intensity. Due to higher roughness of the glass surface compared to the polished silicon or the gold-coated silicon, we chose the 100 nm polymer thickness to ensure full surface coverage.

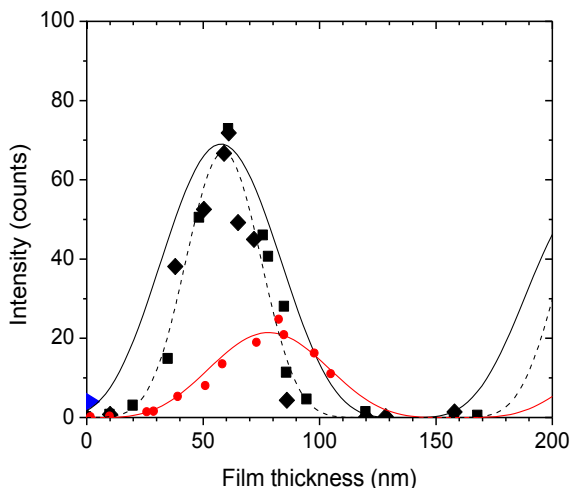


Figure 3.4 a) Fluorescence intensity of Alexa Fluor® 555 hydrazide covalently immobilized on different substrates (35 nm gold – squares, 100 nm gold – diamonds, silicon – circles, triangle – glass) coated with polymer **1** of different thicknesses. Black solid line: Eq. (1) with $I_0=73$ counts, $a=560$ nm, $b=700$ nm, $c=20$ nm; Black dashed line: same as black solid line but with $\sin^{10}(x)$ instead of $\sin^4(x)$ dependence; Red line: Eq. (2) with $I_0=24$ counts, $a=560$ nm, $b=700$ nm.

Notably, the polymer coating **1** contains free aldehyde groups (Figure 3.2), which can be readily conjugated with ligands or dyes containing hydrazine or hydrazide groups. This is a commonly used bioconjugation reaction, which has been previously used for immobilization of biomolecules.²⁸ In the current study, we used this reaction to immobilize Alexa Fluor 555 hydrazide molecules to polymer **1**. Again, care was taken to ensure that the concentration of Alexa Fluor 555 hydrazide and the reaction time was sufficiently high to saturate the surface (Supplemental Figure 3.10).

Figure 3.3 and Figure 3.4 shows that the dependence of the fluorescence signal on the coating thickness can again be described by Eq. (1) on gold surfaces of 35 nm and 100 nm thickness and Eq. (2) on a silicon surface. Relative to the

reference substrate of 100 nm polymer **1** coated glass, the peak fluorescence on the silicon substrate is approximately 4-fold higher, while the fluorescence of Alexa Fluor 555 hydrazide is enhanced 18-fold on the gold substrates.

The difference in enhancement factors between the Alexa Fluor 488 conjugated fibrinogen and the Alexa Fluor 555 hydrazide might be attributed to differences in the initial quantum yields of the two dyes.^{1, 9b, c} For free dyes, the quantum yield for Alexa Fluor 488 is 0.92, and for Alexa Fluor 555 only 0.1.²⁹ The Alexa Fluor 488 fibrinogen conjugate has lower quantum yield than the Alexa Fluor 488 dye itself.^{5a} On the CVD substrates, we found the enhancement factor for the Alexa Fluor 555 hydrazide with a low initial quantum yield to be much higher than that of Alexa Fluor 488, which is consistent with previously reported studies, where the most dramatic relative changes were found for fluorophores with the lowest quantum yields.^{1, 9b, c} It is thought that the intensity enhancement is dictated by the increased radiative decay rate/ spontaneous emission rate of the fluorophore, which, in turn, leads to an increase of the quantum yield and intensity.^{1, 9b, c}

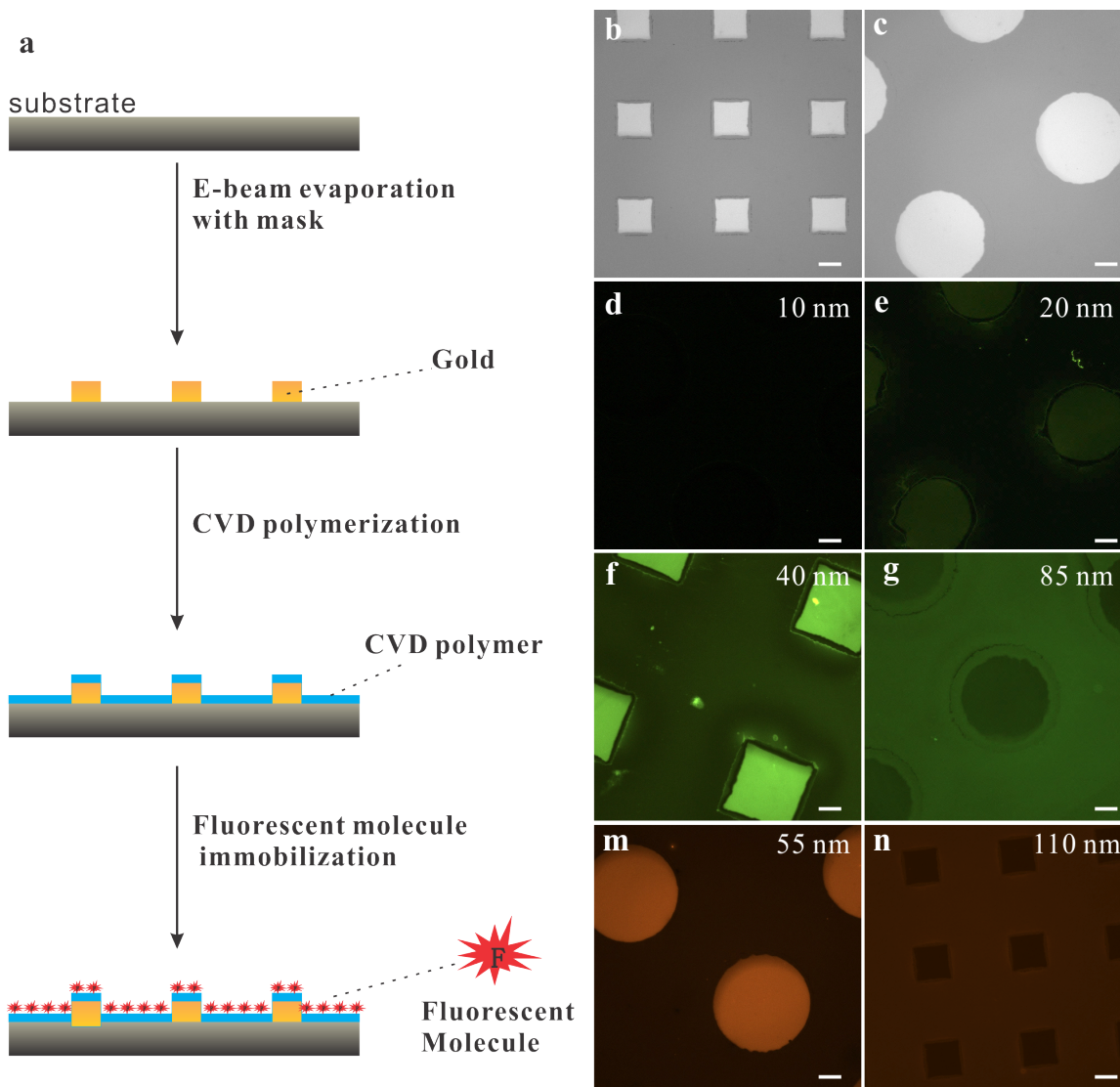


Figure 3.5 a) Scheme for surface treatment to the samples shown in this figure. b) and c): Bright-field images for polished silicon wafer patterned with 35nm gold film inside the squares and circles features; d), e), f), g): the gold patterned silicon substrates similar as shown in b) and c) were coated with polymer **1** of different thicknesses (10nm, 20nm, 40nm, 85nm, respectively) and then incubated in Alexa Fluor 488 conjugated fibrinogen solution (100 $\mu\text{g}/\text{ml}$ in PBS) for 5 hours followed by thorough rinsing and drying before fluorescence microscope imaging; m) and n): the gold patterned silicon substrates were coated with polymer **1** of different thicknesses (55nm and 110nm, respectively) and then incubated in Alexa Fluor 555 hydrazide solution (10 $\mu\text{g}/\text{ml}$, pH=5) for 12 hours followed by thorough washing and drying before fluorescence microscope imaging. All scale bars represent 100 μm .

To directly confirm the role of the gold substrate, we micropatterned gold islands onto silicon wafers using an electron beam evaporation process (Figure 3.5a). This configuration allows us to directly compare gold-coated areas with a bare silicon substrate. The resulting gold patterns on the silicon wafer are shown in Figures 3.5b & c, with the gold substrates appearing as circles or squares. The patterned substrates were then coated with a layer of polymer **1** *via* CVD polymerization. Specific care was taken to ensure the same polymer thickness on top of the gold and the silicon areas. These polymer coated surfaces (with the polymer layer thicknesses noted in Figure 4) were used to immobilize Alexa Fluor 488 conjugated fibrinogen (Figures 3.5 d-g) as well as Alexa Fluor 555 hydrazide (Figures 3.5 m & n). The surface treatment procedure is illustrated schematically in Figure 3.5a. The micro-patterned surfaces displayed the same trend with respect to fluorescence intensity change as observed in Figures 3.3 and 3.4. The surface featuring a 10 nm-thick coating of polymer **1** was dark. In contrast, brighter fluorescence was observed on the surface of the 20 nm-thick polymer coating. This trend continued for the 40 nm-thick polymer coating. Figure 3.5g and Figure 3.5n had the reverse pattern contrast compared to Figures 3.5e, 3.5f & 3.5m, with the fluorescence intensity on the polymer coated silicon area higher than the polymer coated gold area. This is consistent with what we observed in Figure 3.3 and Figure 3.4, because they both fall into the thickness range where the fluorescent molecules on the polymer-coated gold actually have lower intensity than the polymer-coated silicon. Thus the observed fluorescence pattern can be completely reversed, depending on what polymer thickness is employed.

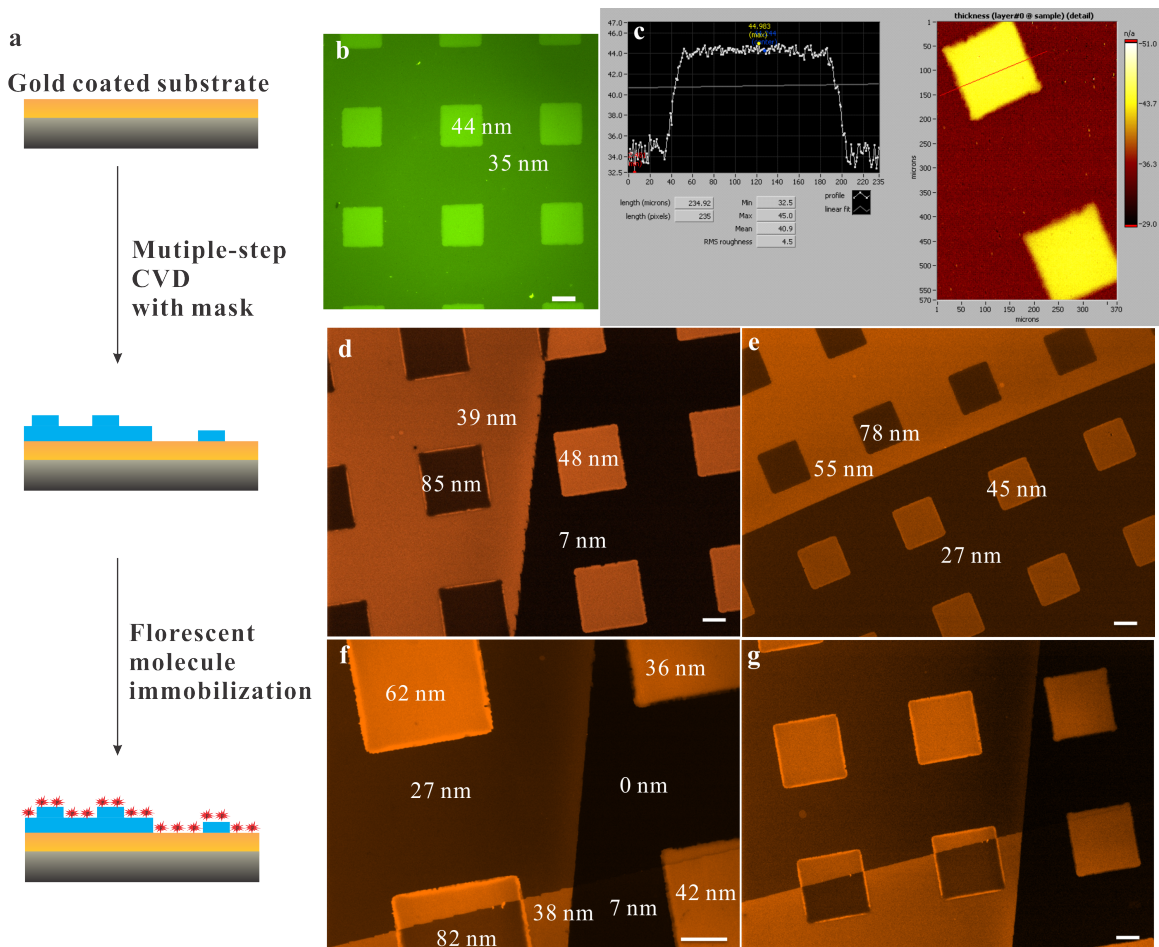


Figure 3.6 All substrates here are polished silicon wafers coated with 100 nm homogenous gold film (no metal pattern). The feature contrast shown in all the images is from different polymer film thickness inside and outside the squares after Multiple-step VAMPIR CVD coating. a) Scheme for surface treatment to the samples shown in this figure. The numbers in b), d), e), f), g) show the thicknesses of different areas. b): The gold substrate coated with polymer **1** (44nm inside the squares and 35nm outside the squares) was incubated in Alexa Fluor® 488 conjugated fibrinogen solution (100 µg/ml in PBS) for 5 hours followed by thorough wash and drying. Fluorescence microscope image was taken in the FITC channel; c): Imaging ellipsometry thickness map and line profile for the same sample shown in b) before in contact with the fibrinogen. d), e), f), g): The gold substrate were coated with polymer **1** of different thicknesses in different areas (thicknesses noted in the images), and then incubated in Alexa Fluor® 555 hydrazide solution (10 µg/ml, pH=5) for 12 hours followed by thorough rinsing and drying. Fluorescence microscope images were then acquired in the Cy3 channel. g) shows the same sample as f) with different magnification. All scale bars represent 100 µm.

Next, we wanted to assess the impact of regions of different polymer thicknesses on an isotropic gold film. Direct polymer microstructuring during the CVD polymerization has been shown in the past,^{18b} and can be easily applied to the various substrates studied in this work. This approach can give rise to patterns with different polymer thicknesses (Figure 3.6a). Polymer **1** was coated onto a homogenous gold surface *via* the VAMPIR process, which is a multiple-step CVD coating process that uses PDMS masks to create terraces of varying thicknesses. All micro-engineered polymer coatings thicknesses in different patterned regions were then measured by imaging ellipsometry before the samples were brought in contact with the fluorescent molecules. The imaging ellipsometry thickness map (Figure 3.6c) for the same sample shown in Figure 3.6b is a representative example of the polymer pattern thickness measurements employed in this study. The different film thicknesses are noted in the fluorescence microscope images shown in Figure 3.6. Figures 3.6 b & d-g clearly show how a chemically isotropic surface can give sharp fluorescence intensity contrast simply by changing the spacer layer thicknesses patterned on different regions of the same surface. Remarkably, the intensity change of the immobilized fluorescent molecules on the polymer patterned surfaces show the same trend as Figure 3.3 and Figure 3.4.

In sensor design and biodetection applications, a high signal-to-noise ratio is critical for the determination of a fluorescence signal, since lots of factors can confound the fluorescence measurement such as excess environmental fluorescence, autofluorescence, arbitrary gain settings in the microscope, lens effects, or the presence of water and other molecules in solution if imaging at a

liquid-solid interface. To accommodate these factors, the background signal is often subtracted by creating surface patterns with testing regions and reference regions. The testing regions bind to target molecules while the reference regions do not. However, this approach is intrinsically hampered as it introduces heterogeneities in the surface that can lead to complex adsorption processes. Moreover, it is difficult to ensure that the reference regions can fully prevent the molecule binding. The current configuration has the potential to enable a novel approach for fluorescent molecule detection and sensor surface design. While chemically isotropic throughout the entire substrate (i.e., identical adsorption isotherms), the polymer area with the optimal thickness can lead to the maximum enhancement factor and can serve as the testing region. For comparison, a surface area with a film thickness conducive to full fluorescence quenching can act as the reference region. In this design, any signal from the reference region would only originate from the imaging environment or software artifact but not the surface immobilized molecules, and thus can be subtracted. This way, we are able to achieve maximum signal from the testing regions and minimum signals from the reference region.

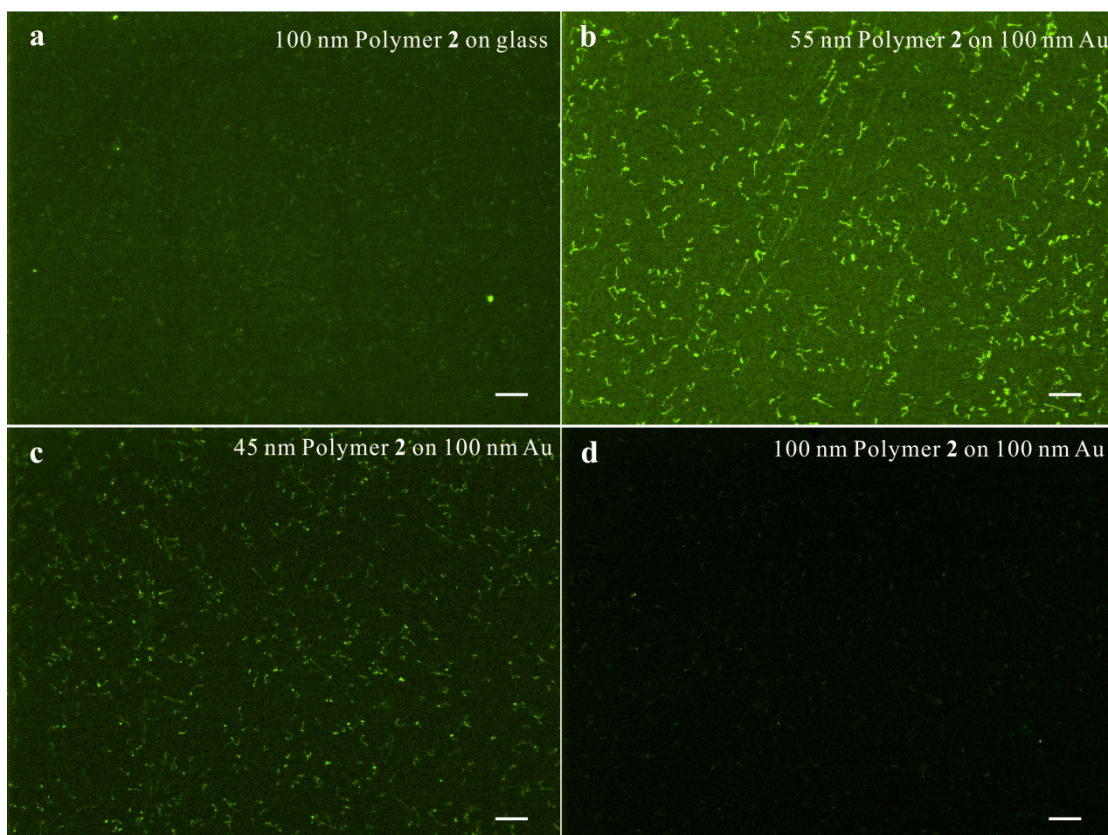


Figure 3.7 Lambda DNA stained with SYBR gold adsorbed and condensed on polymer **2** (with amine group) coated on different substrates with different thicknesses. All the samples were incubated in the DNA solution (50ng/ml) for 30 min followed by thorough rinsing. All scale bars represent 10 μ m.

Finally, we wanted to demonstrate the utility of the fluorescence amplifying substrates for single-molecule studies. We selected lambda-DNA stained with SYBR Gold, as shown in Figure 3.7. Lambda-DNA is a large double-strand DNA molecule with 2 nm diameter and 16 μ m contour length.³⁰ SYBR Gold is bright when bound to nuclear acids and has a good quantum yield of ~ 0.6 .³¹ Here we selected the polymer **2** coating as the spacer layer because it is functionalized with amino groups. Organosilanes with the amino groups such as 3-aminopropyl-triethoxysilanes (APTES) are commonly used to treat mica/glass surface to immobilize and condense DNA molecules, which facilitates AFM or fluorescence imaging.³² Polymer **2**

functionalized with amine has similar interaction with DNA compared to the APTES treated glass. In water solution, the positively charged amino groups interact with the negatively charged phosphate groups on the DNA backbone, and thus induce DNA immobilization and condensation.³³ On polymer coatings without the amine functional group, we could not see the single DNA molecules as shown in Figure 3.7 given the same treatment. After optimizing the polymer **2** spacer layer thickness, we found that 55 nm polymer **2** gives the maximum fluorescence enhancement for the immobilized SYBR gold stained lambda DNA. The enhancement factor is 3-fold compared to the DNA immobilized on 100 nm polymer **2** coated glass. The individual DNA molecules can be much better seen in Figure 3.7b with MEF than in Figure 3.7a. Figure 3.7c and Figure 3.7d with two different polymer **2** thicknesses (45 nm and 100 nm) on gold are shown for comparison purpose. Note that the amine functionalized polymer **2** coating has its own auto-fluorescence. Its intensity also oscillated with the polymer **2** thicknesses on gold. This suggests that for future study we can take advantage of the auto-fluorescence from some biomolecules/cells and try label-free fluorescence enhancement using our established method in this study.

3.4 Summary and Outlook

By using nanometer-thick reactive CVD polymer coatings as the spacer layers for MEF detection, we were able to optimize the fluorescence intensity amplification. We show that the thickness of the polymer coating can modulate the fluorescence signal above a reflective surface between zero and a maximum, that gold substrates

provide a strong enhancement of the fluorescence signal at the maximum, and that patterns of coating thickness can provide direct visualization of the fluorescence intensity change. Polymer patterns with optimized thickness on bare gold surface can be highly useful for boosting the sensitivity of fluorescent molecule detection sensors. Metal enhanced fluorescence can also facilitate single-molecule imaging.

Moreover, lambda- DNA was directly visualized using this approach. It is worth noting that MEF is affected by many factors, such as the metal type, metal particle size and shape, metal layer preparation methods and even the adhesion layer.^{9a, 11} It almost always needs to be optimized on a case-by-case basis. Though in this study we may not have optimized the enhancement effect in every aspect, we have started establishing a viable method to systematically study and use the MEF phenomenon in future applications such as biosensors.

Supplemental Figures

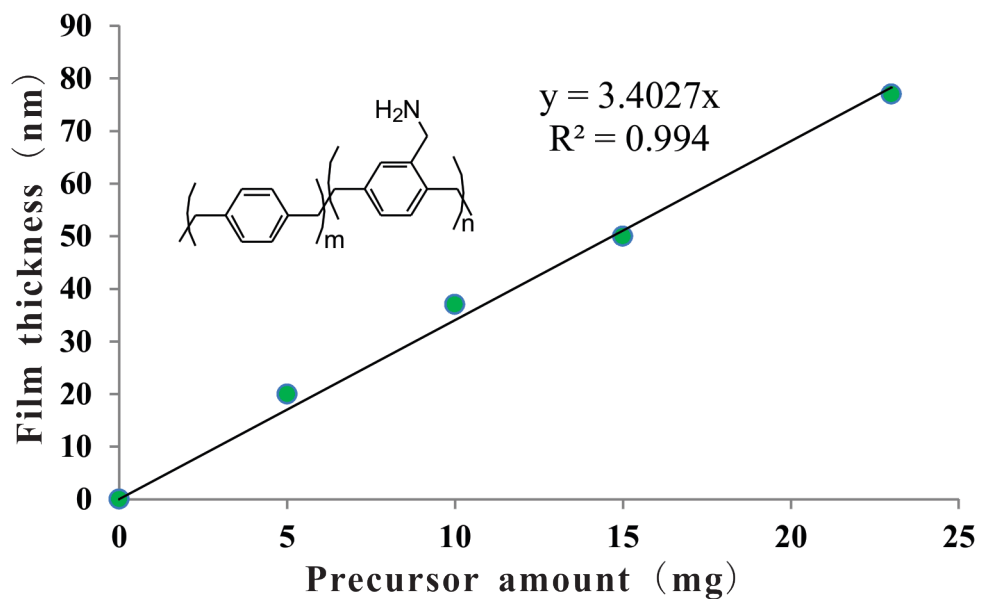
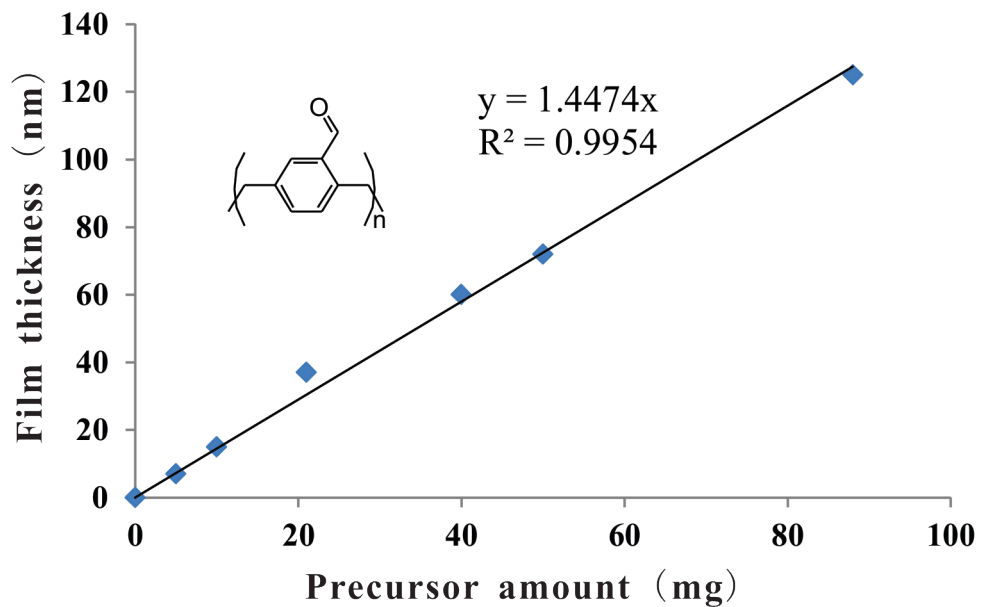


Figure 3.8 Linear relationship of precursor feeding amount and the resulted CVD polymer film thickness for the two different types of polymers used in this study.

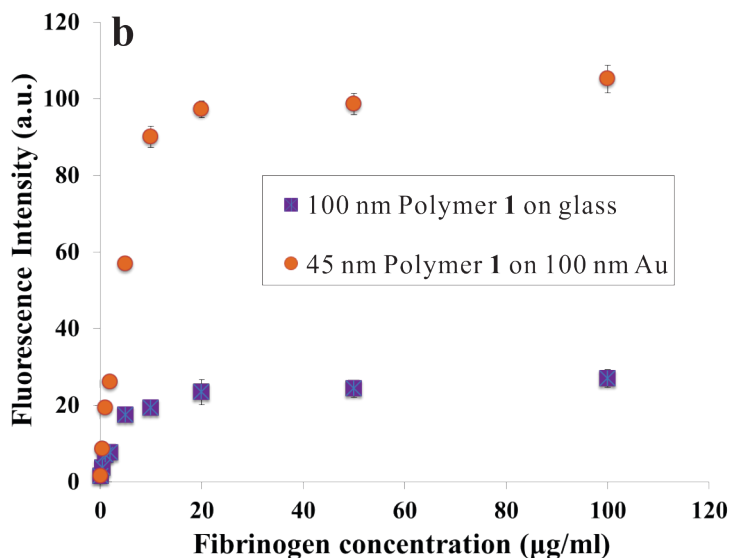


Figure 3.9 Concentration dependence study. Fluorescence intensity of Alexa Fluor 488 conjugated fibrinogen (different concentration from 0.1 to 100 µg/ml in PBS, 5h) adsorbed on 100 nm polymer 1 coated glass or 45nm polymer 1 coated gold.

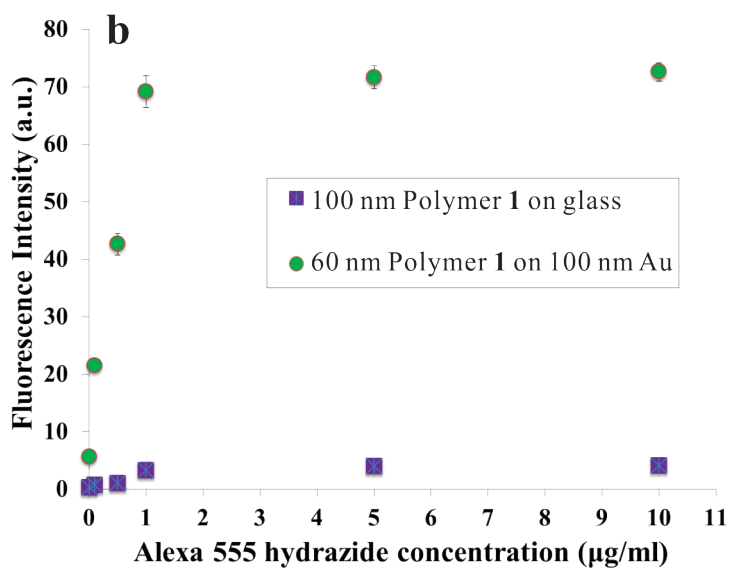


Figure 3.10 Concentration dependence study. Fluorescence Intensity of Alexa Fluor 555 hydrazide (different concentration from 0.01 to 10 µg/ml, pH=5, 12h) covalently immobilized on 100 nm polymer 1 coated glass or 60nm polymer 1 coated gold.

References

1. Aslan, K.; Gryczynski, I.; Malicka, J.; Matveeva, E.; Lakowicz, J. R.; Geddes, C. D., Metal-enhanced fluorescence: an emerging tool in biotechnology. *Curr Opin Biotech* **2005**, *16* (1), 55-62.
2. (a) Wittwer, C. T.; Herrmann, M. G.; Moss, A. A.; Rasmussen, R. P., Continuous fluorescence monitoring of rapid cycle DNA amplification. *Biotechniques* **1997**, *22* (1), 130-&; (b) Konig, K., Multiphoton microscopy in life sciences. *J Microsc-Oxford* **2000**, *200*, 83-104; (c) Nie, S. M.; Chiu, D. T.; Zare, R. N., Probing Individual Molecules with Confocal Fluorescence Microscopy. *Science* **1994**, *266* (5187), 1018-1021.
3. (a) Ratner, B. D.; Bryant, S. J., Biomaterials: Where we have been and where we are going. *Annu Rev Biomed Eng* **2004**, *6*, 41-75; (b) Massoud, T. F.; Gambhir, S. S., Molecular imaging in living subjects: seeing fundamental biological processes in a new light. *Gene Dev* **2003**, *17* (5), 545-580.
4. Roach, S. A.; Rappaport, S. M., But They Are Not Thresholds - a Critical Analysis of the Documentation of Threshold Limit Values. *Am J Ind Med* **1990**, *17* (6), 727-753.
5. (a) Panchuk-Voloshina, N.; Haugland, R. P.; Bishop-Stewart, J.; Bhalgat, M. K.; Millard, P. J.; Mao, F.; Leung, W. Y.; Haugland, R. P., Alexa dyes, a series of new fluorescent dyes that yield exceptionally bright, photostable conjugates. *J Histochem Cytochem* **1999**, *47* (9), 1179-1188; (b) Tuma, R. S.; Beaudet, M. P.; Jin, X. K.; Jones, L. J.; Cheung, C. Y.; Yue, S.; Singer, V. L., Characterization of SYBR gold nucleic acid gel stain: A dye optimized for use with 300-nm ultraviolet transilluminators. *Anal Biochem* **1999**, *268* (2), 278-288; (c) Skonieczny, K.; Ciuciu, A. I.; Nichols, E. M.; Hugues, V.; Blanchard-Desce, M.; Flamigni, L.; Gryko, D. T., Bright, emission tunable fluorescent dyes based on imidazole and pi-expanded imidazole. *J Mater Chem* **2012**, *22* (38), 20649-20664.
6. (a) Michalet, X.; Pinaud, F. F.; Bentolila, L. A.; Tsay, J. M.; Doose, S.; Li, J. J.; Sundaresan, G.; Wu, A. M.; Gambhir, S. S.; Weiss, S., Quantum dots for live cells, in vivo imaging, and diagnostics. *Science* **2005**, *307* (5709), 538-544; (b) Wang, X. Y.; Ren, X. F.; Kahen, K.; Hahn, M. A.; Rajeswaran, M.; Maccagnano-Zacher, S.; Silcox, J.; Cragg, G. E.; Efros, A. L.; Krauss, T. D., Non-blinking semiconductor nanocrystals. *Nature* **2009**, *459* (7247), 686-689.
7. Rurack, K.; Spieles, M., Fluorescence Quantum Yields of a Series of Red and Near-Infrared Dyes Emitting at 600-1000 nm. *Anal Chem* **2011**, *83* (4), 1232-1242.
8. (a) Lambacher, A.; Fromherz, P., Fluorescence interference-contrast microscopy on oxidized silicon using a monomolecular dye layer. *Appl Phys a-Mater* **1996**, *63* (3), 207-216; (b) Kerssemakers, J.; Howard, J.; Hess, H.; Diez, S., The distance that kinesin-1 holds its cargo from the microtubule surface measured by fluorescence interference contrast microscopy. *P Natl Acad Sci USA* **2006**, *103* (43), 15812-15817.
9. (a) Lakowicz, J. R., Radiative decay engineering 5: metal-enhanced fluorescence and plasmon emission. *Anal Biochem* **2005**, *337* (2), 171-194; (b) Geddes, C. D.; Lakowicz, J. R., Metal-enhanced fluorescence. *J Fluoresc* **2002**, *12* (2),

- 121-129; (c) Lakowicz, J. R., Radiative decay engineering: Biophysical and biomedical applications. *Anal Biochem* **2001**, *298* (1), 1-24.
10. Zhang, J.; Lakowicz, J. R., Metal-enhanced fluorescence of an organic fluorophore using gold particles. *Opt Express* **2007**, *15* (5), 2598-2606.
11. Aouani, H.; Wenger, J.; Gerard, D.; Rigneault, H.; Devaux, E.; Ebbesen, T. W.; Mahdavi, F.; Xu, T. J.; Blair, S., Crucial Role of the Adhesion Layer on the Plasmonic Fluorescence Enhancement. *Acs Nano* **2009**, *3* (7), 2043-2048.
12. Lee, K.; Hahn, L. D.; Yuen, W. W.; Vlamakis, H.; Kolter, R.; Mooney, D. J., Metal-Enhanced Fluorescence to Quantify Bacterial Adhesion. *Adv Mater* **2011**, *23* (12), H101-H104.
13. Chance, R. R.; Prock, A.; Silbey, R., Molecular Fluorescence and Energy Transfer Near Interfaces. In *Advances in Chemical Physics*, John Wiley & Sons, Inc.: 2007; pp 1-65.
14. (a) Tarcha, P. J.; DeSaja-Gonzalez, J.; Rodriguez-Llorente, S.; Aroca, R., Surface-enhanced fluorescence on SiO₂-coated silver island films. *Appl Spectrosc* **1999**, *53* (1), 43-48; (b) Renier, A.; Mangeat, T.; Benalia, H.; Elie-Caille, C.; Pieralli, C.; Wacogne, B., Gold/silica thin film for biosensors applications: Metal enhanced fluorescence. *Laser Phys* **2010**, *20* (3), 591-595; (c) Sokolov, K.; Chumanov, G.; Cotton, T. M., Enhancement of molecular fluorescence near the surface of colloidal metal films. *Anal Chem* **1998**, *70* (18), 3898-3905.
15. Aslan, K.; Geddes, C. D., Microwave-accelerated metal-enhanced fluorescence: Platform technology for ultrafast and ultrabright assays. *Anal Chem* **2005**, *77* (24), 8057-8067.
16. Chen, H. Y.; Lahann, J., Designable Biointerfaces Using Vapor-Based Reactive Polymers. *Langmuir* **2011**, *27* (1), 34-48.
17. (a) Elkasabi, Y.; Chen, H. Y.; Lahann, J., Multipotent polymer coatings based on chemical vapor deposition copolymerization. *Adv Mater* **2006**, *18* (12), 1521-+; (b) Elkasabi, Y.; Lahann, J., Vapor-Based Polymer Gradients. *Macromol Rapid Comm* **2009**, *30* (1), 57-63.
18. (a) Chen, H. Y.; Lahann, J., Vapor-assisted micropatterning in replica structures: A solventless approach towards topologically and chemically designable surfaces. *Adv Mater* **2007**, *19* (22), 3801-+; (b) Deng, X. P.; Friedmann, C.; Lahann, J., Bio-orthogonal "Double-Click" Chemistry Based on Multifunctional Coatings. *Angew Chem Int Edit* **2011**, *50* (29), 6522-6526.
19. (a) Kozai, T. D. Y.; Langhals, N. B.; Patel, P. R.; Deng, X. P.; Zhang, H. N.; Smith, K. L.; Lahann, J.; Kotov, N. A.; Kipke, D. R., Ultrasmall implantable composite microelectrodes with bioactive surfaces for chronic neural interfaces. *Nat Mater* **2012**, *11* (12), 1065-1073; (b) Tawfick, S.; Deng, X. P.; Hart, A. J.; Lahann, J., Nanocomposite microstructures with tunable mechanical and chemical properties. *Phys Chem Chem Phys* **2010**, *12* (17), 4446-4451.
20. Jiang, X. W.; Chen, H. Y.; Galvan, G.; Yoshida, M.; Lahann, J., Vapor-based initiator coatings for atom transfer radical polymerization. *Adv Funct Mater* **2008**, *18* (1), 27-35.
21. Bondarenko, L.; Dix, I.; Hinrichs, H.; Hopf, H., Cyclophanes. Part LII: Ethynyl[2.2]paracyclophanes - New building blocks for molecular scaffolding. *Synthesis-Stuttgart* **2004**, (16), 2751-2759.

22. Dix, I.; Hopf, H.; Satyanarayana, T. B. N.; Ernst, L., Preparation and NMR spectra of four isomeric diformyl[2.2]paracyclophanes (cyclophanes 66). *Beilstein J Org Chem* **2010**, *6*, 932-937.
23. Lahann, J., Vapor-based polymer coatings for potential biomedical applications. *Polym Int* **2006**, *55* (12), 1361-1370.
24. Chapman, R. G.; Ostuni, E.; Takayama, S.; Holmlin, R. E.; Yan, L.; Whitesides, G. M., Surveying for surfaces that resist the adsorption of proteins. *J Am Chem Soc* **2000**, *122* (34), 8303-8304.
25. Schasfoort, R. B. M.; Tudos, A. J., *Handbook of Surface Plasmon Resonance*. Royal Society of Chemistry: Cambridge, UK, 2008.
26. Wong, A. P.; Groves, J. T., Topographical imaging of an intermembrane junction by combined fluorescence interference and energy transfer microscopies. *J Am Chem Soc* **2001**, *123* (49), 12414-12415.
27. Schneider, R.; Glaser, T.; Berndt, M.; Diez, S., Using a quartz paraboloid for versatile wide-field TIR microscopy with sub-nanometer localization accuracy. *Opt. Express* **2013**, *21* (3), 3523-3539.
28. (a) Nandivada, H.; Chen, H. Y.; Lahann, J., Vapor-based synthesis of poly [(4-formyl-p-xylylene)-co-(p-xylylene)] and its use for biomimetic surface modifications. *Macromol Rapid Comm* **2005**, *26* (22), 1794-1799; (b) Deng, X. P.; Lahann, J., A Generic Strategy for Co-Presentation of Heparin-Binding Growth Factors Based on CVD Polymerization. *Macromol Rapid Comm* **2012**, *33* (17), 1459-1465.
29. Fluorescence quantum yields (QY) and lifetimes (τ) for Alexa Fluor dyes—Table 1.5. In *Molecular Probes Handbook, A Guide to Fluorescent Probes and Labeling Technologies*, 11th ed.; Johnson, I.; Spence, M. T. Z., Eds. 2010.
30. Southern, E. M.; Anand, R.; Brown, W. R. A.; Fletcher, D. S., A Model for the Separation of Large DNA-Molecules by Crossed-Field Gel-Electrophoresis. *Nucleic Acids Res* **1987**, *15* (15), 5925-5943.
31. Nucleic Acid Detection on Gels, Blots and Arrays—Section 8.4. In *Molecular Probes Handbook, A Guide to Fluorescent Probes and Labeling Technologies*, 11th ed.; Johnson, I.; Spence, M. T. Z., Eds. 2010.
32. (a) Lyubchenko, Y.; Shlyakhtenko, L.; Harrington, R.; Oden, P.; Lindsay, S., Atomic Force Microscopy of Long DNA - Imaging in Air and under Water. *P Natl Acad Sci USA* **1993**, *90* (6), 2137-2140; (b) Jing, J. P.; Reed, J.; Huang, J.; Hu, X. H.; Clarke, V.; Edington, J.; Housman, D.; Anantharaman, T. S.; Huff, E. J.; Mishra, B.; Porter, B.; Shenker, A.; Wolfson, E.; Hiort, C.; Kantor, R.; Aston, C.; Schwartz, D. C., Automated high resolution optical mapping using arrayed, fluid-fixed DNA molecules. *P Natl Acad Sci USA* **1998**, *95* (14), 8046-8051.
33. (a) Feng, Y.; Hoh, J. H., Surface-directed DNA condensation in the absence of soluble multivalent cations. *Nucleic Acids Res* **1998**, *26* (2), 588-593; (b) Hansma, H. G.; Revenko, I.; Kim, K.; Laney, D. E., Atomic force microscopy of long and short double-stranded, single-stranded and triple-stranded nucleic acids. *Nucleic Acids Res* **1996**, *24* (4), 713-720.

CHAPTER 4

Biodegradable CVD Polymer Films

4.1 Introduction

Biodegradable polymers, which can be “degraded through the action of enzymes and/or chemical decomposition associated with living organisms or their secretion products” have a wide range of applications such as packaging, biomedical usage and detergent applications.¹ The main driving forces of developing biodegradable polymers are the environmental concern of non-degradable polymers¹⁻² and the demand for degradable materials in many biomedical applications (surgical fixation, controlled drug delivery, tissue engineering, etc.).^{1,3}

The chemical vapor deposition (CVD) polymerization technique has a lot of distinctive advantages as a coating and surface functionalization platform as discussed in Chapter 1. It has been successfully used in biomedical surface modifications such as biomolecule immobilization (Chapter 2), potential biosensor surface design (Chapter 3) and functional insulating coatings for chronically recording microelectrodes.⁴ However, for certain applications such as modifying tissue engineering scaffold surfaces, completely biodegradable CVD polymer coatings are desired. Successfully synthesized biodegradable CVD polymers can combine the advantages of the chemical vapor deposition and degradability. Previously, other researchers have reported using CVD to synthesize poly(2-

hydroxyethyl methacrylate) (PHEMA) films and studied their degradation.⁵

However, the ester groups of PHEMA are not in the polymer backbone, only in the side chains. It is therefore only partially degradable.

Here we report for the first time a CVD synthesized polymer film with ester groups in the backbone by copolymerizing [2.2]paracyclophanes with cyclic ketene acetals. Cyclic ketene acetals can polymerize with a radical initiator *via* ring-opening polymerization, forming biodegradable polymers with ester groups in the polymer backbone.⁶ They have also been used in copolymerizations with different vinyl monomers in the presence of a radical initiator to impart biodegradability to common vinyl polymers, including photodegradable polymers, water-soluble polymers, thermosensitive polymers, detergent builders and hydrogels.^{6a} In this study, we use the diradicals generated during the traditional [2.2]paracyclophane CVD process as initiators for the cyclic ketene acetal ring-opening polymerization. The diradicals can also serve as copolymer building blocks and contribute to the resulting polymer backbone. (Figure 4.1) Functional groups attached to the [2.2]paracyclophanes can potentially be used to change the polymer properties (hydrophobicity, charge etc.) and to immobilize/deliver desired molecules to guide cell behavior and tissue response. More importantly, the polymer should be able to completely degrade in the end.

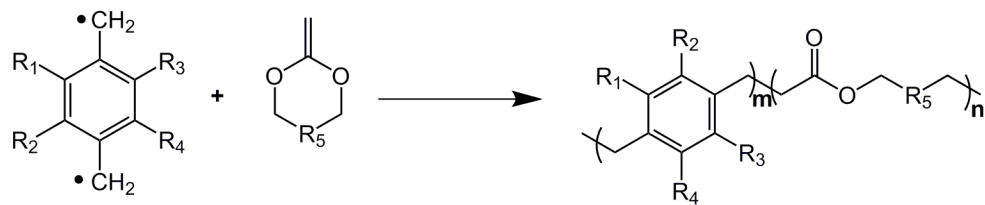


Figure 4.1 Scheme of the biodegradable CVD film synthesis by copolymerizing [2.2]paracyclophanes with cyclic ketene acetals.

4.2 Experimental Section

4.2.1 Synthesis of Cyclic Ketene Acetals (Dr. Christian Friedmann and Domenic Kratzer)

The synthesis methods of different ketene acetals are well documented in the literature.⁷ The most commonly used cyclic ketene acetals in radical ring-opening polymerization studies are summarized in a review by Seema Agarwal published in 2010.^{6b} The ones we synthesized in our lab and used in this study are 5,6-benzo-2-methylene-1,3-dioxepane (Figure 4.2), 2-methylene-1,3-dioxepane (Figure 4.3) and 2-methylene-1,3,6-trioxocane (Figure 4.4).

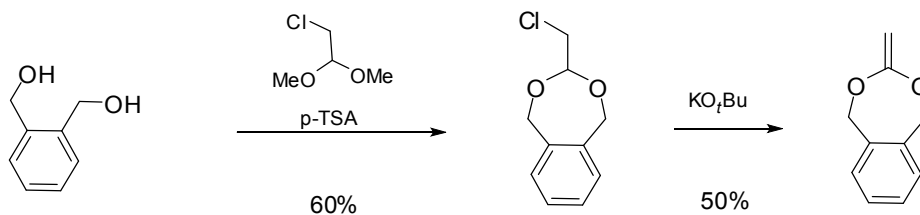


Figure 4.2 Synthesis scheme of 5,6-benzo-2-methylene-1,3-dioxepane.

Synthesis of 2-(chloromethyl)-5,6-benzo-1,3-dioxepane

1,2-Benzendimethanol (16.3 g, 118 mmol), chloroacetaldehyde dimethyl acetal (14.0 mL, 122 mmol) and *p*-toluenesulfonic acid (*p*-TSA) (105 mg, 0.60 mmol) were dissolved in diglyme (33 mL) and the flask was equipped with a short column (10 cm) and a collecting flask for the generated methanol. The mixture was heated to 150 °C and stirred for 24 hours until no more methanol was collected. After cooling to room temperature hexane (100 mL) was added and the precipitated product was filtered off. After washing with hexane (3 x 80 mL) the product was obtained as a white solid (14.2 g, 60%). – **¹H-NMR** (500 MHz, CDCl₃): 7.29–7.20 (m, 4H, aromatic), 5.12 (t, *J* = 5.1 Hz, 1H, OCH), 4.98 (d, *J* = 14.5 Hz, 2H, OCH₂), 4.95 (d, *J* = 14.5 Hz, 2H, OCH₂), 3.63 (d, *J* = 5.1 Hz, 2H, CH₂Cl) ppm. – **¹³C-NMR** (125 MHz, CDCl₃): 138.5, 127.8, 127.5, 106.2, 72.0, 43.9 ppm.

Synthesis of 5,6-benzo-2-methylene-1,3-dioxepane

Under argon, 2-(Chloromethyl)-5,6-benzo-1,3-dioxepane (11.2 g, 56.1 mmol) and potassium *t*-butoxide (KO_{*t*}Bu) (7.74 g, 69.0 mmol) were dissolved in tetrahydrofuran (125 mL) and the mixture was heated to 50 °C. After 72 hours the suspension was cooled to room temperature and the solvent was removed under reduced pressure. Next, diethyl ether (350 mL) was added and the solid was filtered off. After removal of the solvent, the crude product was purified by column chromatography (eluent: hexane/ethyl acetate 4:1 + 5 Vol% triethylamine) to yield the product as a colorless solid (4.51 g, 50%). – **R_f** = 0.70 (hexane/ethyl acetate 4:1 + 5 Vol% triethylamine). – **¹H-NMR** (500 MHz, CDCl₃): 7.29–7.26 (m, 2H, aromatic),

7.13–7.10 (m, 2H, aromatic), 5.09 (s, 4H, OCH₂), 3.75 (s, 2H, CH₂) ppm. – ¹³C-NMR (125 MHz, CDCl₃): 164.2, 135.8, 127.4, 126.2, 72.1, 69.5 ppm.

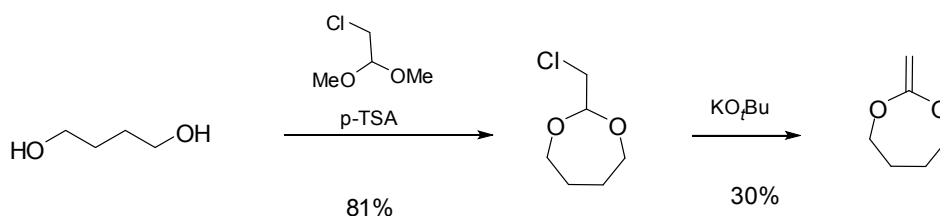


Figure 4.3 Synthesis scheme of 2-methylene-1,3-dioxepane.

Synthesis of 2-chloromethyl-1,3-dioxepane

1,4-Butanediol (17.9 mL, 202 mmol), chloroacetaldehyde dimethyl acetal (23.1 mL, 202 mmol) and *p*-toluenesulfonic acid (100 mg, 0.58 mmol) were dissolved in 1,4-dimethylbenzene (25 mL) and the flask was equipped with a short column (10 cm) and a collecting flask for the generated methanol. The mixture was heated to 130 °C and stirred for 24 hours until no more methanol was collected. After cooling to room temperature, the crude product was purified by distillation (55 mbar, 95 °C) to give 24.9 g (81%) of the title compound as colorless liquid. – ¹H-NMR (500 MHz, CDCl₃): 4.90 (t, *J* = 5.3 Hz, 1H, OCH), 3.97–3.92 (m, 2H, OCH₂), 3.70–3.66 (m, 2H, OCH₂), 3.47 (d, *J* = 5.3 Hz, 2H, CH₂Cl), 1.79–1.67 (m, 4H, OCH₂CH₂) ppm.

Synthesis of 2-methylene-1,3-dioxepane

Under argon, 2-Chloromethyl-1,3-dioxepane (24.0 g, 159 mmol) and KO_tBu (19.6 g, 175 mmol) were dissolved in tetrahydrofuran (175 mL) and the mixture was heated to 50 °C. After 72 hours the suspension was cooled to room temperature

and the solvent was removed under reduced pressure. Next, diethyl ether (350 mL) was added and the solid was filtered off. The organic phase was dried over magnesium sulfate, then the solvent was removed under reduced pressure and the crude product was purified by distillation (140 mbar, 88 °C) to give 5.46 g (30%) of the title compound as colorless liquid. – **¹H-NMR** (500 MHz, CDCl₃): 3.96–3.90 (m, 4H, OCH₂), 3.46 (s, 2H, CH₂), 1.78–1.72 (m, 4H, OCH₂CH₂) ppm.

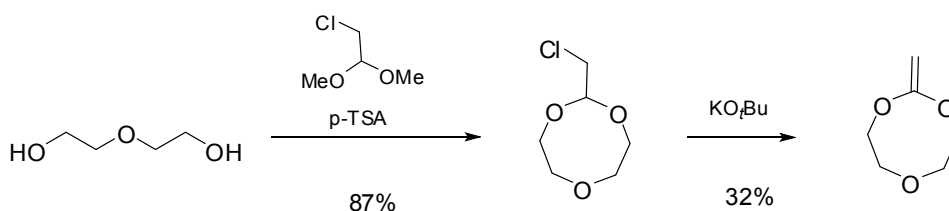


Figure 4.4 Synthesis scheme of 2-methylene-1,3,6-trioxocane.

Synthesis of 2-chloromethyl-1,3,6-trioxocane

Diethylglycol (9.58 mL, 101 mmol), chloroacetaldehyde dimethyl acetal (11.6 mL, 101 mmol) and *p*-toluenesulfonic acid (50 mg, 0.29 mmol) were dissolved in 1,4-dimethylbenzene (12.5 mL) and the flask was equipped with a short column (10 cm) and a collecting flask for the generated methanol. The mixture was heated to 135 °C and stirred for 24 hours until no more methanol was collected. After cooling to room temperature, the crude product was purified by distillation (6 mbar, 80 °C) to give 14.6 g (87%) of the title compound as colorless solid. – **¹H-NMR** (500

MHz, CDCl₃): 4.78 (t, $J = 5.4$ Hz, 1H, OCH), 4.02–3.93 (m, 4H, OCH₂), 3.80–3.62 (m, 4H, OCH₂), 3.47 (d, $J = 5.4$ Hz, 2H, CH₂Cl) ppm.

Synthesis of 2-methylene-1,3,6-trioxocane

Under argon, 2-chloromethyl-1,3,6-trioxocane (12.3 g, 73.8 mmol) and KO_tBu (9.11 g, 81.2 mmol) were dissolved in tetrahydrofuran (70 mL) and the mixture was heated to 50 °C. After 72 hours the suspension was cooled to room temperature and the solvent was removed under reduced pressure. Next, diethyl ether (200 mL) was added and the solid was filtered off. The organic phase was dried over magnesium sulfate, then the solvent was removed under reduced pressure and the crude product was purified by distillation (61 mbar, 85 °C) to give 3.10 g (32%) of the title compound as colorless liquid. – **¹H-NMR** (500 MHz, CDCl₃): 4.08–4.06 (m, 4H, OCH₂), 3.79–3.77 (m, 4H, OCH₂), 3.68 (s, 2H, CH₂) ppm.

4.2.2 CVD Copolymerization of [2.2]Paracyclophanes and Cyclic Ketene Acetals

[2.2]paracyclophane was sublimated at 80 °C in vacuum (0.07 Torr), carried by 20 sccm argon gas through the 510 °C pyrolysis zone and deposited on the cooled substrates (15 °C) in the deposition chamber. The ketene acetal can be fed together with the paracyclophanes or directly into the deposition chamber and controlled by a needle valve. The deposition rate was monitored by an INFICON thin film deposition Quartz Crystal Microbalance (QCM) monitor. The diradicals generated from paracyclophane pyrolysis deposited together with the ketene acetals on the substrates forming copolymer as shown in Figure 4.1.

4.2.3 Surface Characterization and Degradation Progress Tracking

Fourier transform infrared spectroscopy (FTIR) and ellipsometry were used to monitor the film degradation process. FTIR spectra of the CVD polymer films were recorded on a Nicolet 6700 spectrometer with the grazing angle accessory (Smart SAGA) with a 80° fixed angle of incidence. Thicknesses were measured on gold coated silicon substrates by Imaging Spectroscopic Ellipsometer (Accurion, Nanofilm EP³-SE). Ellipsometric parameters were fitted using Cauchy model.

4.2.4 Degradation Condition

The CVD film deposited on gold coated silicon substrates were used in the degradation experiments so that the FTIR and ellipsometry can be used to conveniently check the degradation progress. To speed up the degradation process, 5mM KOH isopropanol solution was used. 0.1 M NaHCO₃ aqueous solution was also used as a more mild condition in some experiments.

4.3 Results and Discussion

We have successfully copolymerized the [2.2]paracyclophane and 5,6-benzo-2-methylene-1,3-dioxepane (BMDO) (Figure 4.5) and totally degraded the copolymer in 5mM KOH in isopropanol within 12 days as shown in the FTIR (Figure 4.6) and ellipsometry (Figure 4.7) measurements.

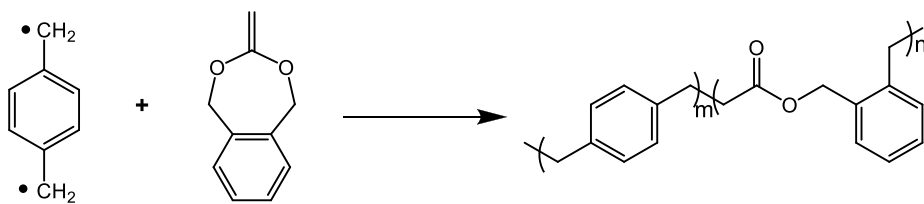


Figure 4.5 Copolymerization of [2.2]paracyclophane and 5,6-benzo-2-methylene-1,3-dioepane. The degrading copolymer shown in Figure 4.6 and Figure 4.7 had an initial feeding ratio of [2.2]paracyclophane : 5,6-benzo-2-methylene-1,3-dioepane = 1 : 2.

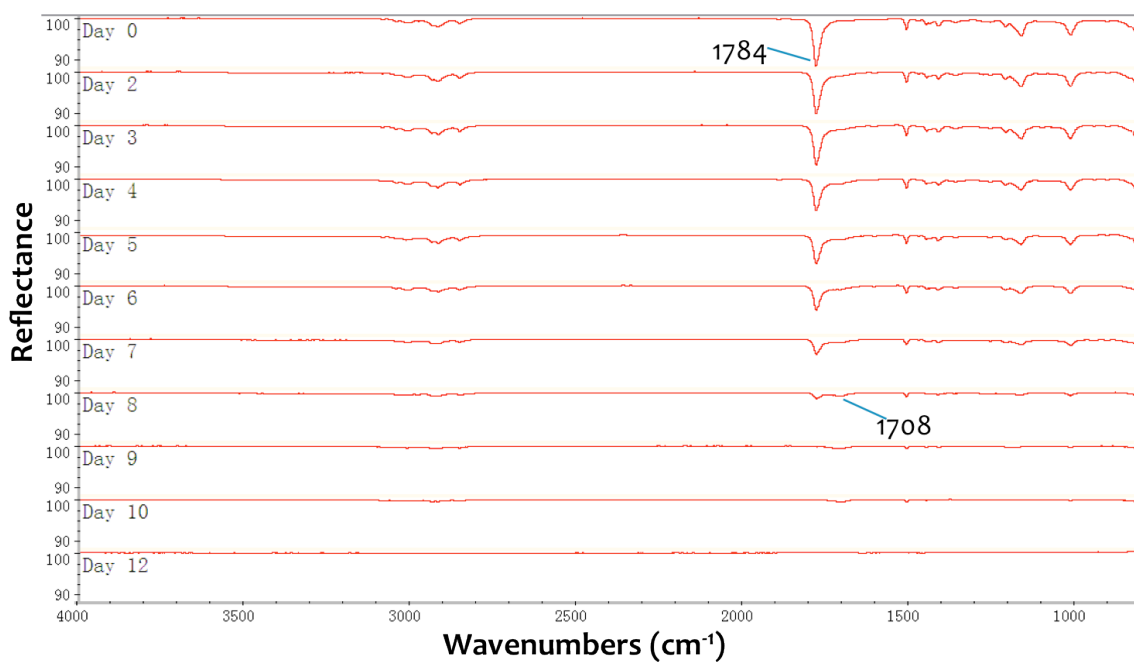


Figure 4.6 FTIR spectra for the degradation process of the [2.2]paracyclophane and 5,6-benzo-2-methylene-1,3-dioepane copolymer in 5mM KOH isopropanol solution.

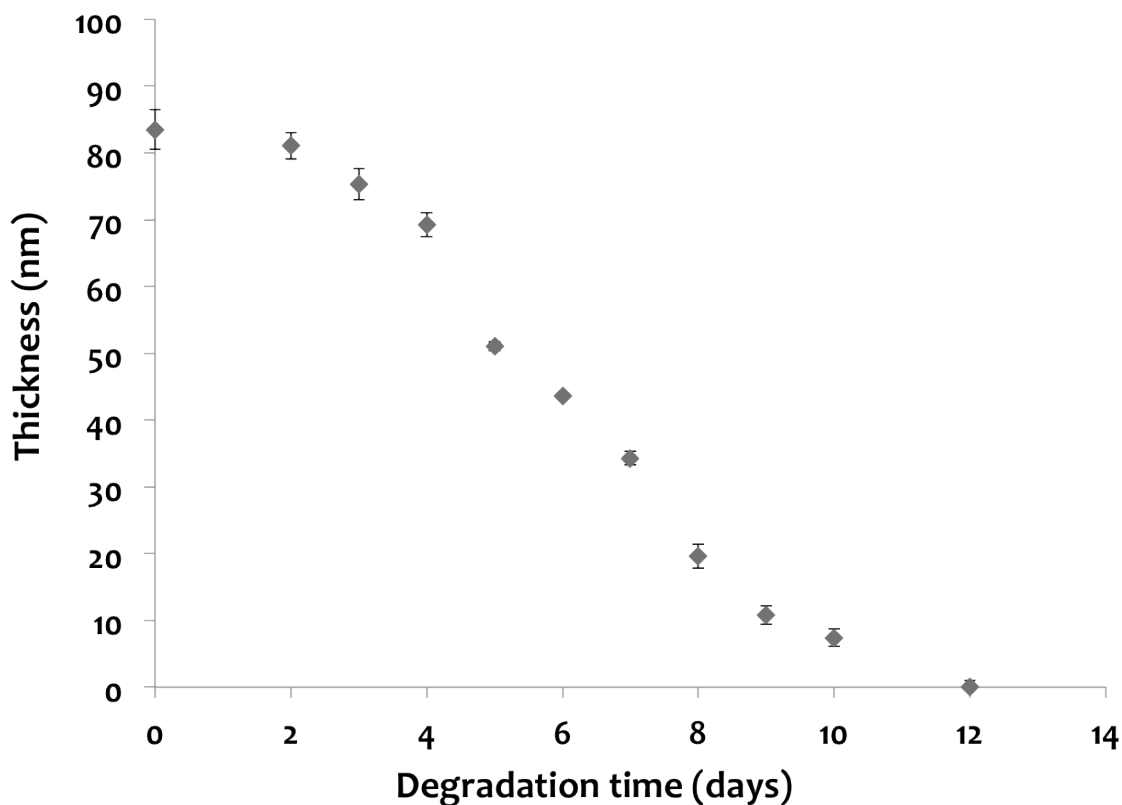


Figure 4.7 Thickness change measured by ellipsometry during the degradation process of the [2.2]paracyclophane and 5,6-benzo-2-methylene-1,3-dioxepane copolymer in 5mM KOH isopropanol solution.

The IR spectra in Figure 4.6 shows that the CVD polymer film was indeed the target copolymer structure shown in Figure 4.5. The IR spectrum of the as-deposited film (spectrum for Day 0) shows the characteristic peaks from both the poly-*p*-xylene block (823, 1513, 2856, 3006, 3048 cm^{-1}) and the ester group (1784, 1168, 1020 cm^{-1}) from the cyclic ketene acetal ring opening. According to the literature,^{6b} 5,6-benzo-2-methylene-1,3-dioxepane (BMDO) can generate ring-opened radicals with increased stability and the increase in steric hindrance to direct non-ring-opened can promote the extent of free-radical ring-opening. BMDO has been successfully copolymerized with styrene,⁹ methyl methacrylate,¹⁰ N-

isopropylacrylamide,¹¹ 2-(2-methoxyethoxy)ethyl methacrylate (MEO₂MA) and oligo(ethylene glycol) methacrylate (OEGMA) with quantitative radical ring-opening.¹² The CVD generated copolymer was intact after common organic solvents wash such as acetone and chloroform, indicating the copolymer has relatively high molecular weight. There was no change to the polymer film after the scotch tape adhesion test, showing good adhesion on the gold-coated silicon substrates.⁸

In 5mM KOH isopropanol solution, the IR peak (1784 cm⁻¹) for ester groups diminished gradually over time along with all other peaks, indicating that the polymer was indeed degrading. A small peak for the carboxylic acid group at 1708 cm⁻¹ appeared during the degradation process. This demonstrates that the degradation mechanism is hydrolysis of the ester groups. The thickness changes in Figure 4.7 further confirmed the degradation, showing that the film thickness decreased gradually overtime from 84 nm on Day 0 to zero on Day 12. Both IR and ellipsometry data demonstrates that the successfully synthesized CVD copolymer film can be completely degraded and it appears to be a surface erosion process.¹³ Compared to bulk erosion, surface erosion is more difficult to achieve but desirable and essential in some biomedical applications such as drug delivery.¹³

So far, the degradable polymer we synthesized can be totally degraded in 5mM KOH isopropanol solution but is not yet 100% degradable under mild conditions in an aqueous solution.

4.4 Conclusion and Future work

Although not being able to totally degrade the polymer in mild aqueous solution yet, the results we collected to date have demonstrated that the cyclic ketene acetal ring-opening polymerization mechanism can be successfully used in the CVD polymerization process. The resulted degradable polymer films with ester groups in the polymer backbone can be completely degraded.

In the future, we need to improve the CVD process control to synthesize a polymer that can be completely degraded in aqueous solutions with a relatively mild pH. Enzyme degradation such as lipase degradation of the polymer can also be tested.¹⁴ Possible methods to achieve complete degradation under mild conditions include improving the polymer film hydrophilicity and lowering the polymer glass transition temperature. Lots of factors during the polymer synthesis could affect the final polymer structure and degradation rate such as CVD deposition rate and reaction temperature.¹⁵ If the deposited film does not have the predicted polymer structure, then side reactions need to be taken into account. Possible side reactions include new cyclization and polymer propagation without the ring-opening.^{6b, 15} In the future, functionalized [2.2]paracyclophanes can be introduced into the copolymerization, not only for introducing the functional groups to anchor biomolecules, but also for changing the polymer properties such as hydrophilicity. Other cyclic ketene acetal molecules may be better for degradation than the 5,6-benzo-2-methylene-1,3-dioxepane we tried in this study. It is also worth noting that thicker film deposition can help with a lot of the analysis of the degradable polymers such as molecular weight, polydispersities, thermal analysis, degradation

products/fragments analysis. Last but not least, extensive biocompatibility tests have to be done before using the newly synthesized degradable CVD film for biomedical applications.

References

1. Amass, W.; Amass, A.; Tighe, B., A review of biodegradable polymers: uses, current developments in the synthesis and characterization of biodegradable polyesters, blends of biodegradable polymers and recent advances in biodegradation studies. *Polym Int* **1998**, *47* (2), 89-144.
2. Gross, R. A.; Kalra, B., Biodegradable polymers for the environment. *Science* **2002**, *297* (5582), 803-807.
3. Freed, L. E.; Vunjaknovakovic, G.; Biron, R. J.; Eagles, D. B.; Lesnoy, D. C.; Barlow, S. K.; Langer, R., Biodegradable Polymer Scaffolds for Tissue Engineering. *Bio-Technol* **1994**, *12* (7), 689-693.
4. Kozai, T. D. Y.; Langhals, N. B.; Patel, P. R.; Deng, X. P.; Zhang, H. N.; Smith, K. L.; Lahann, J.; Kotov, N. A.; Kipke, D. R., Ultrasmall implantable composite microelectrodes with bioactive surfaces for chronic neural interfaces. *Nat Mater* **2012**, *11* (12), 1065-1073.
5. Pfluger, C. A.; Carrier, R. L.; Sun, B.; Ziemer, K. S.; Burkey, D. D., Cross-Linking and Degradation Properties of Plasma Enhanced Chemical Vapor Deposited Poly(2-hydroxyethyl methacrylate). *Macromol Rapid Comm* **2009**, *30* (2), 126-132.
6. (a) Hiraguri, Y.; Tokiwa, Y., Syntheses of Biodegradable Functional Polymers by Radical Ring-Opening Polymerization of 2-Methylene-1,3,6-trioxocane. *J Polym Environ* **2010**, *18* (2), 116-121; (b) Agarwal, S., Chemistry, chances and limitations of the radical ring-opening polymerization of cyclic ketene acetals for the synthesis of degradable polyesters. *Polym Chem-Uk* **2010**, *1* (7), 953-964.
7. (a) Bailey, W. J.; Ni, Z.; Wu, S. R., Synthesis of Poly-Epsilon-Caprolactone Via a Free-Radical Mechanism - Free-Radical Ring-Opening Polymerization of 2-Methylene-1,3-Dioxepane. *J Polym Sci Pol Chem* **1982**, *20* (11), 3021-3030; (b) Bailey, W. J.; Wu, S. R.; Ni, Z., Synthesis and Free-Radical Ring-Opening Polymerization of 2-Methylene-4-Phenyl-1,3-Dioxolane. *Makromol Chem* **1982**, *183* (8), 1913-1920; (c) Bailey, W. J.; Ni, Z.; Wu, S. R., Free-Radical Ring-Opening Polymerization of 4,7-Dimethyl-2-Methylene-1,3-Dioxepane and "5,6-Benzo-2-Methylene-1,3-Dioxepane. *Macromolecules* **1982**, *15* (3), 711-714; (d) Yako, N.; Endo, T., Syntheses and radical ring-opening polymerization of cyclic keten acetals. *Polym. Prepr. Jpn* **1985**, *34*, 154.
8. Lahann, J., Vapor-based polymer coatings for potential biomedical applications. *Polym Int* **2006**, *55* (12), 1361-1370.

9. Wickel, H.; Agarwal, S., Synthesis and characterization of copolymers of 5,6-benzo-2-methylene-1,3-dioxepane and styrene. *Macromolecules* **2003**, *36* (16), 6152-6159.
10. Wickel, H.; Agarwal, S.; Greiner, A., Homopolymers and random copolymers of 5,6-benzo-2-methylene-1,3-dioxepane and methyl methacrylate: Structural characterization using 1D and 2D NMR. *Macromolecules* **2003**, *36* (7), 2397-2403.
11. Ren, L. Q.; Agarwal, S., Synthesis, characterization, and properties evaluation of poly[(N-isopropylacrylamide)-co-ester]s. *Macromol Chem Phys* **2007**, *208* (3), 245-253.
12. Lutz, J. F.; Andrieu, J.; Uzgun, S.; Rudolph, C.; Agarwal, S., Biocompatible, thermoresponsive, and biodegradable: Simple preparation of "all-in-one" biorelevant polymers. *Macromolecules* **2007**, *40* (24), 8540-8543.
13. (a) Tamada, J. A.; Langer, R., Erosion Kinetics of Hydrolytically Degradable Polymers. *P Natl Acad Sci USA* **1993**, *90* (2), 552-556; (b) Gopferich, A., Mechanisms of polymer degradation and erosion. *Biomaterials* **1996**, *17* (2), 103-114; (c) von Burkersroda, F.; Schedl, L.; Gopferich, A., Why degradable polymers undergo surface erosion or bulk erosion. *Biomaterials* **2002**, *23* (21), 4221-31.
14. Hiraguri, Y.; Tokiwa, Y., Synthesis of Copolymers Composed of 2-Methylene-1,3,6-Trioxocane and Vinyl Monomers and Their Enzymatic Degradation. *J Polym Sci Pol Chem* **1993**, *31* (12), 3159-3161.
15. Plikk, P.; Tyson, T.; Finne-Wistrand, A.; Albertsson, A. C., Mapping the Characteristics of the Radical Ring-Opening Polymerization of a Cyclic Ketene Acetal Towards the Creation of a Functionalized Polyester. *J Polym Sci Pol Chem* **2009**, *47* (18), 4587-4601.

CHAPTER 5

Applications of CVD Polymer Coatings on Complex Structures and Integrated Devices

Substrate independence is a prominent feature of the CVD polymerization coating process.¹ We have previously used it for many applications such as flat surface² or 3D surface micro-patterning,³ nano-patterning⁴ and cell culture scaffold coating.⁵ This chapter includes two new applications, one in carbon nanotube/polymer nanocomposite⁶ and one in ultrasmall implantable composite microelectrodes.⁷ These two applications demonstrate the use of functional PPXs coatings in integrated systems, showing their effects not only on surface chemistries but also on mechanical and electrical properties of the integrated systems. Due to the higher cost of the CVD process compared to other coating methods such as spraying, spin coating and dip coating,⁸ it is especially suitable for micro- and nano-devices which require precision production. This is an important reason to emphasize “easy integration with micro- and nano-fabrications” in Chapter 1. More integration studies of the functionalized PPXs in micro- and nano- devices should promote more usage and commercialization of this powerful reactive coating platform.

5.1 Nanocomposite Microstructures with Tunable Mechanical and Chemical Properties

This chapter section has been adapted from of the following published articles with minor modifications:

S. Tawfick, X. Deng, A. J. Hart, J. Lahann. Nanocomposite microstructures with tunable mechanical and chemical properties. *Physical Chemistry Chemical Physics*. 2010, 12, 4446–4451. Reproduced by permission of the PCCP Owner Societies. DOI: 10.1039/C000304M

<http://pubs.rsc.org/en/Content/ArticleLanding/2010/CP/c000304m>

Note: For the study reported in this chapter section, Dr. S. Tawfick and Prof. A. J. Hart carried out the carbon nanotube growth, SEM imaging, mechanical test and analysis. X. Deng and Prof. J. Lahann performed the CVD polymer coating, surface characterizations (IR, XPS, ellipsometry), fluorescence imaging and analysis. All authors wrote the original paper together.

5.1.1 Introduction

Carbon nanotubes (CNTs) are under investigation for myriad applications including reinforced composite materials, transparent conductors, microelectronic interconnections, battery and fuel cell electrodes, artificial muscles, and filtration membranes.⁹ The enthusiasm surrounding CNTs is motivated by their outstanding mechanical, electrical, thermal, chemical, and optical properties.¹⁰ Specifically, individual CNTs have stiffness and strength exceeding steel, and exhibit high strains to failure along with fully recoverable buckling behavior.¹¹ Furthermore, CNTs can be chemically modified by a diverse set of covalent and non-covalent methods, which, in turn, facilitates controlled attachment of polymers and biomolecules to their surfaces, as well as manipulation of their electronic structure.¹² The unique combination of mechanical and chemical properties makes CNTs particularly attractive building blocks for new materials for biomedical applications including neural recording electrodes,¹³ catheters,¹⁴ biochemical sensors,¹⁵ dry adhesives,¹⁶ and hierarchically textured coatings.¹⁷

When CNTs are grown on a substrate by chemical vapor deposition (CVD), they can form vertically aligned “forests” that exhibit anisotropic properties due to the preferential orientation of the CNTs, which is typically perpendicular to the substrate.¹⁸ Many recent studies have demonstrated that CNT forests can be grown over large areas on substrates including silicon wafers,¹⁹ metal foils,²⁰ and advanced fibers.²¹ Importantly, the diameter and areal density of CNTs within a forest can be tuned according to the preparation and/or pre-treatment of the catalyst,²² which controls the mechanical properties and effective surface area of the forest.²³ Thus,

nanoscale control parameters can be combined with processing techniques including patterning of the catalyst, mechanical rolling,²⁴ solvent annealing,²⁵ and etching. These technologies have created diverse geometries of CNTs having controlled orientation and placement over large areas.

In principle, the introduction of additional materials in the void space between CNTs can result in mechanical stabilization and allows for further tuning of the CNT forest properties. However, only a few methods have been used to create such CNT composite structures so far. These methods are polymer infiltration due to capillary effects^{23, 26} and vapor-based deposition processes.^{17, 27} While these methods have been successful in altering the mechanical properties of CNT forests, they typically fall short in providing simple tunability of mechanical stiffness, and do not provide chemical groups for subsequent surface modification. The latter, however, is vital to tailoring the functionality of the CNT structures for biological, chemical, and electrical transduction.

We have previously developed a CVD polymerization technology that allows for deposition of a wide range of different reactive coatings,²⁸ both on simple²⁹ and complex substrates.^{3, 30} These reactive coatings share the same polymer main chain, poly-*p*-xylylene, but differ in the nature of their substituents, which can be presented on aromatic²⁸ or aliphatic³¹ parts of the polymer. In the past, these reactive coatings have been instrumental in immobilizing a number of different entities including proteins,³² peptides,³³ DNA,³⁴ and quantum dots.³⁵ Furthermore, the fundamental ability of reactive coatings to penetrate micro- and nanoscale structures has been previously established.³⁶

Here, we report on a novel process (Figure 5.1) that comprises: (i) spatially controlled CVD of CNT forests; and (ii) reinforcement and functionalization using poly[4-trifluoroacetyl-*p*-xylylene-*co-p*-xylylene] made via CVD polymerization. This simple process enables preparation of a wide range of complex CNT/polymer microstructures with multi-scale texture, tunable mechanical properties and innate chemical reactivity.

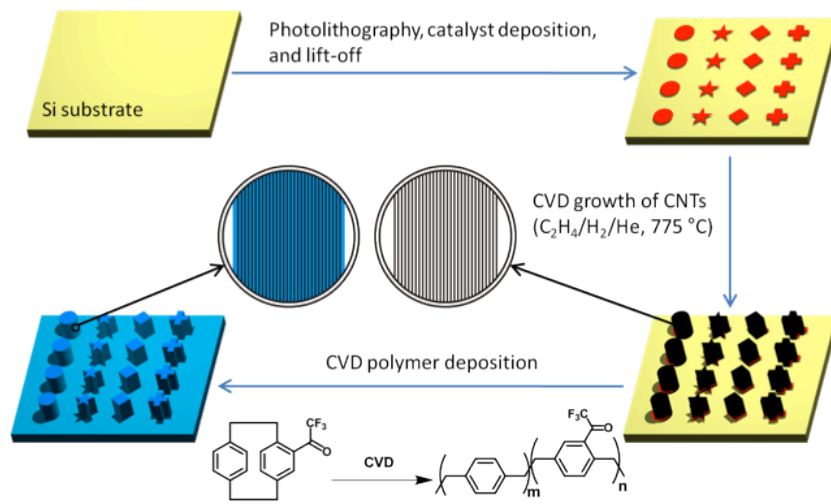


Figure 5.1 Two-stage CVD process for synthesis of functionalized polymer-coated CNT microstructure arrays.

5.1.2 Experimental Section

CNT Growth (Sameh Tawfick)

CNT forest microstructures are grown on thermally-oxidized (100) silicon wafers, on which a supported catalyst layer of 1/10 nm Fe/Al₂O₃ is deposited by e-beam evaporation, as described in a previous publication.³⁷ The catalyst layer is patterned to specify the cross-sectional shapes of the microstructures. Catalyst patterning is achieved by photolithography (SPR 220 photoresist) prior to catalyst

deposition and lift-off (by ultrasonic agitation in acetone) after catalyst deposition. After catalyst patterning, CNT growth is performed in a horizontal tube furnace (22 mm inner diameter, 300 mm heated length) at atmospheric pressure with flows of 100/100/400 sccm C₂H₄/H₂/He, at 775 °C. During the initial stage of growth, the CNTs crowd and self-align perpendicular to the substrate, and then continue growing perpendicular to the substrate. The initial growth rate is typically approximately 100 μm min⁻¹, and the growth time is accordingly chosen to give the desired forest height.

CVD Polymer Coating

The starting material 4-trifluoroacetyl[2.2]paracyclophane was synthesized via Friedel–Crafts acylation of [2.2]paracyclophane.³⁸ A pressure of 0.07 Torr and temperatures of 90–100 °C were employed for the sublimation of the starting material. Then the starting material was transferred in a stream of argon carrier gas (20 sccm) to the pyrolysis zone (670 °C).³⁸ Following pyrolysis, the diradicals were transferred into the deposition chamber, where polymerization occurred.³⁸ While the wall temperature was adjusted to 120 °C, the substrates were cooled to 15 °C to optimize the deposition onto the substrate and the deposition rate was controlled at a constant rate 0.05 nm s⁻¹. Rotation of the sample holder ensured uniform film deposition.

Surface Characterization

XPS data were recorded on an Axis Ultra X-ray photoelectron spectrometer (Kratos Analyticals, UK) equipped with a monochromatized Al Kα X-ray source. All spectra were calibrated with respect to the non-functionalized aliphatic carbon with

a binding energy of 285.0 eV. Theoretical values were calculated based on the structure of the starting material 4-trifluoroacetyl[2.2]paracyclophane. IR spectroscopy was performed on a Nicolet 6700 spectrometer utilizing the grazing angle accessory (Smart SAGA) at a grazing angle of 80°.

Thicknesses were measured at a wavelength of 532 nm using an EP³-SW ellipsometry (Nanofilm Technologie GmbH, Germany). For calibration, nulling experiments were conducted on CVD polymer coated silicon substrates at an incident angle of 70°, and a constant-n (refractive index) and -k (extinction coefficient) value model was used to model the ellipsometric parameters Ψ and δ .

Surface Functionalization

Fluorescein-5-thiosemicarbazide solution (10 mM in ethanol– water 1 : 1 mixture) was allowed to react with the trifluoroacetyl groups of the reactive coating deposited on the CNT structures.

Mechanical Testing (Sameh Tawfick)

Mechanical testing of the CNT forest microstructures was performed using a custom-built microcompression tester, with computer control of displacement and automated measurement of force. The structures were contacted using a stainless steel tip machined to a diameter of \approx 300 nm.

5.1.3 Results and Discussion

Prior to deposition of the reactive coating poly[4-trifluoroacetyl-*p*-xylylene-*co-p*-xylylene] on CNT structures, a library of CNT test structures was grown from lithographically patterned catalyst film (Figure 5.2). Following a previously established photolithographic technique, a thin film of 1/10 nm Fe/Al₂O₃ was patterned on silicon wafers, and vertically aligned CNTs were grown in a C₂H₄/H₂/He atmosphere at 775 °C. After the CNT structures were created, the structures were then modified via CVD polymerization. For a proof-of-concept, we selected poly[4-trifluoroacetyl-*p*-xylylene-*co-p*-xylylene] as the reactive coating because of its documented reactivity towards hydrazides and hydrazines. The process could be similarly applied to reactive coatings with other functional groups, such as active esters, anhydrides, amines, acetylene, or tertiary bromides.²⁸ Polymer deposition followed a modified Gorham process (Figure 5.1),³⁹ where 4-trifluoroacetyl[2.2]paracyclophane was sublimated at a temperature of 90–100 °C and a pressure of 0.07 Torr. Subsequent cleavage of the C–C bonds of the bridge at 670 °C resulted in two different quinodimethanes (monomers). Next, the reactive species were allowed to enter the deposition chamber, where they spontaneously deposited on the CNT structures.

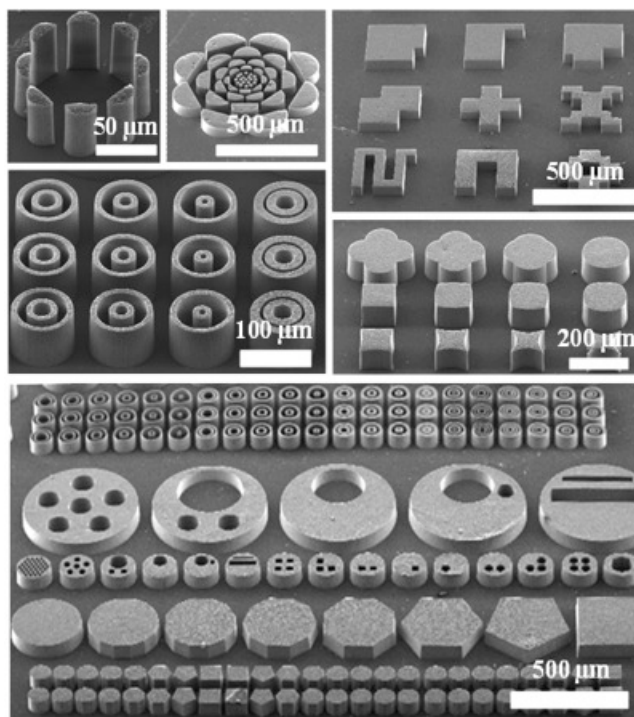


Figure 5.2 SEM images of polymer-coated CNT microstructures, demonstrating diversity of shapes and heterogeneous in-plane scales obtained through parallel processing of CNTs.

Figure 5.2 shows SEM images of a variety of CNT structures after deposition of the reactive coating. The approximate thickness of the polymer coating in this case is 19 nm, and the polymer deposition does not alter the initial topology of the CNT structures. Depending on the deposition time, the polymer thickness varied between 0 and 100 nm, as determined by ellipsometry on Si coupons placed next to the CNT structures. In fact, deposition time is an excellent control parameter for the integration of polymer into the composite structure.

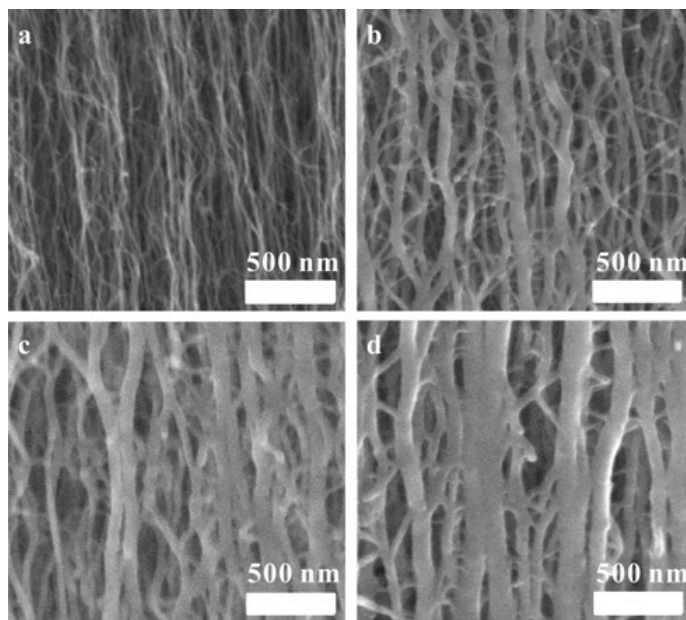


Figure 5.3 SEM images of the sidewalls of the CNT microstructures; (a) after CNT growth, without polymer; (b) after 10 min CVD polymerization (10 nm thickness); (c) after 20 min CVD polymerization (19 nm thickness); (d) after 30 min CVD polymerization (27 nm thickness). The images show that poly[4-trifluoroacetyl-*p*-xylylene-*co-p*-xylylene] conformally coats the CNTs and increases their effective diameter, with thicker polymers at longer deposition times. The magnified images were taken from the side walls of identical microstructures shown in Figure 5.3.

Figure 5.3 compares an uncoated CNT forest (a), with composite structures (b–d) obtained after CVD polymerization for 10, 20 and 30 min, respectively. Based on the SEM images, the respective polymer thicknesses were estimated to be 10, 19, and 27 nm. These figures also show that the polymer has a close to perfect conformity on the individual CNTs and CNT bundles within the forest.

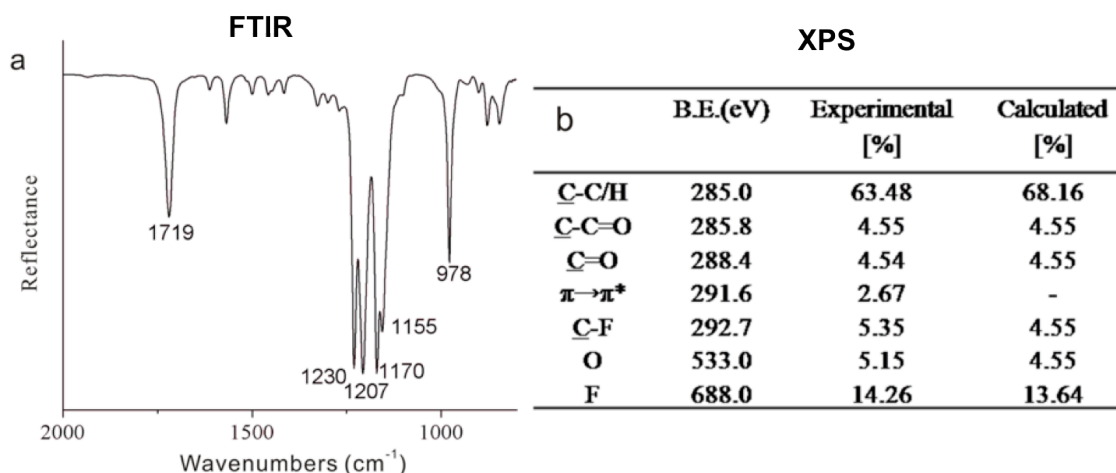


Figure 5.4 Chemical analysis of reactive coating deposited on CNTs; (a) FTIR spectrum of poly[4-trifluoroacetyl-*p*-xylylene-*co-p*-xylylene]; (b) chemical composition of the polymer-coated CNTs determined by XPS.

The chemical composition of poly[4-trifluoroacetyl-*p*-xylylene-*co-p*-xylylene] deposited onto the CNT structures was confirmed by grazing angle Fourier transform infrared (FTIR) spectroscopy to be in accordance with published data.⁴⁰ Specifically, the polymer coatings showed characteristic bands of the C-F stretches from 1230 cm⁻¹ to 1155 cm⁻¹ (Figure 5.4a).⁴¹ In addition, X-ray photoelectron spectroscopy (XPS) was used to confirm the elemental composition of poly[4-trifluoroacetyl-*p*-xylylene-*co-p*-xylylene] after deposition onto CNT structures (Figure 5.4b). The theoretical values, calculated based on the chemical structure of the 4-trifluoroacetyl[2.2]paracyclophane, were in excellent agreement with the experimental findings and confirmed the presence of the reactive coating on the CNT structures. In the light of previous studies that established a good agreement between surface composition obtained by XPS and bulk composition obtained by elemental analysis,³⁸ we decided to continue our investigations into the mechanical

properties of CNT microstructures coated with poly[4-trifluoroacetyl-*p*-xylylene-*co-p*-xylylene].

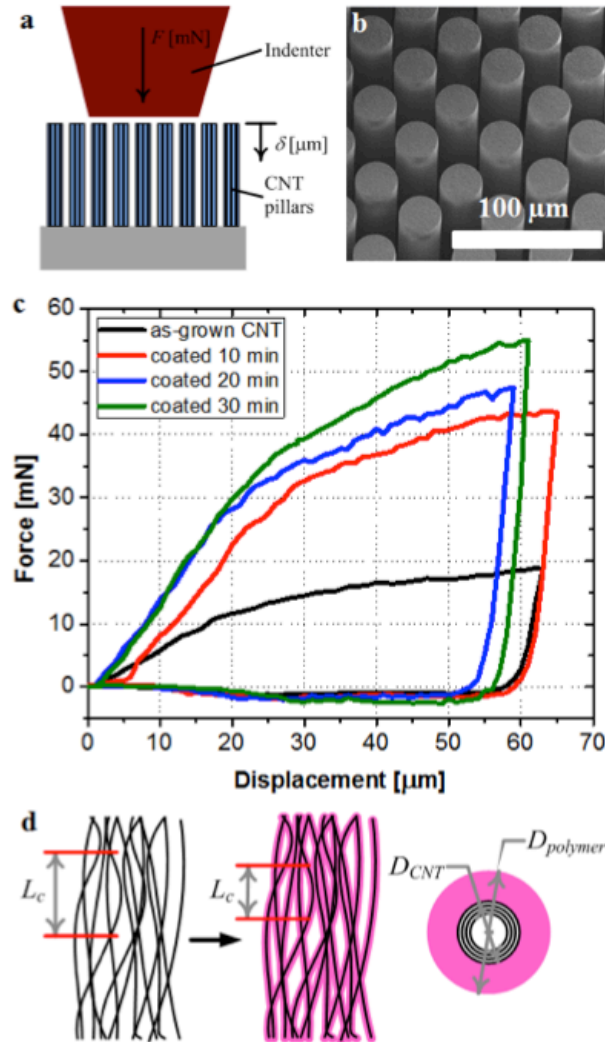


Figure 5.5 Tuning of the mechanical properties of the polymer-CNT microstructures: (a) schematic of test configuration; (b) SEM image of representative microstructure array used for mechanical testing; (c) load-displacement curves, corresponding to data in Table 5.1; (d) schematic of effective length approximation for modelling of mechanical properties.

Table 5.1 Summary of measurements of polymer-coated CNT microstructures, along with parameter estimates calculated by effective elasticity model

Polymer CVD time [min]	Measurements			Model	
	Polymer thickness on flat substrate [nm]	Diameter of polymer-coated CNT [nm]	E [MPa]	(EI) composite [mN/nm ²]	c [μm ⁻³]
0	0	9	36	0.900	6.18 × 10 ⁶
10	38	28	64.5	0.918	1.09 × 10 ⁷
20	70	47	73.1	1.04	1.08 × 10 ⁷
30	100	63	80.15	1.36	9.09 × 10 ⁶

Deposition of poly[4-trifluoroacetyl-*p*-xylylene-*co-p*-xylylene] within CNT forests also facilitates tuning of the mechanical properties of the complex nanocomposite microstructures. Specifically, we wanted to confirm that the Young's modulus of the structures, determined by compression testing, could be designed by selecting the thickness of the polymer layer. Figure 5.5 presents the measurement configuration and results of microcompression tests of arrays of bare CNT pillars, along with arrays coated for 10, 20, and 30 min. For each sample, the elastic modulus of the pillars (E_f) is calculated from the slope of the unloading curve, after loading to the sample to a strain $\approx 35\%$. As expected, polymer coating increases the modulus of the structures, and we can understand the mechanism of mechanical reinforcement using a simple mechanical model.

It has been verified that elastic deformation of CNTs can be modeled using continuum mechanics.^{11, 42} Thus, a CNT can be approximated as a hollow circular beam having flexural rigidity EI , where I is the moment of inertia of its cross-section.

Then, after polymer coating, each CNT is a core–shell composite beam, having the following rigidity:

$$(EI)_c = (EI)_{CNT} + (EI)_{polymer} \quad (1)$$

However, because of the entanglement of individual CNTs and the interaction among them within a forest, estimation of the elastic modulus of forests from the known modulus and dimensions of individual CNTs (*i.e.*, the CNT’s inner diameter, outer diameter and length) remains a challenge. For example, while the mechanical properties of CNT forests have been studied by means of cyclic compression tests; and the elastic modulus was determined, only the critical buckling stress could be theoretically predicted.⁴³

Thus, we must consider how the mechanical behavior of the composite material depends both on the characteristics of the individual CNTs and their coupling. Due to their high aspect ratio and their tortuosity within the forest, individual CNTs are mostly subject to bending, when the forest is compressed. Consequently, the flexural rigidity of the individual CNTs dominates the collective stiffness of a CNT forest. The flexural rigidity is equal to EI , where E is the elastic modulus of the CNT, and I is the second moment of area of the CNT cross-section. Thus, the film stiffness (k_f) can be related to the elastic modulus of the forest (E_f) and the flexural modulus of an individual polymer-coated CNT according to the equations below.

$$k_f = \frac{E_f A_{tip}}{h_f} = c(EI)_c \quad (2)$$

$$c = \frac{n\lambda}{mL_c^3} \quad (3)$$

The constant of proportionality (c) accounts for the geometry, loading, and collective morphology of the individual CNTs. Within eqn (3), λ is a constant and L_c is a characteristic length; both of these parameters depend on the geometry of the individual CNTs and loading conditions. For example, if the CNT forest could be modeled as a number of cantilever beams each subject to a transverse tip force, then $\lambda = 3$, and L_c would be equal to the beam length. For curved beams, $\lambda = 2/\pi$, and L_c is the radius of curvature of the beam.

Using this expression, we model each CNT (extending vertically through the forest) as a number of identical compression springs loaded in series. Consequently, the forest is a number of CNTs loaded in parallel. The constant m accounts for the periodicity of the characteristic length within the forest, which is directly related to the number of identical springs that constitute each CNT. Thus, m is related to the waviness of the individual CNTs, because the amount of contact with other CNTs determines the characteristic “free” length of each spring section. Finally, n represents the number of parallel, load-bearing elements and thus relates to the areal density of the CNT forest (CNTs per cm^2).

Using the measured values of the outer diameter of the polymer-coated CNTs, and a published value ($E_p = 1 \text{ GPa}$)⁴⁴ of the modulus of parylene,⁴² we calculate c for the three composites that were tested. These values, along with the value for uncoated CNTs, are shown in Table 5.1. In the case of the 10 min coating, the increase in the elastic modulus of the forest (80%) cannot be related only to the increase in flexural rigidity (2%). According to the model, the c value increases to

$1.09 \times 10^7 \mu\text{m}^{-3}$, and therefore the polymer connects neighboring CNTs and CNT bundles. Considering that all parameters are constant except for the polymer thickness, we predict that the characteristic CNT length decreases by $\approx 20\%$ due to the increased coupling within the composite.

For the 20 min deposition time, the composite rigidity significantly increases due to the increase in polymer diameter. However, the value of c remains almost unchanged compared to the 10 min sample, indicating that the mechanism of film deformation and the characteristic length remain unchanged. For the 30 min deposition time, the composite modulus of rigidity continues to increase due to the increased diameter. Interestingly, the value of c decreased slightly but remains higher than that for the as-grown CNTs. This may be attributed to inaccuracy in average diameter measurements after polymer coating, owing to the polydisperse collection of individual CNTs and bundles within the forest. We also expect that the diffusion resistance to coating infiltration inside the CNT structures increases with deposition time, as the coating builds up on the outer CNTs and therefore blocks access to the inner regions. Therefore, while highly uniform and conformal coating is observed on the outer surfaces, the change in c may reflect non-uniformity in the coating thickness horizontally throughout the structure. Cross-sectioning the structures using a focused ion beam (FIB) was inconclusive in due to beam-induced damage of the sample, and we are studying this issue in further detail.

Moreover, we note that the loading region stress–strain curve of the nanotubes show two distinct linear trends during loading. The first slope is linear and extends to $\approx 12\text{--}18\%$ where a transition to a smaller slope takes place. This

transition can be attributed to a change in deformation mechanism from compression to collective buckling of the CNTs. In the latter case, the proximity of the individual CNTs induces self-organization of wavelike buckles, as has been observed previously.^{43a}

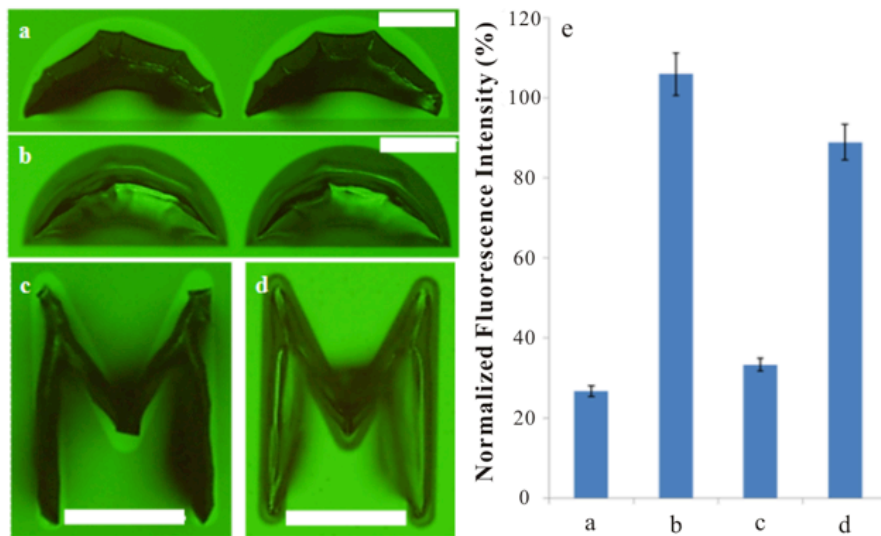


Figure 5.6 Demonstration of selective chemical functionalization of CNT microstructures enabled by the polymer coating: (a, c) CNT structures without polymer coating, with coating and subsequent reaction with a fluorescence probe; (b, d) CNT structures with poly[4-trifluoroacetyl-*p*-xylylene-*co-p*-xylylene] coating and subsequent immobilization of dye coating, exhibiting significant fluorescence enhancement. Structures were densified by infiltration and evaporation of acetone before dye coating to prevent distortion due to capillary forces from the dye solution. The normalized fluorescence intensity (NFI), plotted in (e), is defined as the mean gray value of the CNT structures divided by the mean gray value of flat surface background. Scale bars represent 100 μm .

Finally, to confirm that poly[4-trifluoroacetyl-*p*-xylylene-*co-p*-xylylene] deposited within CNT structures still maintained their chemical reactivity towards binding partners, we used a model ligand, fluorescein-5-thiosemicarbazide, for coupling to poly[4-trifluoroacetyl-*p*-xylylene-*co-p*-xylylene]. Figure 5.6 details the

outcome of this experiment. As anticipated, after immobilization of the fluorescence label, enhanced fluorescence was observed on the CNT structures. Note, that the relatively high background fluorescence of the substrate present before and after reaction with the fluorescence label is due to the autofluorescence of the photoresist used during photolithography (step 1 in Figure 5.1). To quantitatively compare the fluorescence intensity of the CNT structure area, the mean gray values of the CNT structures were measured using ImageJ software. The normalized fluorescence intensity (NFI) was calculated as the mean gray value of the CNT structures divided by the mean gray value of the flat surface (background) surrounding the structures, as shown in Figure 5.6e. The fluorescence intensity of the CNT structures increases by approximately 400% after polymer coating, confirming that deposition of poly[4-trifluoroacetyl-*p*-xylylene-*co-p*-xylylene] imparted chemical functionality to the CNTs.

5.1.4 Conclusion

Spatially controlled growth of CNTs enables the fabrication of a wide range of complex nanocomposite microstructures. Here, we demonstrate that poly[4-trifluoroacetyl-*p*-xylylene-*co-p*-xylylene] made by chemical vapor deposition polymerization can be conformally introduced within CNT microstructures. Polymer infiltration enables simultaneous mechanical reinforcement and chemical functionalization of the CNTs, while retaining their aligned and multiscale texture. We expect that much greater versatility in mechanical and chemical properties can

be achieved by changing the structural characteristics of the CNT forest (*e.g.*, CNT diameter, areal density), or by further tuning the coating properties, structure, and thickness. Based on this initial study, it is very plausible that chemically modified and mechanically reinforced CNT microstructures could play a pivotal role in future development of thin films for energy absorption, materials exhibiting chemical and/or optical transduction of mechanical stimuli, and next-generation biointerfaces.

5.2 Materials and Surface Design of Ultrasmall Implantable Composite

Microelectrodes for Chronic Neural Interfaces

This chapter has been adapted from part of the following published articles with minor modifications:

T. D. Y. Kozai, N. B. Langhals, P. R. Patel, X. Deng, H. Zhang, K. L. Smith, J. Lahann, N. A. Kotov, D. R. Kipke. Ultrasmall implantable composite microelectrodes with bioactive surfaces for chronic neural interfaces. *Nature Materials*. 2012, 11, 1065-1073. doi:10.1038/nmat3468. Reproduced with permission of Nature Publishing Group.

Note: This section mainly focuses on the materials part especially the CVD polymer coatings, the original paper published in Nature Materials is a complete study with neural recording, cell and animal studies. Please refer to the original paper for the neural recording and biological data. I would like to express my appreciation for the chance to collaborate with all the authors of this paper especially Dr. T. D. Y. Kozai.

5.2.1 Introduction

Obtaining selective, high-fidelity, long-lasting readouts of brain activity is a critical technology across basic and applied neuroscience. Since the pioneering work of Strumwasser,⁴⁵ demonstrating the ability to chronically record neural activity using microwires in hibernating squirrels, there has been an ongoing push to improve implantable microelectrode technologies in terms of size, shape, density, recording mode, signal-to-noise ratio (SNR), tissue integration and functional duration.⁴⁶ Today, most implantable neural microelectrodes trace back to the three historical microelectrode technologies: microwires; thin-film planar probes based on silicon or polymer substrates; or bulk micromachined arrays. Although incremental progress has been steady, there are still no definitive solutions for creating stable, long-lasting devices that elicit little or no deleterious tissue responses in the brain.^{46a, 47} As recent advances in the understanding of brain tissue responses come to the forefront of neural engineering,⁴⁸ advances of these technologies are reaching limitations imposed by size, flexibility, strength, biocompatibility and electrical trade-offs of traditional materials such as metals, glass and silicon. To make fundamental advances in microelectrode technologies, it is necessary to bring together a new set of materials to create functional chronic implantable electrodes that are much smaller and more flexible, but sufficiently robust, and at the same time have improved electrical characteristics and bioactive surfaces to control intrinsic biological processes.

Emerging trends and technology in advanced biomaterials⁴⁹ and chronic neural interfaces^{48a, 50} involve bio-inspired exploration of new paradigms to

improve the biocompatibility and lifetime, better tissue integration and maintain neuronal viability. Although carbon-fibre microelectrodes have been extensively used to record extracellular/intracellular neural activity and changes in chemical concentrations, they are insulated in glass capillaries or fused silica tubes, which increase the implanted device's footprint and stiffness⁵¹ and limit its capabilities for chronic *in vivo* single-unit recordings. Studies of the probe/tissue interface suggest that flexible probes may help to minimize perpetual mechanical trauma caused by physiological motion between the probe and the surrounding tissue.^{48e, 52} To this end, polymers have been employed in increasingly flexible probes.⁵³ Furthermore, new fabrication techniques leveraging softer advanced materials have allowed for sophisticated types of probe architecture with subcellular-sized features demonstrating a reduction of the encapsulation response.⁵⁴ However, reduction of recording sites causes an inverse effect of increasing impedance despite its ideal characteristics for isolating single-unit neural activity. Therefore, advanced organic conductive polymers such as poly(3,4-ethylenedioxythiophene) (PEDOT) have been used to improve the recording characteristics of small recording sites over time,⁴⁹ although PEDOT has been shown to cause some degradation from prolonged electrical stimulation.⁵⁵ More recently, functional organic bioactive surface materials have shown promise of improving chronic interfaces in new ways.⁵⁶ The emerging engineering model based on these studies points to innovative composite materials that are specifically designed to fulfill aggressive sets of functional requirements across multiple dimensions that were previously limited by intrinsic size, strength, flexibility, electrical and biocompatibility trade-offs.

Our objective was to fabricate and test an ultrasmall organic electrical microelectrode that has a subcellular cross-sectional dimension, but is flexible, stronger, and has sufficient electrical characteristics for neural recording and advanced bioactive capabilities for controlling intrinsic biological processes. We developed composite materials that are specifically engineered to extend the microelectrode design space to achieve a set of functional requirements for chronic performance that previously were limited by intrinsic size, strength and electrical trade-offs of conventional technologies.

Here, we report the development of an integrated composite electrode consisting of a carbon-fiber core, a poly(*p*-xylylene)-based thin-film coating that acts as a dielectric barrier and that is functionalized to control intrinsic biological processes, and a poly(thiophene)-based recording pad. The resulting implants are an order of magnitude smaller than traditional recording electrodes, and more mechanically compliant with brain tissue. They were found to elicit much reduced chronic reactive tissue responses and enabled single-neuron recording in acute and early chronic experiments in rats. This technology, taking advantage of new composites, makes possible highly selective and stealthy neural interface devices towards realizing long-lasting implants.

5.2.2 Experimental Section

Functional CVD Coatings on Carbon-fibre Microthread Electrodes (MTEs)

One to three individual 7 μm diameter (Cytec Thornel T650, tensile modulus = 234 GPa) carbon fibres were mounted onto a NeuroNexus A16 printed circuit board or a bare stainless-steel wire using silver epoxy (WPI) and baked at 140 $^{\circ}\text{C}$ for 10 min. An $\approx 800\text{-nm}$ -thick poly(*p*-xylylene) insulator layer was then deposited using CVD. One gram of paracyclophane was sublimed at 90 to 110 $^{\circ}\text{C}$ and 0.07 Torr and carried into the pyrolysis chamber by argon at a flow rate of 20 standard cubic centimetres per minute (sccm). After pyrolysis at 670 $^{\circ}\text{C}$, the polymer was deposited on the substrate at 15 $^{\circ}\text{C}$. The deposition rate, according to the quartz-crystal microbalance, was 0.6-1.0 \AA s^{-1} . Next, the surface was functionalized with a $\approx 50\text{ nm}$ thick poly(*p*-xylylene-4-methyl-2-bromoisobutyrate)-*co*-(*p*-xylylene)) layer using CVD. [2.2]paracyclophane-4-methyl 2-bromoisobutyrate was sublimed at 90-110 $^{\circ}\text{C}$ and 0.07 Torr and carried into the pyrolysis chamber by argon at a flow rate of 20 sccm. After pyrolysis at 550 $^{\circ}\text{C}$, the polymer was deposited on the substrate at 15 $^{\circ}\text{C}$ at 0.6-1.0 \AA s^{-1} .

Atom Transfer Radical Polymerization

Poly(ethylene glycol) monomethyl ether methacrylate (PEGMA) was grafted onto the poly(*p*-xylylene) surface by ATRP. Poly(*p*-xylylene-4-methyl-2-bromoisobutyrate)-*co*-(*p*-xylylene)) was used as the initiator for ATRP because of its functional groups.⁵⁷ After deposition of poly(*p*-xylylene-4-methyl-2-bromoisobutyrate)-*co*-(*p*-xylylene)), MTEs were incubated under inert conditions with a degassed aqueous solution of oligo(ethylene glycol) methyl ether

methacrylate, with CuBr/CuBr₂/2,2'-bipyridine as the catalyst. The polymerizations proceeded at room temperature for 4 h. Surface-modified MTEs were thoroughly rinsed after the reaction.

Probe Tip Treatment with PEDOT

Poly(*p*-xylylene)-coated and PEGMA-grafted carbon fibers were cut to a length of 0.3-0.5 cm. For PEDOT deposition, monomer 3,4-ethylenedioxythiophene (EDOT) (Bayer, Germany) was electrochemically polymerized and deposited onto the surface of the electrode sites together with the anions in the solution. Specifically, PEDOT/PSS was electropolymerized from a 0.1 M poly(sodium-*p*-styrenesulfonate) (PSS) (Acros Organics, Morris Plains, NJ) aqueous solution with an EDOT concentration of 0.01 M under galvanostatic conditions. In galvanostatic mode, the current was held at 100 pA.

Electrical Characterization

EIS and CV measurements were made using an Autolab potentiostat PGSTAT12 (Eco Chemie, Utrecht, The Netherlands) with associated frequency response analyzer and general-purpose electrochemical system software (Metrohm, Westbury, NY), respectively. To obtain EIS and CV measurements, each probe was submerged in a PBS solution of 137 mM sodium chloride, 2.7 mM potassium chloride, and 11.9 mM phosphate buffer with a stainless steel rod serving as the counter electrode and a standard Ag|AgCl probe as the reference. Impedance measurements were taken between 10 Hz and 31 kHz at 25 mV_{rms}. CV values were obtained by cycling three times from 0.8 V to -0.6 V at a sweep rate of 1 V/s and averaging the last two cycles. Charge storage capacity (CSC) of each site was

calculated from the full area under the CV curve, scaled by the inverse of the scan rate. After implantation, a distant stainless steel (316-SS grade) bone screw was used as the reference and counter electrode.

Protein Adsorption

Poly(*p*-xylylene)-coated and PEGMA-grafted devices were incubated in FITC-albumin in 2 mg/ml PBS solution for 60 min, then washed in PBS for 30 min.

Immediately after, FITC-albumin was imaged with an Nikon Eclipse 80i in the FITC channel. Biofouling was calculated by measuring the intensity of the probe after adsorption and normalizing it against the background intensity.

SEM Imaging

SEM imaging was carried out on a FEI Quanta 200 3D Focused Ion Beam Workstation (FEI, Hillsboro, OR). Samples were sputter coated with gold prior to imaging.

Microscopic Raman Spectroscopy

The carbon nanotube samples were analyzed using a Bruker SENTERRA Raman system (Bruker Optik GmbH, Ettlingen, Germany) based on an Olympus BX 51 microscope (Olympus Corp., Tokyo, Japan), and an Olympus UIS-2 LMPlanFL N 100x/0.80 objective (Olympus Corp. Tokyo, Japan) with 2 μm resolution used for the lateral and axial directions. The equipped 532 nm laser was chosen for the measurements of the sample surfaces. In order to avoid thermal decomposition of the sample, the laser power was attenuated to 2mW for the analysis. The spectra were recorded in the region from 100 to 4000 cm^{-1} for each sample.

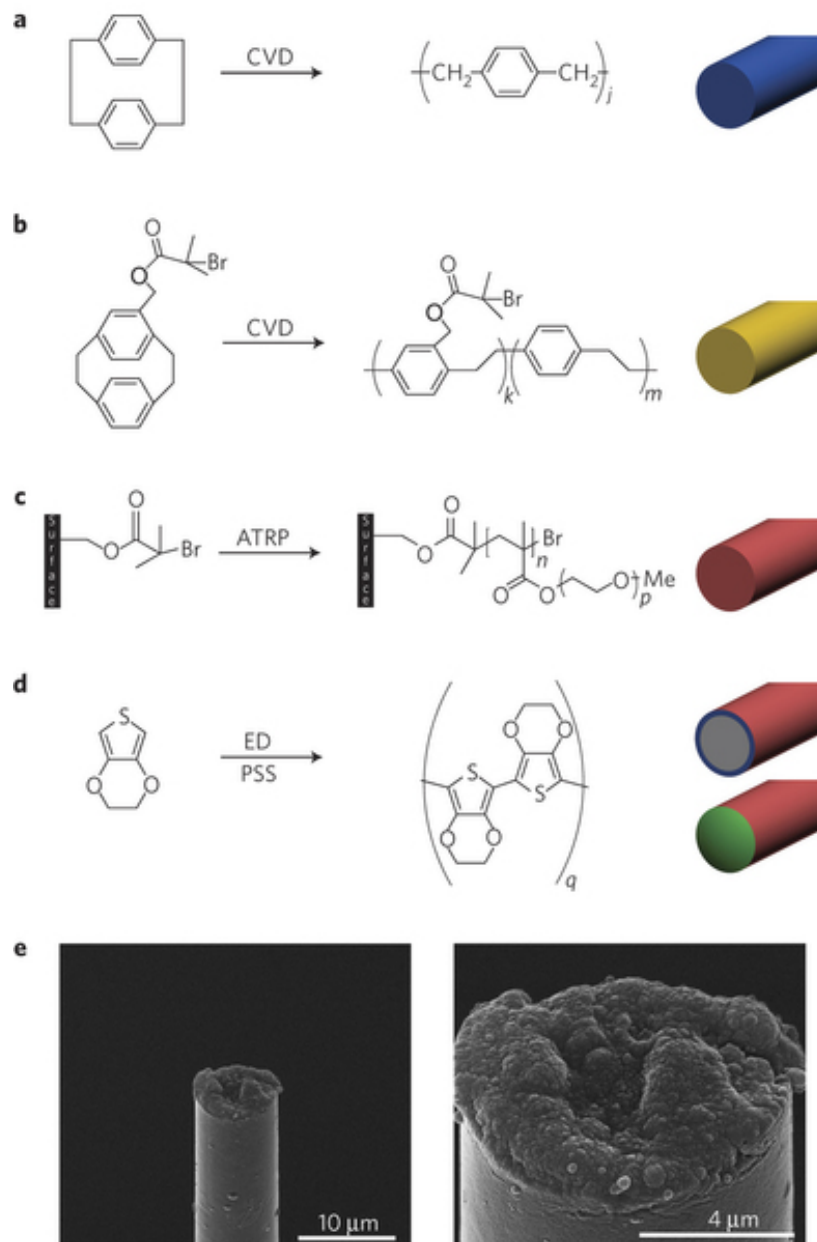


Figure 5.7 Microthread electrodes (MTE). a–d, Preparation of a MTE: carbon fibres are coated with 800nm poly(*p*-xylylene) (a); the fibre is further coated with a 50-nm-thick layer of poly(*p*-xylylene-4-methyl-2-bromoisobutyrate)-*co*-(*p*-xylylene) (b); poly(ethylene glycol) is covalently grafted onto the doubly coated fibre by ATRP (c); a carbon recording site is exposed at the tip by cutting away the insulation, and the recording site is coated with PEDOT by electrochemical deposition (d). SEM images of a fully assembled, functional MTE (e). The Confocal Raman Spectroscopy analysis of the MTE components is shown in Figure 5.8. EDX analysis is shown in Figure 5.9.

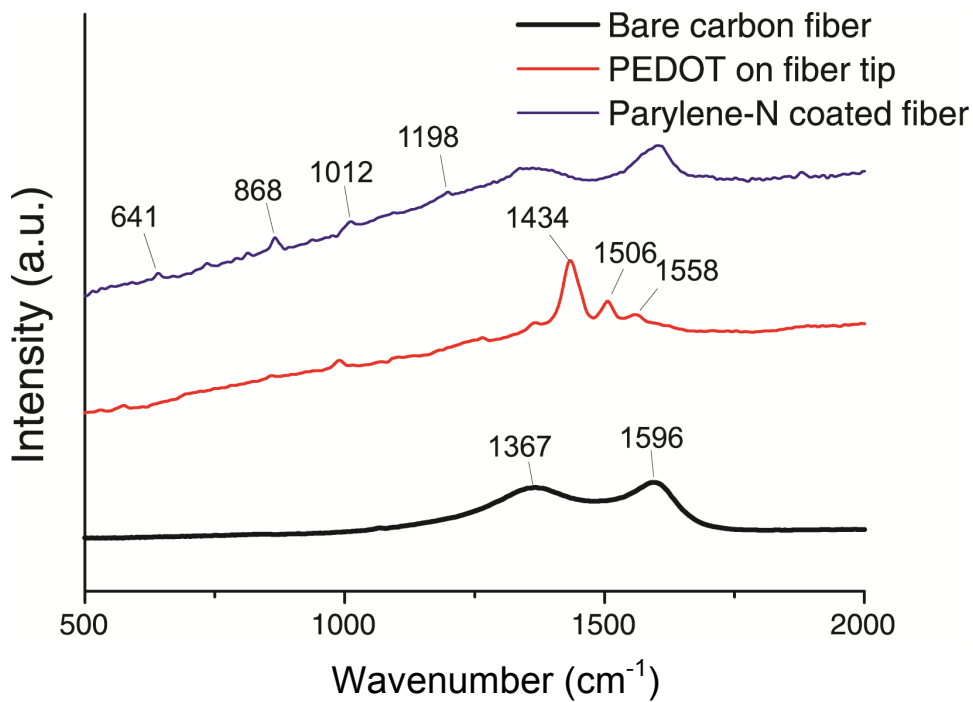


Figure 5.8 Raman Spectroscopy Analysis of MTE components. Raman Spectroscopy of bare carbon fibers (black), PEDOT recording tip (red), and poly(*p*-xylylene) coating (blue). Characteristic bands are labeled with their respective wavenumbers. This demonstrates that the parylene insulation was present along the sides of the carbon fiber surface. Also, PEDOT was detected at the tip of the device, but not along the insulated sides of the microthread electrode.

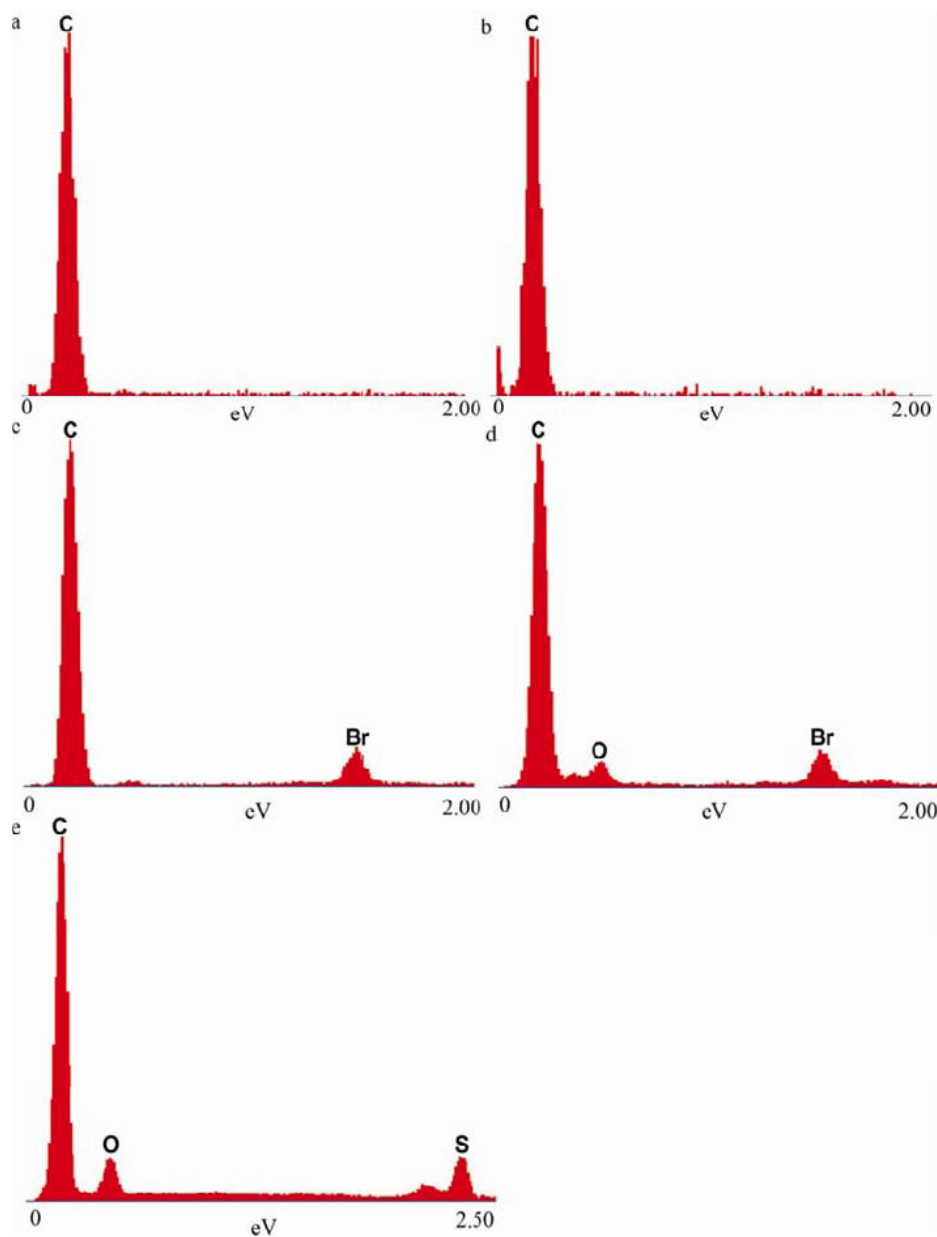


Figure 5.9 Stepwise EDX Analysis of Microthread Electrodes throughout fabrication. EDX data of MTE component. **a**, Carbon fiber, **b**, Poly(*p*-xylylene), **c**, Poly[*p*-xylylene-4-methyl-2-bromoisobutyrate]-*co*-(*p*-xylylene)]. **d**, PEGMA. **e**, PEDOT. The poly[*p*-xylylene-4-methyl-2-bromoisobutyrate]-*co*-(*p*-xylylene)] and PEGMA coatings were not detectable using Raman Spectroscopy, perhaps due to low activity of their Raman scattering frequencies. Therefore, EDX was also used to characterize the surface material after each fabrication step. Carbon fiber and parylene-N were not discernable using EDX. The bromine element could be detected after the 50 nm coating with poly[*p*-xylylene-4-methyl-2-bromoisobutyrate]-*co*-(*p*-xylylene)]. An increase in oxygen was detected as expected after the PEGMA coating. Sulfur was detected in PEDOT at the tip of the assembled Microthread Electrode. This suggests that each component of the fabrication is assembled into the MTE.

5.2.3 Results and Discussion

The resulting microthread electrodes (MTEs) were prepared by mounting 7 μm diameter carbon fibres onto a microelectrode printed circuit board. The carbon fibre was then coated with an 800nm poly(*p*-xylylene) coating using chemical vapor deposition (CVD) polymerization (Figure 5.7a). Poly(*p*-xylylene) (also known as parylene-N) was selected for its very low dissipation factor, high dielectric strength and low dielectric constant that is also invariant with frequency. A 50 nm thick layer of the functionalized polymer poly((*p*-xylylene-4-methyl-2-bromoisobutyrate)-*co*-(*p*-xylylene)) was deposited onto the poly(*p*-xylylene) coated fibre using CVD polymerization (Figure 5.7b). This polymer provides initiator groups for subsequent atom transfer radical polymerization (ATRP).⁵⁷ By ATRP, a ≈ 200 nm thick poly(ethylene glycol) methacrylate (PEGMA) top layer was deposited, which rendered the neuronal probe devices protein-resistant (Figure 5.7c).⁵⁷⁻⁵⁸ Finally, a recording site was created by electrochemical deposition of poly(3,4-ethylenedioxythiophene)/poly(styrenesulphonate) (PEDOT:PSS) onto the tip of the neuronal probe, from which the poly(*p*-xylylene) and PEGMA coatings had previously been removed (Figure 5.7d). The primary innovation of this technology is the combination of advanced materials to create an ultras-small organic interface that has the approximate size of a single trace on a conventional silicon neural probe, but sufficient strength and flexibility to act as a stand-alone electrode.

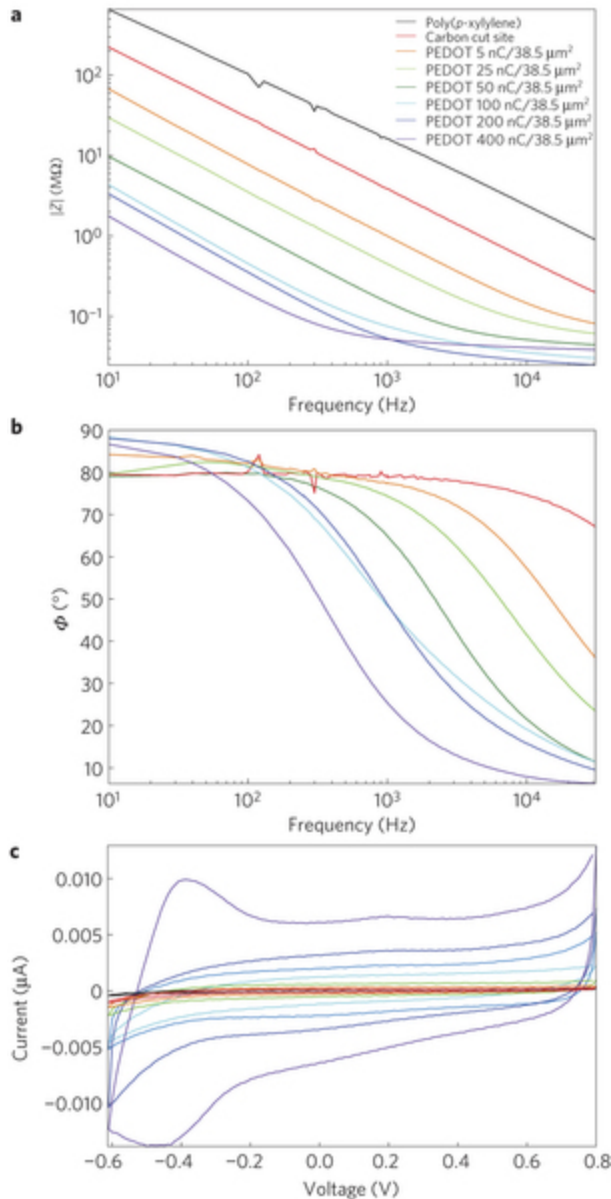


Figure 5.10 In vitro electrical characterization of MTEs. **a,b**, Electrical characterization of a poly(*p*-xylylene)-coated carbon fibre, a poly(*p*-xylylene)-coated fibre with an exposed carbon tip and a poly(*p*-xylylene)-coated fibre with a recording site of PEDOT:PSS electrodeposited with applied charges of 5, 25, 50, 100, 200 and 400 nC. **a**, Bode magnitude impedance plot showing decreasing impedance with increasing PEDOT deposition across all frequencies. **b**, Bode phase plot showing phase shift towards smaller phases indicative of a change from a capacitive carbon interface to a faradaic PEDOT interface with increasing deposition. The poly(*p*-xylylene)-insulated fibre without an exposed recording site was not plotted because a reliable signal could not be detected. **c**, Cyclic voltammogram showing increasing charge storage capacity with increasing PEDOT deposition in response to voltage cycling of the electrode site.

The MTE electrical properties were characterized by electrochemical impedance spectroscopy (EIS) and cyclic voltammetry. Measurements were taken for two controls: poly(*p*-xylylene) insulated carbon fibres, and poly(*p*-xylylene)-insulated fibres with a $\approx 38.5 \mu\text{m}^2$ exposed cut carbon tip. Last, poly(*p*-xylylene) insulated MTEs with recording sites and increasing degrees of PEDOT:PSS deposition were characterized. EIS measurements showed a progressive decrease in impedance as the insulation at the tip was removed, as well as with increasing PEDOT deposition (Figure 5.10a). The phase diagram also shows decreasing phase delay with increasing PEDOT deposition, which is a hallmark of PEDOT-coated electrical sites (Figure 5.10b).⁵⁹ Cyclic voltammetry measurements also showed increased charge storage capacity with increasing PEDOT deposition (Figure 5.10c), which could be relevant for brain stimulation devices. Cyclic voltammetry profiles indicate the presence of PEDOT on the recording site.

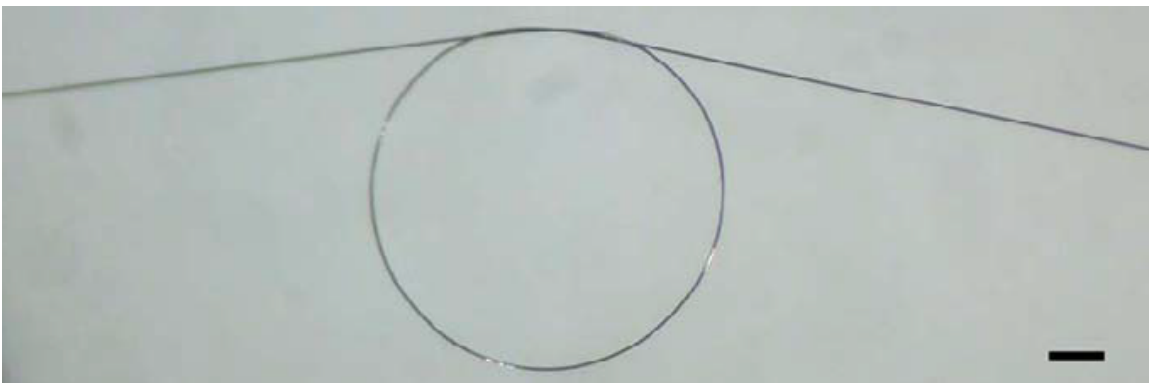


Figure 5.11 Demonstration of bending strength of Microthread Electrode. MTE can withstand substantial bending into, for instance, a loop-knot without any fracturing. Scale bare indicates 100 microns.

The MTEs also have an essential combination of mechanical properties for neural probes in terms of stiffness, strength and size (Figure 5.11). The stiffness (k) of a MTE calculated from the cross-sectional area (A), elastic modulus (E) and length implanted into the cortex (l) is $4,540 \text{ N m}^{-1}$, which is an order of magnitude smaller than for a conventional silicon microelectrode of the same length, $\approx 151,000 \text{ N m}^{-1}$ (ref.^{52c}). The cantilever beam spring constant (k_c) for a conventional silicon microelectrode is 2.13 N m^{-1} in the direction normal to the recording surface and 143 N m^{-1} in the lateral direction, whereas k_c for the MTE is 0.0106 N m^{-1} in all radial directions. This reduced stiffness or improved compliance ($1/k$) is primarily the result of the small-diameter carbon fibre, comparable to the size of cells, and the use of the thin parylene-N coating (Figure 5.12a). The k_c is superior over recently developed tunicate-derived nanocomposite probes.⁶⁰ Stiff implanted probes tethered to the skull may also cause rupture of the nearby blood brain barrier (BBB) during micromotion or physiological motion.^{48e, 52b, 61}

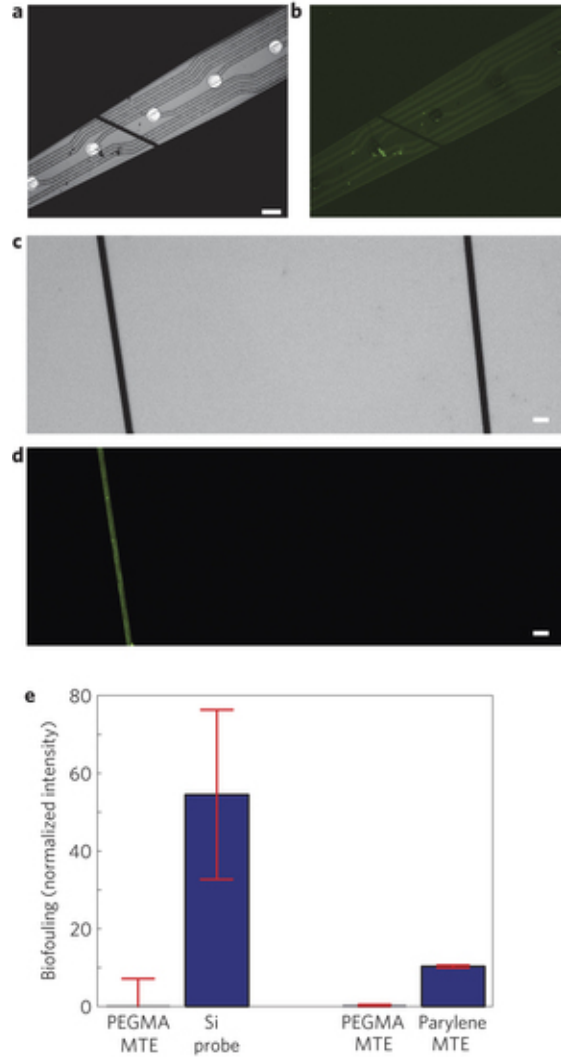


Figure 5.12 Physical characteristics of the MTEs. **a**, AMTE laid on top of a 10mm silicon electrode. Scale bar, 50 μm. **b**, FITC–albumin adsorbed onto a 10mm silicon electrode whereas an ATRP-PEGMA surface-coated MTE showed no adsorption. **c**, Bright-field images of FITC–albumin adsorbed onto a poly(*p*-xylylene)-coated device (left) and an ATRP-PEGMA coated device (right). Scale bar, 20 μm. **d**, The same image as in c under fluorescent microscopy showing less protein adsorption onto the PEGMA surface (right) compared with the poly(*p*-xylylene) surface (left). **e**, Comparison of the intensity of adsorbed FITC–albumin between PEGMA-coated MTEs and silicon probes (left), and PEGMA coated MTEs and poly(*p*-xylylene)-coated MTEs. Error bars show s.d.

To prevent biofouling from BBB disruption, the MTEs have a biofouling-resistant surface through functionalization of the outer poly(*p*-xylylene) insulation

with PEGMA, an anti-biofouling molecule. Although stab wound studies show limited chronic tissue damage,^{48a} plasma protein adsorption onto the electrode may perpetuate the tissue response in chronically implanted neural electrodes. For example, the plasma protein albumin is, in part, responsible for inducing glial cell activation and proliferation.⁶² Adsorption of plasma proteins to probe surfaces may perpetuate the release of pro-inflammatory cytokines and their continual adsorption onto the probe surface. Within the central nervous system, anti-biofouling coatings may have to be stable only long enough for cells to repair the BBB and clean up the plasma exudates, thereby allowing attenuation of pro-inflammatory cytokines in the probe's microenvironment.^{48e} As such, covalently grafted functional bioactive surface materials may be more effective for improving chronic neural interfaces than rapidly dissolving anti-biofouling hydrogels. Furthermore, although bioactive peptide coatings may denature, their effects have been shown to last for months.⁵⁶ The organic PEGMA surface material demonstrated improved antibiofouling properties from FITC-albumin adsorption compared with the native poly(*p*-xylylene) surface *in vitro* (Figure 5.12). The covalently grafted PEGMA layer has the added benefit of further minimizing the microelectrode footprint compared with traditional drug-eluting hydrogels that acutely push tissue away from the electrode surface. To the authors' knowledge, this is the first demonstration of a functionalized poly(*p*-xylylene) coating in a functional neural microelectrode. These properties are especially important when chronic use of the probes is intended.

5.2.4 Conclusion

This study brought together a new set of materials to make fundamental advances in microelectrode technology across the dimensions of size, strength, flexibility, surface biochemistry and electrical properties. The results demonstrated that this innovative composite microelectrode with a reduced footprint was able to chronically record single-unit spikes. To the best of the authors' knowledge this is: the smallest stand-alone implantable neuronal ultramicroelectrode; the first functionalized poly(*p*-xylylene) surface on a neural microelectrode; and the smallest recording electrode site to deposit PEDOT:PSS and successfully record chronic single-unit activity in the cortex. Furthermore, emerging PEDOT blends (PEDOT/carbon nanotubes) show promising results of being more stable than PEDOT:PSS (ref. ⁶³). Although these electrodes successfully recorded high-quality neural activity over several weeks, four of the seven implants had a headcap failure around the sixth week associated with poor printed circuit board design, compounded by the animal regularly bumping it into the cage. However, previous studies suggest that recordings become stable around 5-6 weeks.⁴⁹ Although the present data are extremely encouraging, especially for improving basic neuroscience research, it is difficult at this stage to predict outcomes of clinical relevance, typically demonstrated through long-term chronic testing in primates. Present efforts are focused on improving low-profile headcap connector designs and developing more mechanically stable mounting media to evaluate long-term viability. Another focus is to substitute the carbon-fibre core with carbon nanotube composite materials that are stronger and more flexible than platinum in addition to

being compatible with traditional microfabrication processes to enable manufacturing of high-density arrays.⁶⁴ These composite materials may negate the need for an organic recording site to detect biopotentials, and instead allow us to use these coatings for delivering bioactive molecules to the recording site.⁶⁵ These devices will be implanted into the brain by leveraging existing and emerging insertion techniques.⁶⁶ In the future, more advanced bio/nanomaterials could be used to further attenuate the tissue response and provide a more biomimetic, bio-integrating interface to further blur the line between organic and inorganic, perhaps with combinations of lipids, growth factors, cell adhesion molecules, drugs and/or enzymes.^{56, 67} The techniques and knowledge gained here will serve as a foundation for innovative long-term chronic implant designs that we anticipate will be transitioned to primate studies as the next step of this work.

The capability of monitoring specific neuronal ensembles for long periods of time with great precision would be a powerful tool in neuroscience research for linking low-level neuronal circuits to high-level brain function, such as learning, memory and perception. As a result of its small size, the MTE is also attractive for use with emerging optical technologies, such as *in vivo* multi-photon microscopy because it produces negligible optical shadows. These microelectrodes can also be grafted with fluorescent labels for *in vivo* multi-photon deep tissue microscopy neuroscience studies. The MTE's subcellular footprint also limits the impact of diffusion on biochemical and bioelectrical signaling around the device. Developing smaller and more flexible neural probes with advanced surface materials for long-term, high-quality and selective neural recording could potentially lead to paradigm

shifts in both neuroscience research and clinical neurotechnologies. The organic integrated (nano)composite microelectrode technology may be further tailored to other disciplines, such as cardiology, peripheral nerve injury or transdermal microelectrodes, to establish stealthy bio-interfaces for monitoring and controlling intrinsic biological pathways.

References

1. Alf, M. E.; Asatekin, A.; Barr, M. C.; Baxamusa, S. H.; Chelawat, H.; Ozaydin-Ince, G.; Petruczok, C. D.; Sreenivasan, R.; Tenhaeff, W. E.; Trujillo, N. J.; Vaddiraju, S.; Xu, J.; Gleason, K. K., Chemical Vapor Deposition of Conformal, Functional, and Responsive Polymer Films. *Adv Mater* **2010**, *22* (18), 1993-2027.
2. Deng, X. P.; Eyster, T. W.; Elkasabi, Y.; Lahann, J., Bio-Orthogonal Polymer Coatings for Co-Presentation of Biomolecules. *Macromol Rapid Comm* **2012**, *33* (8), 640-645.
3. Chen, H. Y.; Rouillard, J. M.; Gulari, E.; Lahann, J., Colloids with high-definition surface structures. *P Natl Acad Sci USA* **2007**, *104* (27), 11173-11178.
4. Chen, H. Y.; Hirtz, M.; Deng, X. P.; Laue, T.; Fuchs, H.; Lahann, J., Substrate-Independent Dip-Pen Nanolithography Based on Reactive Coatings. *J Am Chem Soc* **2010**, *132* (51), 18023-18025.
5. Zhang, Y.; Deng, X. P.; Scheller, E. L.; Kwon, T. G.; Lahann, J.; Franceschi, R. T.; Krebsbach, P. H., The effects of Runx2 immobilization on poly (epsilon-caprolactone) on osteoblast differentiation of bone marrow stromal cells in vitro. *Biomaterials* **2010**, *31* (12), 3231-3236.
6. Tawfick, S.; Deng, X. P.; Hart, A. J.; Lahann, J., Nanocomposite microstructures with tunable mechanical and chemical properties. *Phys Chem Chem Phys* **2010**, *12* (17), 4446-4451.
7. Kozai, T. D. Y.; Langhals, N. B.; Patel, P. R.; Deng, X. P.; Zhang, H. N.; Smith, K. L.; Lahann, J.; Kotov, N. A.; Kipke, D. R., Ultrasmall implantable composite microelectrodes with bioactive surfaces for chronic neural interfaces. *Nat Mater* **2012**, *11* (12), 1065-1073.
8. Chen, H. Y.; Lahann, J., Designable Biointerfaces Using Vapor-Based Reactive Polymers. *Langmuir* **2011**, *27* (1), 34-48.
9. (a) Holt, J. K.; Park, H. G.; Wang, Y. M.; Stadermann, M.; Artyukhin, A. B.; Grigoropoulos, C. P.; Noy, A.; Bakajin, O., Fast mass transport through sub-2-nanometer carbon nanotubes. *Science* **2006**, *312* (5776), 1034-1037; (b) Blair, P. J.; Jiang, J.; Schoeler, G. B.; Moron, C.; Anaya, E.; Cespedes, M.; Cruz, C.; Felices, V.; Guevara, C.; Mendoza, L.; Villaseca, P.; Sumner, J. W.; Richards, A. L.; Olson, J. G., Characterization of spotted fever group rickettsiae in flea and tick specimens from northern Peru. *J Clin Microbiol* **2004**, *42* (11), 4961-4967; (c) Katagiri, M.; Sakuma, N.; Suzuki, M.; Sakai, T.; Sato, S.; Hyakushima, T.; Nihei, M.; Awano, Y., Carbon nanotube vias fabricated by remote plasma-enhanced chemical vapor deposition. *Jpn J Appl Phys* **2008**, *47* (4), 2024-2027; (d) Baughman, R. H.; Zakhidov, A. A.; de Heer, W. A., Carbon nanotubes - the route toward applications. *Science* **2002**, *297* (5582), 787-792; (e) Coleman, J. N.; Khan, U.; Blau, W. J.; Gun'ko, Y. K., Small but strong: A review of the mechanical properties of carbon nanotube-polymer composites. *Carbon* **2006**, *44* (9), 1624-1652; (f) Eklund, P. C.; Ajayan, P. M.; Blackmon, R.; Hart, A. J.; Kong, J.; Pradhan, B.; Rao, A.; Rinzler, A. *International Assessment of Research and Development on Carbon Nanotubes: Manufacturing and Applications*; 2007.
10. Dresselhaus, M. S.; Dresselhaus, G.; Avouris, P., *Carbon Nanotubes: Synthesis, Structure, Properties and Applications* 1st ed.; Springer: 2001.

11. Salvetat, J. P.; Bonard, J. M.; Thomson, N. H.; Kulik, A. J.; Forro, L.; Benoit, W.; Zuppiroli, L., Mechanical properties of carbon nanotubes. *Appl Phys a-Mater* **1999**, *69* (3), 255-260.
12. (a) Strano, M. S.; Dyke, C. A.; Usrey, M. L.; Barone, P. W.; Allen, M. J.; Shan, H. W.; Kittrell, C.; Hauge, R. H.; Tour, J. M.; Smalley, R. E., Electronic structure control of single-walled carbon nanotube functionalization. *Science* **2003**, *301* (5639), 1519-1522; (b) Tasis, D.; Tagmatarchis, N.; Bianco, A.; Prato, M., Chemistry of carbon nanotubes. *Chem Rev* **2006**, *106* (3), 1105-1136.
13. Lin, C. M.; Lee, Y. T.; Yeh, S. R.; Fang, W. L., Flexible carbon nanotubes electrode for neural recording. *Biosens Bioelectron* **2009**, *24* (9), 2791-2797.
14. Kim, Y. A.; Hayashi, T.; Terrones, M.; Endo, M.; Dresselhaus, M. S., Selective Fabrication of Carbon Nanotube and Their Applications. *J Biomed Nanotechnol* **2006**, *2* (2), 106-108.
15. Barone, P. W.; Baik, S.; Heller, D. A.; Strano, M. S., Near-infrared optical sensors based on single-walled carbon nanotubes. *Nat Mater* **2005**, *4* (1), 86-U16.
16. Yurdumakan, B.; Raravikar, N. R.; Ajayan, P. M.; Dhinojwala, A., Synthetic gecko foot-hairs from multiwalled carbon nanotubes. *Chem Commun* **2005**, (30), 3799-3801.
17. Lau, K. K. S.; Bico, J.; Teo, K. B. K.; Chhowalla, M.; Amaratunga, G. A. J.; Milne, W. I.; McKinley, G. H.; Gleason, K. K., Superhydrophobic carbon nanotube forests. *Nano Lett* **2003**, *3* (12), 1701-1705.
18. Fan, S. S.; Chapline, M. G.; Franklin, N. R.; Tomblor, T. W.; Cassell, A. M.; Dai, H. J., Self-oriented regular arrays of carbon nanotubes and their field emission properties. *Science* **1999**, *283* (5401), 512-514.
19. Awano, Y.; Sato, S.; Kondo, D.; Ohfuti, M.; Kawabata, A.; Nihei, M.; Yokoyama, N., Carbon nanotube via interconnect technologies: size-classified catalyst nanoparticles and low-resistance ohmic contact formation. *Phys Status Solidi A* **2006**, *203* (14), 3611-3616.
20. (a) Talapatra, S.; Kar, S.; Pal, S. K.; Vajtai, R.; Ci, L.; Victor, P.; Shaijumon, M. M.; Kaur, S.; Nalamasu, O.; Ajayan, P. M., Direct growth of aligned carbon nanotubes on bulk metals. *Nat Nanotechnol* **2006**, *1* (2), 112-116; (b) Nessim, G. D.; Seita, M.; O'Brien, K. P.; Hart, A. J.; Bonaparte, R. K.; Mitchell, R. R.; Thompson, C. V., Low Temperature Synthesis of Vertically Aligned Carbon Nanotubes with Electrical Contact to Metallic Substrates Enabled by Thermal Decomposition of the Carbon Feedstock. *Nano Lett* **2009**, *9* (10), 3398-3405.
21. Yamamoto, N.; Hart, A. J.; Garcia, E. J.; Wicks, S. S.; Duong, H. M.; Slocum, A. H.; Wardle, B. L., High-yield growth and morphology control of aligned carbon nanotubes on ceramic fibers for multifunctional enhancement of structural composites. *Carbon* **2009**, *47* (3), 551-560.
22. (a) Nessim, G. D.; Hart, A. J.; Kim, J. S.; Acquaviva, D.; Oh, J. H.; Morgan, C. D.; Seita, M.; Leib, J. S.; Thompson, C. V., Tuning of Vertically-Aligned Carbon Nanotube Diameter and Areal Density through Catalyst Pre-Treatment. *Nano Lett* **2008**, *8* (11), 3587-3593; (b) Bennett, R. D.; Hart, A. J.; Cohen, R. E., Controlling the morphology of carbon nanotube films by varying the areal density of catalyst nanoclusters using block-copolymer micellar thin films. *Adv Mater* **2006**, *18* (17), 2274-+.

23. Garcia, E. J.; Wardle, B. L.; Hart, A. J., Joining prepreg composite interfaces with aligned carbon nanotubes. *Compos Part a-Appl S* **2008**, *39* (6), 1065-1070.
24. Tawfick, S.; O'Brien, K.; Hart, A. J., Flexible High-Conductivity Carbon-Nanotube Interconnects Made by Rolling and Printing. *Small* **2009**, *5* (21), 2467-2473.
25. Hayamizu, Y.; Yamada, T.; Mizuno, K.; Davis, R. C.; Futaba, D. N.; Yumura, M.; Hata, K., Integrated three-dimensional microelectromechanical devices from processable carbon nanotube wafers. *Nat Nanotechnol* **2008**, *3* (5), 289-294.
26. (a) Garcia, E. J.; Hart, A. J.; Wardle, B. L.; Slocum, A. H., Fabrication and nanocompression testing of aligned carbon-nanotube-polymer nanocomposites. *Adv Mater* **2007**, *19* (16), 2151-+; (b) Jung, Y. J.; Kar, S.; Talapatra, S.; Soldano, C.; Viswanathan, G.; Li, X. S.; Yao, Z. L.; Ou, F. S.; Avadhanula, A.; Vajtai, R.; Curran, S.; Nalamasu, O.; Ajayan, P. M., Aligned carbon nanotube-polymer hybrid architectures for diverse flexible electronic applications. *Nano Lett* **2006**, *6* (3), 413-418.
27. (a) Fang, W. L.; Chu, H. Y.; Hsu, W. K.; Cheng, T. W.; Tai, N. H., Polymer-reinforced, aligned multiwalled carbon nanotube composites for microelectromechanical systems applications. *Adv Mater* **2005**, *17* (24), 2987-+; (b) Miserendino, S.; Yoo, J.; Cassell, A.; Tai, Y. C., Electrochemical characterization of parylene-embedded carbon nanotube nanoelectrode arrays. *Nanotechnology* **2006**, *17* (4), S23-S28; (c) Vaddiraju, S.; Cebeci, H.; Gleason, K. K.; Wardle, B. L., Hierarchical Multifunctional Composites by Conformally Coating Aligned Carbon Nanotube Arrays with Conducting Polymer. *Acs Appl Mater Inter* **2009**, *1* (11), 2565-2572; (d) Li, J.; Stevens, R.; Delzeit, L.; Ng, H. T.; Cassell, A.; Han, J.; Meyyappan, M., Electronic properties of multiwalled carbon nanotubes in an embedded vertical array. *Appl Phys Lett* **2002**, *81* (5), 910-912.
28. Yoshida, M.; Langer, R.; Lendlein, A.; Lahann, J., From advanced biomedical coatings to multi-functionalized biomaterials. *Polym Rev* **2006**, *46* (4), 347-375.
29. Lahann, J., Vapor-based polymer coatings for potential biomedical applications. *Polym Int* **2006**, *55* (12), 1361-1370.
30. (a) Suh, K. Y.; Langer, R.; Lahann, J., Fabrication of elastomeric stamps with polymer-reinforced sidewalls via chemically selective vapor deposition polymerization of poly(p-xylylene). *Appl Phys Lett* **2003**, *83* (20), 4250-4252; (b) Hu, W. W.; Elkasabi, Y.; Chen, H. Y.; Zhang, Y.; Lahann, J.; Hollister, S. J.; Krebsbach, P. H., The use of reactive polymer coatings to facilitate gene delivery from poly (epsilon-caprolactone) scaffolds. *Biomaterials* **2009**, *30* (29), 5785-5792; (c) Chen, H. Y.; Elkasabi, Y.; Lahann, J., Surface modification of confined microgeometries via vapor-deposited polymer coatings. *J Am Chem Soc* **2006**, *128* (1), 374-380.
31. Plano, M. A.; Kumar, D.; Cleary, T. J., The effect of deposition conditions on the properties of vapor-deposited parylene AF-4 films. *Mater Res Soc Symp P* **1997**, *476*, 213-218.
32. Lahann, J.; Balcells, M.; Rodon, T.; Lee, J.; Choi, I. S.; Jensen, K. F.; Langer, R., Reactive polymer coatings: A platform for patterning proteins and mammalian cells onto a broad range of materials. *Langmuir* **2002**, *18* (9), 3632-3638.
33. Elkasabi, Y.; Yoshida, M.; Nandivada, H.; Chen, H. Y.; Lahann, J., Towards multipotent coatings: Chemical vapor deposition and biofunctionalization of carbonyl-substituted copolymers. *Macromol Rapid Comm* **2008**, *29* (11), 855-870.

34. Thevenet, S.; Chen, H. Y.; Lahann, J.; Stellacci, F., A generic approach towards nanostructured surfaces based on supramolecular nanostamping on reactive polymer coatings. *Adv Mater* **2007**, *19* (24), 4333-+.
35. Chen, H. Y.; Lahann, J., Vapor-assisted micropatterning in replica structures: A solventless approach towards topologically and chemically designable surfaces. *Adv Mater* **2007**, *19* (22), 3801-+.
36. Juneja, J. S.; Ten Eyck, G. A.; Bakhru, H.; Lu, T. M., Pressure dependent Parylene-N pore sealant penetration in porous low-kappa dielectrics. *J Vac Sci Technol B* **2005**, *23* (5), 2232-2235.
37. Wegenhart, B.; Tan, L.; Held, M.; Kieliszewski, M.; Chen, L., Aggregate structure of hydroxyproline-rich glycoprotein (HRGP) and HRGP assisted dispersion of carbon nanotubes. *Nanoscale Res Lett* **2006**, *1* (2), 154-159.
38. Lahann, J.; Klee, D.; Hocker, H., Chemical vapour deposition polymerization of substituted [2.2]paracyclophanes. *Macromol Rapid Comm* **1998**, *19* (9), 441-444.
39. Gorham, W. F., A New, General Synthetic Method for the Preparation of Linear Poly-p-xylylenes. *Journal of Polymer Science Part A-1: Polymer Chemistry* **1966**, *4* (12), 3027-3039.
40. Elkasabi, Y.; Chen, H. Y.; Lahann, J., Multipotent polymer coatings based on chemical vapor deposition copolymerization. *Adv Mater* **2006**, *18* (12), 1521-+.
41. Lin-Vien, D.; Colthup, N. B.; Fateley, W. G.; Grasselli, J. G., *The Handbook of Infrared and Raman Characteristic Frequencies of Organic Molecules*. 1st ed.; Academic Press: Boston, 1991.
42. Khang, D. Y.; Xiao, J. L.; Kocabas, C.; MacLaren, S.; Banks, T.; Jiang, H. Q.; Huang, Y. Y. G.; Rogers, J. A., Molecular scale buckling mechanics on individual aligned single-wall carbon nanotubes on elastomeric substrates. *Nano Lett* **2008**, *8* (1), 124-130.
43. (a) Tong, T.; Zhao, Y.; Delzeit, L.; Kashani, A.; Meyyappan, M.; Majumdar, A., Height independent compressive modulus of vertically aligned carbon nanotube arrays. *Nano Lett* **2008**, *8* (2), 511-515; (b) Cao, A. Y.; Dickrell, P. L.; Sawyer, W. G.; Ghasemi-Nejhad, M. N.; Ajayan, P. M., Super-compressible foamlike carbon nanotube films. *Science* **2005**, *310* (5752), 1307-1310.
44. (a) Kim, K. H.; Yoon, H. J.; Jeong, O. C.; Yang, S. S., Fabrication and test of a micro electromagnetic actuator. *Sensor Actuat a-Phys* **2005**, *117* (1), 8-16; (b) Katragadda, R.; Wang, Z.; Khalid, W.; Li, Y.; Xu, Y., Parylene cantilevers integrated with polycrystalline silicon piezoresistors for surface stress sensing. *Appl Phys Lett* **2007**, *91* (8).
45. Strumwasser, F., Long-Term Recording from Single Neurons in Brain of Unrestrained Mammals. *Science* **1958**, *127* (3296), 469-470.
46. (a) Kipke, D. R.; Shain, W.; Buzsaki, G.; Fetze, E.; Henderson, J. M.; Hetke, J. F.; Schalk, G., Advanced Neurotechnologies for Chronic Neural Interfaces: New Horizons and Clinical Opportunities. *J Neurosci* **2008**, *28* (46), 11830-11838; (b) Schmidt, E. M.; Bak, M. J.; McIntosh, J. S., Long-Term Chronic Recording from Cortical-Neurons. *Exp Neurol* **1976**, *52* (3), 496-506.
47. Grill, W. M.; Norman, S. E.; Bellamkonda, R. V., Implanted Neural Interfaces: Biochallenges and Engineered Solutions. *Annu Rev Biomed Eng* **2009**, *11*, 1-24.

48. (a) Biran, R.; Martin, D. C.; Tresco, P. A., Neuronal cell loss accompanies the brain tissue response to chronically implanted silicon microelectrode arrays. *Exp Neurol* **2005**, *195* (1), 115-126; (b) Rousche, P. J.; Normann, R. A., Chronic recording capability of the Utah Intracortical Electrode Array in cat sensory cortex. *J Neurosci Meth* **1998**, *82* (1), 1-15; (c) Ward, M. P.; Rajdev, P.; Ellison, C.; Irazoqui, P. P., Toward a comparison of microelectrodes for acute and chronic recordings. *Brain Res* **2009**, *1282*, 183-200; (d) Purcell, E. K.; Thompson, D. E.; Ludwig, K. A.; Kipke, D. R., Flavopiridol reduces the impedance of neural prostheses in vivo without affecting recording quality. *J Neurosci Meth* **2009**, *183* (2), 149-157; (e) Kozai, T. D. Y.; Vazquez, A. L.; LWeaver, C.; Kim, S. G.; Cui, X. T., In vivo two-photon microscopy reveals immediate microglial reaction to implantation of microelectrode through extension of processes. *J Neural Eng* **2012**, *9* (6).
49. Ludwig, K. A.; Uram, J. D.; Yang, J. Y.; Martin, D. C.; Kipke, D. R., Chronic neural recordings using silicon microelectrode arrays electrochemically deposited with a poly(3,4-ethylenedioxythiophene) (PEDOT) film. *J Neural Eng* **2006**, *3* (1), 59-70.
50. (a) Szarowski, D. H.; Andersen, M. D.; Retterer, S.; Spence, A. J.; Isaacson, M.; Craighead, H. G.; Turner, J. N.; Shain, W., Brain responses to micro-machined silicon devices. *Brain Res* **2003**, *983* (1-2), 23-35; (b) Polikov, V. S.; Tresco, P. A.; Reichert, W. M., Response of brain tissue to chronically implanted neural electrodes. *J Neurosci Meth* **2005**, *148* (1), 1-18.
51. (a) Clark, J. J.; Sandberg, S. G.; Wanat, M. J.; Gan, J. O.; Horne, E. A.; Hart, A. S.; Akers, C. A.; Parker, J. G.; Willuhn, I.; Martinez, V.; Evans, S. B.; Stella, N.; Phillips, P. E. M., Chronic microsensors for longitudinal, subsecond dopamine detection in behaving animals. *Nat Methods* **2010**, *7* (2), 126-U58; (b) Vanhorne, C. G.; Bement, S.; Hoffer, B. J.; Gerhardt, G. A., Multichannel Semiconductor-Based Electrodes for In vivo Electrochemical and Electrophysiological Studies in Rat Cns. *Neurosci Lett* **1990**, *120* (2), 249-252; (c) Matsumura, M.; Chen, D. F.; Sawaguchi, T.; Kubota, K.; Fetz, E. E., Synaptic interactions between primate precentral cortex neurons revealed by spike-triggered averaging of intracellular membrane potentials in vivo. *J Neurosci* **1996**, *16* (23), 7757-7767.
52. (a) Neary, J. T.; Kang, Y.; Willoughby, K. A.; Ellis, E. F., Activation of extracellular signal-regulated kinase by stretch-induced injury in astrocytes involves extracellular ATP and P2 purinergic receptors. *J Neurosci* **2003**, *23* (6), 2348-2356; (b) Subbaroyan, J.; Martin, D. C.; Kipke, D. R., A finite-element model of the mechanical effects of implantable microelectrodes in the cerebral cortex. *J Neural Eng* **2005**, *2* (4), 103; (c) Lee, H.; Bellamkonda, R. V.; Sun, W.; Levenston, M. E., Biomechanical analysis of silicon microelectrode-induced strain in the brain. *J Neural Eng* **2005**, *2* (4), 81-9; (d) LaPlaca, M. C.; Cullen, D. K.; McLoughlin, J. J.; Cargill, R. S., 2nd, High rate shear strain of three-dimensional neural cell cultures: a new in vitro traumatic brain injury model. *J Biomech* **2005**, *38* (5), 1093-105; (e) Gilletti, A.; Muthuswamy, J., Brain micromotion around implants in the rodent somatosensory cortex. *J Neural Eng* **2006**, *3* (3), 189-95.
53. (a) Kim, D. H.; Viveni, J.; Amsden, J. J.; Xiao, J.; Vigeland, L.; Kim, Y. S.; Blanco, J. A.; Panilaitis, B.; Frechette, E. S.; Contreras, D.; Kaplan, D. L.; Omenetto, F. G.; Huang, Y.; Hwang, K. C.; Zakin, M. R.; Litt, B.; Rogers, J. A., Dissolvable films of silk fibroin for ultrathin conformal bio-integrated electronics. *Nat Mater* **2010**, *9* (6),

- 511-7; (b) Takeuchi, S.; Ziegler, D.; Yoshida, Y.; Mabuchi, K.; Suzuki, T., Parylene flexible neural probes integrated with microfluidic channels. *Lab Chip* **2005**, *5* (5), 519-23; (c) Rousche, P. J.; Pellinen, D. S.; Pivin, D. P., Jr.; Williams, J. C.; Vetter, R. J.; Kipke, D. R., Flexible polyimide-based intracortical electrode arrays with bioactive capability. *IEEE Trans Biomed Eng* **2001**, *48* (3), 361-71.
54. Seymour, J. P.; Kipke, D. R., Neural probe design for reduced tissue encapsulation in CNS. *Biomaterials* **2007**, *28* (25), 3594-607.
55. Cui, X. T.; Zhou, D. D., Poly (3,4-ethylenedioxythiophene) for chronic neural stimulation. *IEEE Trans Neural Syst Rehabil Eng* **2007**, *15* (4), 502-8.
56. Azemi, E.; Lagenaur, C. F.; Cui, X. T., The surface immobilization of the neural adhesion molecule L1 on neural probes and its effect on neuronal density and gliosis at the probe/tissue interface. *Biomaterials* **2011**, *32* (3), 681-692.
57. Jiang, X. W.; Chen, H. Y.; Galvan, G.; Yoshida, M.; Lahann, J., Vapor-based initiator coatings for atom transfer radical polymerization. *Adv Funct Mater* **2008**, *18* (1), 27-35.
58. Katira, P.; Agarwal, A.; Fischer, T.; Chen, H. Y.; Jiang, X.; Lahann, J.; Hess, H., Quantifying the performance of protein-resisting surfaces at ultra-low protein coverages using kinesin motor proteins as probes. *Adv Mater* **2007**, *19* (20), 3171-+.
59. Jan, E.; Hendricks, J. L.; Husaini, V.; Richardson-Burns, S. M.; Sereno, A.; Martin, D. C.; Kotov, N. A., Layered Carbon Nanotube-Polyelectrolyte Electrodes Outperform Traditional Neural Interface Materials. *Nano Lett* **2009**, *9* (12), 4012-4018.
60. Harris, J. P.; Capadona, J. R.; Miller, R. H.; Healy, B. C.; Shanmuganathan, K.; Rowan, S. J.; Weder, C.; Tyler, D. J., Mechanically adaptive intracortical implants improve the proximity of neuronal cell bodies. *J Neural Eng* **2011**, *8* (6), 066011.
61. Bjornsson, C. S.; Oh, S. J.; Al-Kofahi, Y. A.; Lim, Y. J.; Smith, K. L.; Turner, J. N.; De, S.; Roysam, B.; Shain, W.; Kim, S. J., Effects of insertion conditions on tissue strain and vascular damage during neuroprosthetic device insertion. *J Neural Eng* **2006**, *3* (3), 196-207.
62. (a) Ivens, S.; Kaufer, D.; Flores, L. P.; Bechmann, I.; Zumsteg, D.; Tomkins, O.; Seiffert, E.; Heinemann, U.; Friedman, A., TGF-beta receptor-mediated albumin uptake into astrocytes is involved in neocortical epileptogenesis. *Brain* **2007**, *130* (Pt 2), 535-47; (b) Nadal, A.; Fuentes, E.; Pastor, J.; McNaughton, P. A., Plasma-Albumin Is a Potent Trigger of Calcium Signals and DNA-Synthesis in Astrocytes. *P Natl Acad Sci USA* **1995**, *92* (5), 1426-1430.
63. Luo, X. L.; Weaver, C. L.; Zhou, D. D.; Greenberg, R.; Cui, X. Y. T., Highly stable carbon nanotube doped poly(3,4-ethylenedioxythiophene) for chronic neural stimulation. *Biomaterials* **2011**, *32* (24), 5551-5557.
64. Shim, B. S.; Tang, Z. Y.; Morabito, M. P.; Agarwal, A.; Hong, H. P.; Kotov, N. A., Integration of conductivity transparency, and mechanical strength into highly homogeneous layer-by-layer composites of single-walled carbon nanotubes for optoelectronics. *Chem Mater* **2007**, *19* (23), 5467-5474.
65. (a) Keefer, E. W.; Botterman, B. R.; Romero, M. I.; Rossi, A. F.; Gross, G. W., Carbon nanotube coating improves neuronal recordings. *Nat Nanotechnol* **2008**, *3* (7), 434-439; (b) Luo, X. L.; Matranga, C.; Tan, S. S.; Alba, N.; Cui, X. Y. T., Carbon nanotube nanoreservoir for controlled release of anti-inflammatory dexamethasone.

Biomaterials **2011**, *32* (26), 6316-6323; (c) Cui, X. Y.; Lee, V. A.; Raphael, Y.; Wiler, J. A.; Hetke, J. F.; Anderson, D. J.; Martin, D. C., Surface modification of neural recording electrodes with conducting polymer/biomolecule blends. *J Biomed Mater Res* **2001**, *56* (2), 261-272.

66. (a) Kozai, T. D. Y.; Kipke, D. R., Insertion shuttle with carboxyl terminated self-assembled monolayer coatings for implanting flexible polymer neural probes in the brain. *J Neurosci Meth* **2009**, *184* (2), 199-205; (b) Gilgunn, P. J.; Khilwani, R.; Kozai, T. D. Y.; Weber, D. J.; Cui, X. T.; Erdos, G.; Ozdoganlar, O. B.; Fedder, G. K. In *An ultra-compliant, scalable neural probe with molded biodissolvable delivery vehicle*, Micro Electro Mechanical Systems (MEMS), 2012 IEEE 25th International Conference on, Jan. 29 2012-Feb. 2 2012; 2012; pp 56-59.

67. Kotov, N. A.; Winter, J. O.; Clements, I. P.; Jan, E.; Timko, B. P.; Campidelli, S.; Pathak, S.; Mazzatenta, A.; Lieber, C. M.; Prato, M.; Bellamkonda, R. V.; Silva, G. A.; Kam, N. W. S.; Patolsky, F.; Ballerini, L., Nanomaterials for Neural Interfaces. *Adv Mater* **2009**, *21* (40), 3970-4004.

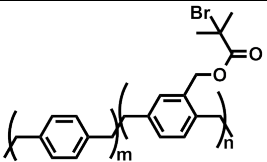
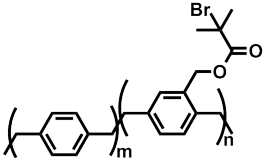
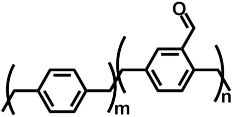
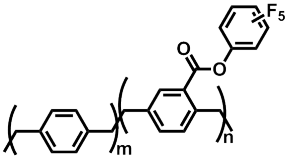
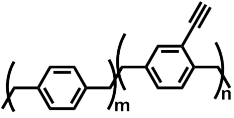
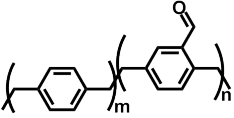
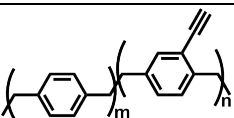
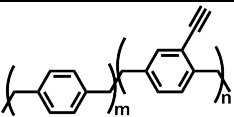
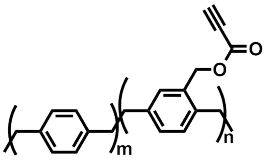
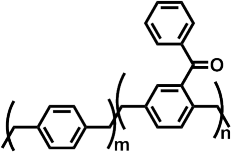
CHAPTER 6

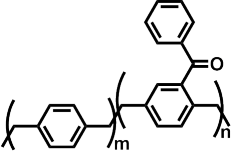
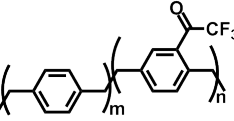
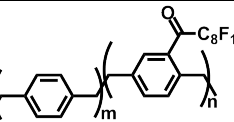
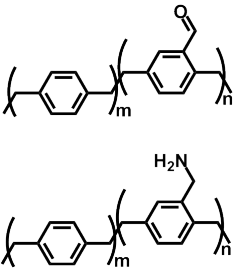
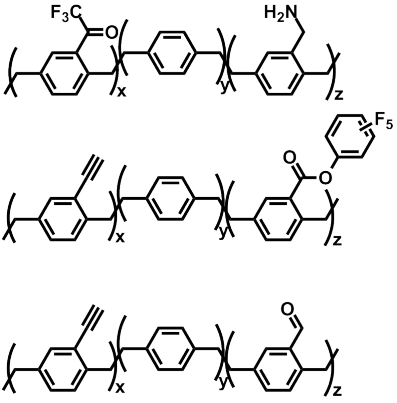
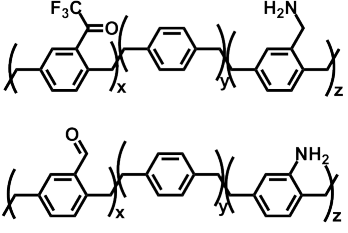
Conclusion and Future Directions

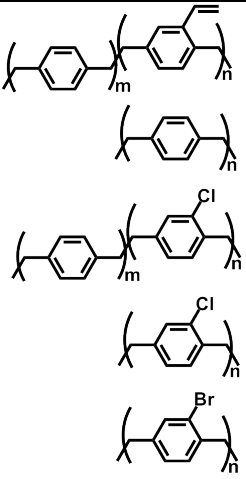
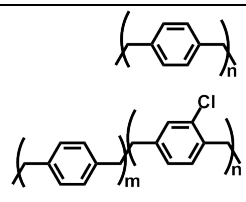
6.1 Conclusion

In this dissertation, four different application areas of functionalized CVD polymers have been presented: orthogonal immobilization strategies for multiple biomolecules (Chapter 2), metal enhanced fluorescence for biosensor development (Chapter 3), biodegradable CVD polymer coatings (Chapter 4) and CVD polymer applications in complex structures and integrated devices (Chapter 5). This dissertation mainly focuses on surface design for biomedical applications. Together with previous studies based on the functionalized [2.2]paracyclophane CVD polymerization, we have shown that the surface functionalization and coating platform is useful in many applications. (Listed in Table 6.1). A wide variety of surface reactions were used in these studies, which are also summarized in Table 6.1.

Table 6.1 Applications summary of the functionalized [2.2]paracyclophane CVD polymerization.

Application	CVD polymer	Surface reaction	Reference
Protein resistant surface		Atom transfer radical polymerization (ATRP) of Poly(ethylene glycol) monomethyl ether methacrylate (PEGMA)	¹
Cell adhesion resistant surface		ATRP of PEGMA	^{1c}
Sugar immobilization		Aldehyde-hydrazide reaction	²
Protein and cell immobilization		Active ester-amine chemistry	³
Peptide immobilization		Copper catalyzed alkyne-azide cycloaddition (CuAAC)	^{2b, 3a}
DNA supramolecular nanostamping		Aldehyde-amine reaction	⁴
Dip-pen nano-patterning		CuAAC	⁵
Copper catalyzed “click” chemistry		CuAAC	⁶
Copper-free “click” chemistry		Copper-free activated alkyne-azide cycloaddition	⁷
2D and 3D surface Photo-patterning		UV crosslinking	⁸

Photoresist		UV crosslinking	9
Surface modifications of micro- and nano-structures		Hydrazide-ketone reaction	10
Superhydrophobic surface		Hydrazide-ketone reaction	11
Thermal bonding		Aldehyde-amine reaction	12
Copolymers with defined functional group ratios		Hydrazide-ketone reaction NHS ester-amine reaction CuAAC Active ester-amine chemistry CuAAC Hydrazide-aldehyde reaction	2b, 3a, 13
Functional groups and immobilized molecules gradient		Hydrazide-ketone reaction NHS ester-amine reaction Hydrazide-aldehyde reaction Sulfo NHS ester-amine reaction	14

Substrate-selective CVD coating on certain metals		For the vinyl functionalized polymer: Cross metathesis reaction with Grubbs catalyst	15
Electrode insulation layer		No reactive group on the insulation layer, but another functionalized layer is usually coated on top of the insulation layer	1d, 12b

6.2 Future Directions

6.2.1 Combining the Functional Coating Platform with Multifunctional Linkers

Chemical vapor deposition polymerization of [2.2]paracyclophane is a powerful surface functionalization platform, but like any other techniques, it still has limitations. Not every type of functional group attached to the [2.2]paracyclophane molecule can survive the thermal pyrolysis condition ($>500\text{ }^{\circ}\text{C}$) under vacuum, which is essential for the paracyclophane ring-opening and the diradicals generation. Some functionalized paracyclophane could not form a high molecular weight polymer. Some others can successfully polymerize but functional group loss due to partial degradation and side reactions could occur. Thus it is not always easy to synthesize paracyclophanes with new functional groups useful for

the CVD process. Fortunately, developments in organic synthesis have made a lot of multifunctional linkers easily accessible or even commercially available. For example, a wide selection of multifunctional polyethylene glycol (PEG) linkers is now commercially available. These PEG linkers have different chain lengths (molecular weight), choices of linear or star shapes and commonly used functional groups for bioconjugation chemistries.¹⁶ The PEG molecules not only can serve as linkers to introduce functional groups not available for the CVD process, but also an essential layer to prevent protein non-specific binding. Linkers not commercially available can usually be synthesized to meet specific requirements.

6.2.2 Understanding the Biomolecule-Surface Interactions

To date, we have mostly focused on the biomolecule immobilizations and their biological activities were tested in some studies.^{3a, b} Most of the traditional thin film characterization methods such as FTIR, XPS and ellipsometry are carried out at the air-solid interface. The changes of the biomolecules structure, conformation and orientation at the liquid-air interface remain extremely challenging and need to be studied in the future with appropriate instruments (for instance, IR, AFM at the liquid-solid interface, sum frequency generation (SFG) vibrational spectroscopy etc.). Molecular dynamics based simulation methods can also provide some insight into this issue. We are currently conducting collaborative researches to study the peptide and protein conformation change at the biointerface. Reactive CVD polymers, together with a wide selection of multifunctional linkers provide a versatile surface design platform. With better understanding of the biomolecule-

surface interactions, we may be able to introduce necessary molecules on the surface to protect and stabilize target biomolecules even under water-free conditions.

6.2.3 Improving the CVD Polymerization System Design

The CVD polymerization system we currently use works well in most ultrathin film coating applications (thickness $<1 \mu\text{m}$) and the thickness can be well controlled by changing the monomer-feeding amount. For thicker film deposition, an adapted system design is necessary. The system also needs to be modified for new monomer types which are not the [2.2]paracyclopane derivatives such as the cyclic ketene acetals used for the degradable CVD polymer synthesis. It is much more convenient to do traditional polymer analyses (molecular weight, thermal analysis etc.) on thicker films since most of the measurements require milligram amount of the molecules to be analyzed. Existing CVD polymerization system design such as iCVD can be used as a reference for the changes.¹⁷

6.2.4 Developing More Integrated and Sophisticated Devices

An integrated biomedical device design needs multidisciplinary collaborative efforts. (Figure 6.1) These collaborative efforts open exciting new avenues for research and commercialization. Applying CVD polymer coatings to more integrated and sophisticated devices is an important future direction.

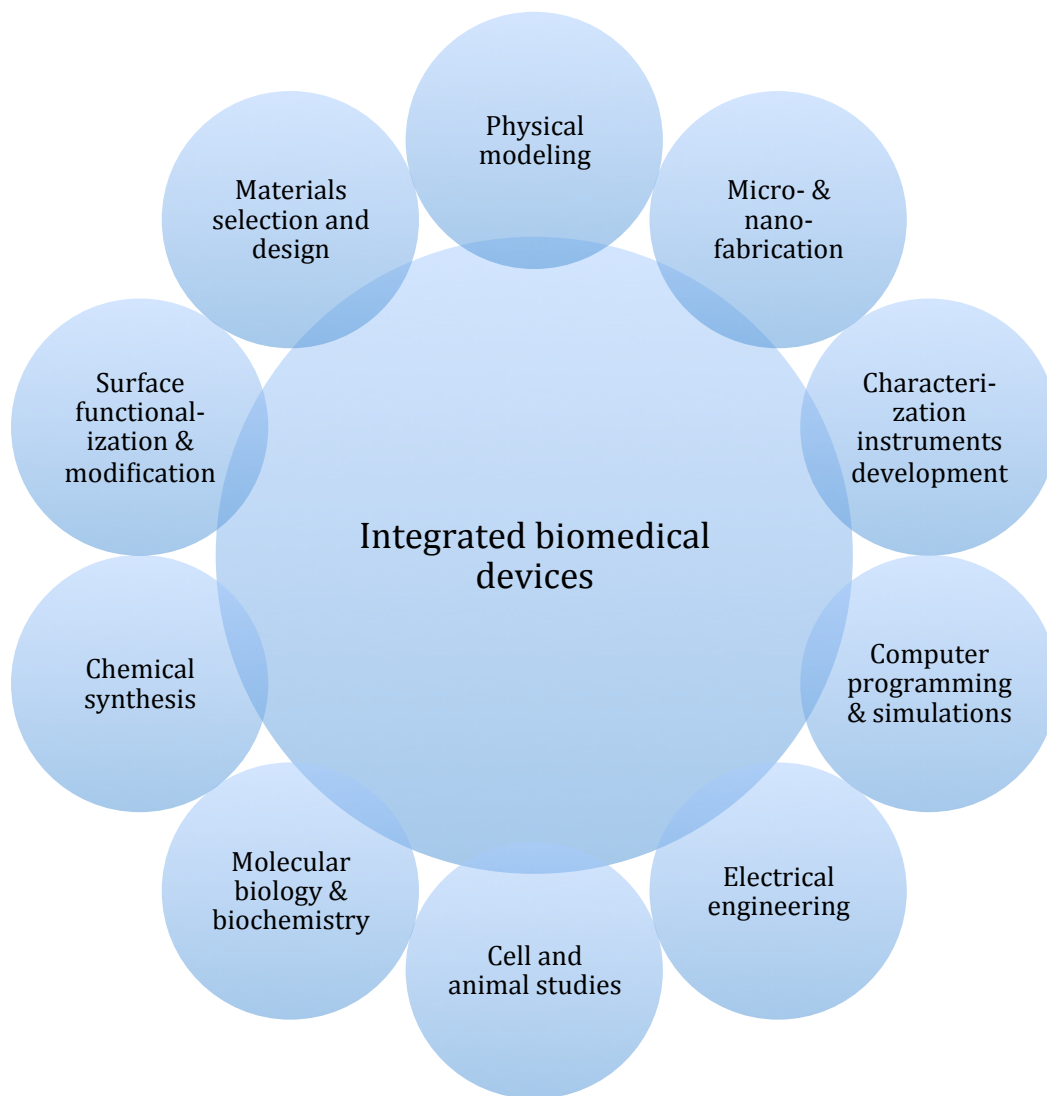


Figure 6.1 Multidisciplinary collaborative efforts for designing and producing integrated biomedical devices.

References

1. (a) Agarwal, A.; Luria, E.; Deng, X. P.; Lahann, J.; Hess, H., Landing Rate Measurements to Detect Fibrinogen Adsorption to Non-fouling Surfaces. *Cell Mol Bioeng* **2012**, *5* (3), 320-326; (b) Katira, P.; Agarwal, A.; Fischer, T.; Chen, H. Y.; Jiang, X.; Lahann, J.; Hess, H., Quantifying the performance of protein-resisting surfaces at ultra-low protein coverages using kinesin motor proteins as probes. *Adv Mater* **2007**, *19* (20), 3171-+; (c) Jiang, X. W.; Chen, H. Y.; Galvan, G.; Yoshida, M.; Lahann, J., Vapor-based initiator coatings for atom transfer radical polymerization. *Adv Funct Mater* **2008**, *18* (1), 27-35; (d) Kozai, T. D. Y.; Langhals, N. B.; Patel, P. R.; Deng, X. P.; Zhang, H. N.; Smith, K. L.; Lahann, J.; Kotov, N. A.; Kipke, D. R., Ultrasmall implantable composite microelectrodes with bioactive surfaces for chronic neural interfaces. *Nat Mater* **2012**, *11* (12), 1065-1073.
2. (a) Nandivada, H.; Chen, H. Y.; Lahann, J., Vapor-based synthesis of poly [(4-formyl-p-xylylene)-co-(p-xylylene)] and its use for biomimetic surface modifications. *Macromol Rapid Comm* **2005**, *26* (22), 1794-1799; (b) Deng, X. P.; Lahann, J., A Generic Strategy for Co-Presentation of Heparin-Binding Growth Factors Based on CVD Polymerization. *Macromol Rapid Comm* **2012**, *33* (17), 1459-1465.
3. (a) Deng, X. P.; Eyster, T. W.; Elkasabi, Y.; Lahann, J., Bio-Orthogonal Polymer Coatings for Co-Presentation of Biomolecules. *Macromol Rapid Comm* **2012**, *33* (8), 640-645; (b) Zhang, Y.; Deng, X. P.; Scheller, E. L.; Kwon, T. G.; Lahann, J.; Franceschi, R. T.; Krebsbach, P. H., The effects of Runx2 immobilization on poly (epsilon-caprolactone) on osteoblast differentiation of bone marrow stromal cells in vitro. *Biomaterials* **2010**, *31* (12), 3231-3236; (c) Lahann, J.; Balcells, M.; Rodon, T.; Lee, J.; Choi, I. S.; Jensen, K. F.; Langer, R., Reactive polymer coatings: A platform for patterning proteins and mammalian cells onto a broad range of materials. *Langmuir* **2002**, *18* (9), 3632-3638.
4. Thevenet, S.; Chen, H. Y.; Lahann, J.; Stellacci, F., A generic approach towards nanostructured surfaces based on supramolecular nanostamping on reactive polymer coatings. *Adv Mater* **2007**, *19* (24), 4333-+.
5. Chen, H. Y.; Hirtz, M.; Deng, X. P.; Laue, T.; Fuchs, H.; Lahann, J., Substrate-Independent Dip-Pen Nanolithography Based on Reactive Coatings. *J Am Chem Soc* **2010**, *132* (51), 18023-18025.
6. Nandivada, H.; Chen, H. Y.; Bondarenko, L.; Lahann, J., Reactive polymer coatings that "click". *Angew Chem Int Edit* **2006**, *45* (20), 3360-3363.
7. Deng, X. P.; Friedmann, C.; Lahann, J., Bio-orthogonal "Double-Click" Chemistry Based on Multifunctional Coatings. *Angew Chem Int Edit* **2011**, *50* (29), 6522-6526.
8. (a) Chen, H. Y.; Lahann, J., Fabrication of discontinuous surface patterns within microfluidic channels using photodefinable vapor-based polymer coatings. *Anal Chem* **2005**, *77* (21), 6909-6914; (b) Chen, H. Y.; Rouillard, J. M.; Gulari, E.; Lahann, J., Colloids with high-definition surface structures. *P Natl Acad Sci USA* **2007**, *104* (27), 11173-11178.

9. Wu, M. G.; Hsu, H. L.; Hsiao, K. W.; Hsieh, C. C.; Chen, H. Y., Vapor-Deposited Parylene Photoresist: A Multipotent Approach toward Chemically and Topographically Defined Biointerfaces. *Langmuir* **2012**, *28* (40), 14313-14322.
10. (a) Chen, H. Y.; Elkasabi, Y.; Lahann, J., Surface modification of confined microgeometries via vapor-deposited polymer coatings. *J Am Chem Soc* **2006**, *128* (1), 374-380; (b) Tawfick, S.; Deng, X. P.; Hart, A. J.; Lahann, J., Nanocomposite microstructures with tunable mechanical and chemical properties. *Phys Chem Chem Phys* **2010**, *12* (17), 4446-4451.
11. Elkasabi, Y.; Nandivada, H.; Chen, H. Y.; Bhaskar, S.; D'Arcy, J.; Bondarenko, L.; Lahann, J., Partially Fluorinated Poly-p-xylylenes Synthesized by CVD Polymerization. *Chem Vapor Depos* **2009**, *15* (4-6), 142-149.
12. (a) Chen, H. Y.; McClelland, A. A.; Chen, Z.; Lahann, J., Solventless adhesive bonding using reactive polymer coatings. *Anal Chem* **2008**, *80* (11), 4119-4124; (b) Seymour, J. P.; Elkasabi, Y. M.; Chen, H. Y.; Lahann, J.; Kipke, D. R., The insulation performance of reactive parylene films in implantable electronic devices. *Biomaterials* **2009**, *30* (31), 6158-6167.
13. Elkasabi, Y.; Chen, H. Y.; Lahann, J., Multipotent polymer coatings based on chemical vapor deposition copolymerization. *Adv Mater* **2006**, *18* (12), 1521-+.
14. (a) Elkasabi, Y. M.; Lahann, J.; Krebsbach, P. H., Cellular transduction gradients via vapor-deposited polymer coatings. *Biomaterials* **2011**, *32* (7), 1809-1815; (b) Elkasabi, Y.; Lahann, J., Vapor-Based Polymer Gradients. *Macromol Rapid Comm* **2009**, *30* (1), 57-63.
15. Chen, H. Y.; Lai, J. H.; Jiang, X. W.; Lahann, J., Substrate-selective chemical vapor deposition of reactive polymer coatings. *Adv Mater* **2008**, *20* (18), 3474-+.
16. Hermanson, G. T., *Bioconjugate Techniques*. 2nd ed.; Academic Press: 2008.
17. (a) Sreenivasan, R.; Gleason, K. K., Overview of Strategies for the CVD of Organic Films and Functional Polymer Layers. *Chem Vapor Depos* **2009**, *15* (4-6), 77-90; (b) Tenhaeff, W. E.; Gleason, K. K., Initiated and oxidative chemical vapor deposition of polymeric thin films: iCVD and oCVD. *Adv Funct Mater* **2008**, *18* (7), 979-992.